AUTOMATED HYDRODYNAMIC TRAP FOR SINGLE CELL ANALYSIS IN FREE SOLUTION

BY

ERIC MICHAEL JOHNSON CHAVARRIA

DISSERTATION

Submitted in partial fulfillment of the requirements
for the degree of Doctor of Philosophy in Biophysics and Computational Biology
in the Graduate College of the
University of Illinois at Urbana-Champaign, 2014

Urbana, Illinois

Doctoral Committee:

Assistant Professor Charles Schroeder, Chair
Assistant Professor Su-A Myong
Assistant Professor Tom Kuhlman
Professor Emad Tajkhorshid
Professor Paul Selvin

Abstract

Over the last several years, microfluidic-based techniques have been developed to study inducible gene expression at the single cell level, albeit without the ability to control external stimuli with precise methods. Most are limited by long diffusive timescales to alternate environmental concentrations. In this work, we report a microfluidic-based platform for single cell analysis that provides dynamic control over periodic, time-dependent culture media. Single cells are confined in free solution by the sole action of gentle fluid flow, thereby enabling non-perturbative trapping of cells for long time scales.

Recent studies have reported the ability of biological systems to implement low-pass filters to distinguish high frequency noise in environmental stimuli from lower frequency input signals. This cellular adaptation is critical for survival in fluctuating environmental conditions, yet we still lack a complete understanding of this phenomenon. The hydrodynamic trap was developed as a step forward in elucidate single cells in changing environmental conditions. To become the single cell microbioreactor (SCM), our trapping technique went through four generations.

Our first generation was directed at sequencing organisms that were uncultivated. Rumen fauna from cattle, sheep, and reindeer consist of a

heterogeneous cell mixture including *Oscillospira spp.* These bacterium have distinct septation patterns and form spores. In particular, *O. guilliermondii* has been observed in these rumen sample for almost a century yet we are still unable to cultivate them within the lab. Our hydrodynamic trapping technique was able to isolate and sort up to 50 *O. guilliermondii* cells from a heterogeneous environmental rumen sample. Our proof-of-principle demonstration produced $\succ$80 % sample purity.

Our second generation was aimed at live cell growth for defining our trapping technique as a non perturbative method. Many other methods of confinement produce perturbations through optical, magnetic, acoustic, or electrokinetic fields. Our technique utilizes the sole action of fluid flow for confining target cells. We observed *Escherichia coli* cells run and tumble within our trap. In addition, we observed increasing growth rates over 5 generations. Our results demonstrate that cells beneficially adapt to the trap environment. This non-perturbative nature of our trap is useful for observing cells over extended periods of time.

Finally, our third and final generation was aimed at elucidating gene expression under oscillating nutrient conditions. We observed gene expression under periodic concentrations of a lactose mimic. We also, performed diffusion experiments of TetR:EYFP on a chromosomal binding array by rapidly switching to concentrations of aTc. Using the SCM, we are able to observe the rapid release and subsequent intracellular diffusion of the Tet repressor within the nucleoid region of Gram-negative bacteria. Overall, this microfluidic bioreactor provides a direct method for sustaining periodic environmental conditions, measuring growth rates, detecting gene expression, and observing intracellular diffusion within single cells suspended at a stagnation point.

To my parents for the life I have.

To my spouse for the life we have yet to live.

Acknowledgments

My time at the University of Illinois Urbana-Champaign has been overall rewarding and I have met many interesting people who share a passion for research, outreach, and teaching. My apologies in advance if I fail to mention someone, however your influence and interactions have not been forgotten.

I thank my parents for instilling a passion for success and discovery in me every day. For always being there with encouragement, love, and support. For all the sacrifices you have made so that I can have the opportunities I've dreamed of.

I have much appreciation and love for my spouse, Veronica. For her patience, understanding and solidarity during the hard times of my doctorate. This process would not have been endurable without her presence and support. For encouraging us to adopt Jake, Byron, and Robbie. Without them graduate life would not have been as memorable.

With the upmost respect and gratitude I acknowledge my advisor, Charles Schroeder for his patience, support, and mentorship. Without his unfaltering encouragement and support, I would not have become the scientific researcher I am today.

To the late Professor and Director of Biophysics, Bob Clegg who sacrificed his time and energy to include others, who encouraged outreach within the community, and was a great mentor. Even though I only scratched the surface of who Bob was, his impact will not be forgotten.

To my starting labmates, the OGs and the NGs who supported and encouraged each other through discussion. I'd like to thank Dr. Melikhan Tanyeri for his training and mentorship during my time working on the hydrodynamic trap. Much appreciation to Utsav Agrawal for his collaboration on developing the SCM and performing painstaking calibrations. Arnab Mukherjee for his help and training in molecular biology. Chris Brockman for useful discussions, collaboration, and development of the automated hydrodynamic for single molecule DNA confinement. Folarin Latinwo for his calm and reassuring discussions. Thank you all for keeping the research experience "thought-provoking".

I'd like to thank the Kenis Lab for access to their cleanroom facilities and useful discussion regarding microfluidics.

I'd like to thank Professors Roderick Mackie and Isaac Cann for collaboration on the cell sorting application. Dr. Peiying Hong for conducting the whole genome application of the sorted cell sample.

Much appreciation to Tom Kuhlman who graciously agreed to serve on my committee and welcomed me into his lab through collaboration and mentorship.

My appreciation and gratitude to Professors Charles Schroeder, Bob Clegg, Su-A Myong, Zan Luthey-Schulten, and Tom Kuhlman for serving as my preliminary exam and defense committee members.

My appreciation and gratitude to Professors Emad Tajkhorshid, and Paul Selvin for graciously agreeing to serve on my defense committee on short notice.

I'd like to thank the Graduate College Office Educational Equity Programs for their support through the Summer Pre-Doctoral Institute and Graduate College Fellowship. I have met many helpful people including by not limited to; Ave Alvarado, Jessica Howard, Daniel Wong, and all the students I've met who commit and dedicate their time supporting success in others. Thank you all for making the graduate experience fulfilling.

I'd like to thank the past and current members of the Illinois Biophysics Society that I have worked with for their efforts in keeping the goals and vision alive. I look forward to witnessing the continued growth and progress in the future.

I'd like to thank the National Science Foundation through their support of a graduate research fellowship.

I'd like to thank those that I have missed through teaching and outreach, your influence and support will not be forgotten.

I'd like to point out that painstaking data collection and writing could not have been endurable without good music. The best album that carried me through those times of frustration and stress during my preliminary exam in 2012 is *Drink the Sea* by The Glitch Mob. I find it fitting in 2014 that their latest album *Love Death Immortality* assisted me in writing this thesis.

Finally, I would like to mention that my success at the writing of this thesis is a culmination of encouragement from mentors and research advisors throughout my education. I thank you all for your time and support. I look forward to giving back by mentoring and advising future students throughout my career.

Contents

Preface

This thesis describes the development of the single cell microbioreactor (SCM), a device capable of trapping and observing single cells over long time scales in fluctuating nutrient conditions. The SCM works by tracking a desired target cell in planar extensional flow then using feedback control to manipulate a stagnation point position in order to push the cell to the desired setpoint.

Chapter 1 describes the motivation for our work in developing the SCM for single cell gene expression. Chapter 2 provides background on the fluid flow and feedback control models implemented to trap cells for long time scales. Chapter 3 provides experimental detail regarding the generation and development of the SCM. Chapter 4 provides application specific details and results for cell sorting, cell growth, single cell gene expression, and intracellular diffusion. Chapter 5 ends with a comparison with other trapping techniques and potential applications for the SCM.

Overall, the SCM provides a non-perturbative method for single cell analysis under periodic nutrient conditions. Below is a list of publications that I have contributed to regarding the hydrodynamic trap and SCM:

1. Tanyeri, M., E.M. Johnson-Chavarria, and C.M. Schroeder. 2010. Hydrodynamic trap for single particles and cells. Appl. Phys. Lett. 96(22): 224101, doi:10.1063/1.3431664, PMCID: PMC2892531

2. Johnson-Chavarria, E.M., M. Tanyeri, and C.M. Schroeder. 2011. A microfluidic-based hydrodynamic trap for single particles. J. Vis. Exp. (47), e2517, doi:10.3791/2517, PMCID: PMC3182637.

3 Johnson-Chavarria, E.M., U. Agrawal, M. Tanyeri, T. Kuhlman, and C.M. Schroeder. 2014. Automated single cell microbioreactor for monitoring intracellular dynamics and cell growth in free solution. *Submitted.*

Chapter 1

Introduction

Single cell analysis has primarily been explored using external force fields such as optical, magnetic, or acoustic forces in order to trap target particles in solution. Moving beyond these techniques, we were inspired to extend the field by developing devices that use the sole action of fluid flow for trapping and manipulating target particles. In this Chapter, I introduce the motivation for our work towards developing a non-perturbative single cell microbioreactor (SCM) technique for single cell analysis.

1.1 Single cell gene expression

Gene expression varies from cell to cell and this accounts for differences found even in isogenic populations. These variations lead to different cell phenotypes and ultimately controls cell fate. By using single cells to better understand these variations we can create better cellular and intracellular models to elucidate disease progression, bacterial infection, or prognosis. The conventional method of cell analysis is through batch culture and bulk methods for analyzing population

dynamics. However, I will now discuss how single cell analysis reveals dynamics obscured by these batch methods.

Ensemble average measurements of gene expression obtained from bacterial populations conceal the intrinsic noise of a genetic regulatory network. In this way, ensemble measurements mask the dynamic response of different types of gene regulatory mechanisms such as positive and negative feedback loops, which can result in similar levels of protein expression from vastly different dynamics. Therefore, it is challenging to understand gene network dynamics from bulk averaged data analysis. This limitation has resulted in the need for single cell gene expression analysis.

Gene expression has been shown to be correlated with growth rates of cell populations. Interestingly, however, genes associated with cell division, such as *ftsZ* which is responsible for encoding a protein ring for bacterial cell division, are apparently observed to be unaffected by growth rates (1). Therefore, it has been proposed that chromosomal replication serves as an initiation for cell division. This is contrary to the widely held notion that a critical mass must reached by a cell in order to divide. Protein expression also plays a role in cell growth rates. Unnecessary or "gratuitous" expression may displace the resource allocation for the remaining cellular proteome. The fraction dedicated to ribosomal and associated proteins has been determined to be 0.55 and is growth rate independent (2, 3).

Stochastic gene expression is associated with the intrinsic noise due to low copy numbers of the molecules involved that gives rise to different levels of gene expression in a genetically identical cell population. This stochastic nature of gene expression has been quantified using fluorescent protein markers such as GFP, YFP, and CFP. These reporter proteins have been integrated downstream of target genes in order to quantify levels of expression. A system with absent or low levels of intrinsic noise should show correlation between levels of expression for

different genes. Experimentally, intrinsic noise has been observed using two fluorescent probes with identical promoters and wild type repressor lacI. However, with an inducible system, both proteins are expressed at similarly high levels thereby depicting low levels of intrinsic noise in the population average. In *Escherichia. coli* deletion of a DNA repair and maintenance gene (*recA*) or the addition of an oscillatory inducing network promotes the increase of intrinsic noise (4). In addition, further work has incorporated time lapse microscopy in order to study the effects of cell lineage on the intrinsic noise of a genetic network in *E. coli* (5).

Phenotypic switching in cells has been linked to the stochastic event of the *lac* repressor dissociating from DNA (6, 7). Cells that are uninduced have leaky or basal expression with low copies of a positive feedback gene. A burst in protein expression is required to switch to a fully induced state. Moreover, the switch is also dependent on inducer concentrations. As a result, bistability can be generated in a cell population (Fig. 1.1). This phenotypic heterogeneity of a genetically identical cell population is actually believed to benefit the population as a whole (8).

Frequency of changes in environmental conditions can lead to bacterial persistence, which is defined as the slow death or zero growth rate even in the presence of antibiotics, because most small molecule antibiotics require cellular growth to have an effect (9, 10). This particular case differs from bacterial resistance in which cells have genetically evolved to block or inhibit the effects of antibiotics and continue to proliferate.

1.2 Gene regulation in bacteria

Advances in cell cloning allow researchers to express genes under control of inducible promoters by molecular engineering plasmids. Plasmids are circular loops

of dsDNA similar to some prokaryotic chromosomes. Plasmids are considered replicons and can replicate independent of the host chromosome. Once a target gene sequence has been inserted into a plasmid vector, transformation is performed by making cell membranes permeable through methods such as heat shock, electroporation, and vesicle transport. Certain strains of bacteria have been isolated and engineered to provide ideal conditions for gene expression. These strains contain certain gene knockouts that facilitate adequate protein expression levels but may decrease growth rates compared to wild type.

Genes are sequences of DNA that code for a product such as proteins or RNA. In general, genes are regulated at the levels of transcription, RNA processing, and translation. However, bacterial mRNA is considered ready for translation almost as soon as transcription begins. Initiation of transcription is regulated by proteins that facilitate RNA polymerase binding to DNA. Termination is provided by sequences of DNA that prevent further transcription of RNA. Translation of mRNA to protein is performed by ribosomes which consist of many small proteins and large ribosomal RNAs. In prokaryotes the sequence of several genes under common control or regulation is called an operon (11).

The *Lac* operon is a sequence of genes responsible for the transport and metabolism of lactose in some enteric bacteria. This operon has been well identified in *E. coli* and has been modified by molecular engineering for target inducible gene expression. In the *lac* operon, three genes *lacZ*, *lacY*, and *lacA*, are regulated by a common promoter and main operator sequence (Fig 1.2). The metabolism of lactose is provided by *lacZ* which encodes for an enzyme β-galactosidase, digesting lactose into glucose and galactose. The transport of extracellular lactose into the cytoplasm is facilitated by lactose permease and is coded by *lacY*. The third gene *lacA* codes for transacetylase which transfers an acetyl group from acetyl-CoA to lactose. The functionality for this transfer is currently not fully understood. A

hypothetical role for this enzyme is for detoxification of non-metabolic β-galactoside analogs but a high affinity substrate has yet to be determined (12, 13).

Upstream of these three *lac* genes is the promoter and operator sequence that is trans modified by catabolite activator proteins (CAP) and *lac* repressor (lacI). The CAP complex consists of a protein that is allosteric, modified by the binding of cyclic adenosine monophosphate (cAMP). This cofactor concentration is increased in the absence of glucose and promotes binding to CAP which promotes CAP/*lac* promoter affinity. The CAP protein then facilitates binding of RNA polymerase to the *lac* operon. The operator is cis-acting on the *lacZYA* genes when it is trans modified by *lac* repressors. These repressors are tetrameric and are affected by the binding of lactose. When lactose or an analog is bound to the repressor, the repressor protein dissociates to a low affinity DNA sequence, which allows RNA polymerase to proceed with transcription of *lacZYA* (14).

1.3 Single cell approaches

Traditional approaches for studying gene expression have relied on high-throughput screening assays such as flow cytometry, which allows for single cell resolution (15). However, these methods typically require large volumes (≈ 1-10 mL) of cell culture and growth media, which may not be advantageous to limited sample volumes or fragile cell lines. In addition, flow cytometry provides information at an instant in time, rather than a dynamic time course of data from a single sample over long time scales.

Microfluidic fabrication has allowed researchers to design and build devices for single cells analysis, thereby enabling studies of gene expression (16), chemotaxis, enzymatic activity using chemical cytometry (17, 18), and cell sorting in free solution (19–23). Nutrient or chemical gradients can be readily generated in low Reynolds number laminar flows within microfluidic channels. Moreover, the

elastomeric properties of polydimethylsiloxane (PDMS) have allowed for fabrication of on-chip valves, which allows for flow metering and delivery of cells into microfluidic chambers or careful control over nutrient streams (24, 25). To this end, feedback control has been coupled with on-chip valves to generate an automated microfluidic Wheatstone bridge for on-demand capture of samples for rapid analysis (26). Microfluidic platforms have also been used to study chemotaxis via time-dependent control over chemical gradients (27). In addition, microcavities have been used to build single cell microarrays that allow for the adherence of one cell per cavity (28, 29) or many cells per chamber, including a mother cell and subsequent lineage (30).

The ability to integrate single cell experimental data and large-scale simulations for predicting whole cell phenotypes is a central goal in the field. Combined experimental and simulation-based approaches are required to understand the complex dynamics of cellular systems. Within a genetically-identical population of cells, intrinsic noise from gene expression can induce phenotypic heterogeneity. Recently, stochastic 'noise' within the *lac* circuit has been incorporated in a whole cell simulation (31, 32). In addition, chemotactic receptor adaptation times have been modelled to investigate optimal filtering as dictated by the cut-off frequency of a low-pass filter (33), which responds to low frequency but not to high frequency nutrient fluctuations. Interestingly, this type of response is essential for a cellular system to adapt or to sustain fitness in rapidly fluctuating environment conditions.

Overall, there is a critical need for development of improved techniques for single cell analysis. These methods can provide fundamentally new information on cell dynamic variation and can be coupled with large-scale models for holistic approaches to understanding genetic network dynamics. Current microfluidic-based approaches for single cell analysis can be classified into two categories: contact and non-contact based methods. Contact based methods for trapping

include barrier hydrodynamics and chemical and gel matrices (34, 35). Non-contact based methods isolate target cells by using optical, electric, acoustic, or magnetic fields (36, 37).

1.4 Methods for single cell confinement

Optical tweezers are a common method for non-contact particle trapping and are commonly used for single molecule and single cell experiments (38). Optical trapping allows for passive trapping of particles, wherein focused light enables confinement without the need for continuous feedback control (39). Recently, this method was used to study the chemotactic motion of single *E. coli* cells using a dual trap to confine the poles of a single cell (40). Min et al. furthered the use of this technique to observe run and tumble statistics of single *E. coli* cells (41). Although optical tweezers provide a convenient method for trapping, the use of a focused laser beam to confine living cells for long time scales has raised concerns about local heating and irradiative photo-damage to cellular structures (42). In prior work, potential damage to due to energy exposure was mitigated using an enzymatic oxygen scavenging system to generate growth anaerobic conditions, which minimized the formation of free radical singlet oxygen species (43).

Irradiative damage was also previously investigated by Ayano et al. using optical tweezers to transport single cells to micro-chamber arrays (44). These authors observed that continuous exposure of cells to 3 mW of laser illumination for 3 hr resulted in complete stoppage of cell growth. Indeed, light exposure to living cells during these experiments is considerable. As a reference, consider the use of time-lapse fluorescence microscopy to illuminate cells with a mercury arc lamp ($\approx$ 15 mW). Here, an exposure time of 0.25 sec (e.g., acquiring 15 frames at 60 fps) results in a total energy accumulation of 3.75 mJ across the field of view.

The reported lower limit of energy required for optical trapping focused at a specific target is ≈ 6 mJ (45).

The study of single cell gene expression has been advanced by the implementation of microfluidic fabrication. Microfluidic flow cells manually constructed from adhesive or parafilm sandwiched in between glass coverslips are commonly used in single molecule and single cell research. However, it is difficult to achieve small channel geometries (≈ 500 μm) using this approach, and these methods are generally limited in the ability to precisely control nutrient conditions in a rapid, reliable, and time-dependent fashion. Soft-lithography techniques using polydimethylsiloxane (PDMS) (46) have provided researchers across disciplines with rapid device prototyping for the confinement and analysis at the single cell level. We have utilized micro-channel fabrication to further develop the primitive flow method initially develop by G. I. Taylor using a four roll mill setup (47). Recently, this technique was used to manually trap and stretch single strands of DNA within microfluidic flow cells using coverslips (48) and has since been incorporated into a microfluidic PDMS device (49). The development of membrane pressure valves implemented using two-layer PDMS fabrication (25) has promoted the automation of this trapping technique.

Using contact based trapping methods, researchers have relied on advances in microfluidics to trap cells using hydrodynamic barriers. In these devices, cells are commonly captured in arrays while continuously exchanging media through the array (50), which allows for multiplexed screening of cells with nutrient exchange. In many cases, barriers are well suited to study cell-to-cell dynamics to large cell loading per well, rather than a single cell per trapping site. Researchers have also used non-contact hydrodynamic methods based on micro-eddies to trap cells, wherein rotational flow is used to confine cells within micro-vortices or against a pillar barrier. The forces exerted by these techniques have been reported to be ≈

30 pN with shear stresses ≤ 1.5 N m^{-2} (15 dyn cm^{-2}), which is comparable to arterial blood flow (37, 51, 52). Alternative non-contact methods have relied on magnetic force fields (53), acoustic traps (54), or homogeneous electric fields to trap particles. However, magnetic trapping of cells generally requires intracellular embedding of ferromagnetic particles, which can be perturbative. Moreover, electrokinetic trapping requires special considerations regarding the electrical conductivity of the media and may perturb cell membrane electrical potentials (55).

Overall, there is a strong need for development of new non-contact based methods for single cell analysis. In particular, new microfluidic platforms are required that allow for chemostatic growth environments of single cells, with the ability to control cellular growth media and to observe cell dynamics. In this thesis, I report the development of a single cell microbioreactor (SCM) that allows for the investigation of cell growth in free solution with the combined ability for time-dependent control over media conditions (Fig. 1.3). We use the SCM to characterize cell growth dynamics in free solution, and in all cases, single cell experiments are compared to bulk growth. In addition, we also use the SCM to investigate dynamic gene expression and intracellular spatial distributions of transcription factors in single bacterial cells under precise dynamic control over environmental conditions.

In short, with the dependence of gene expression on cell fitness and nutrient or inducer concentrations, there is a strong need to develop tools for non-perturbative manipulation, periodic stimuli induction, and chemostat capabilities in order to construct better gene regulatory models. Therefore, in this thesis I outline the development of our single cell microbioreactor (SCM) and its implementation for investigating gene expression in single cell bacteria under periodic environmental conditions in free solution.

1.5 Figures and tables

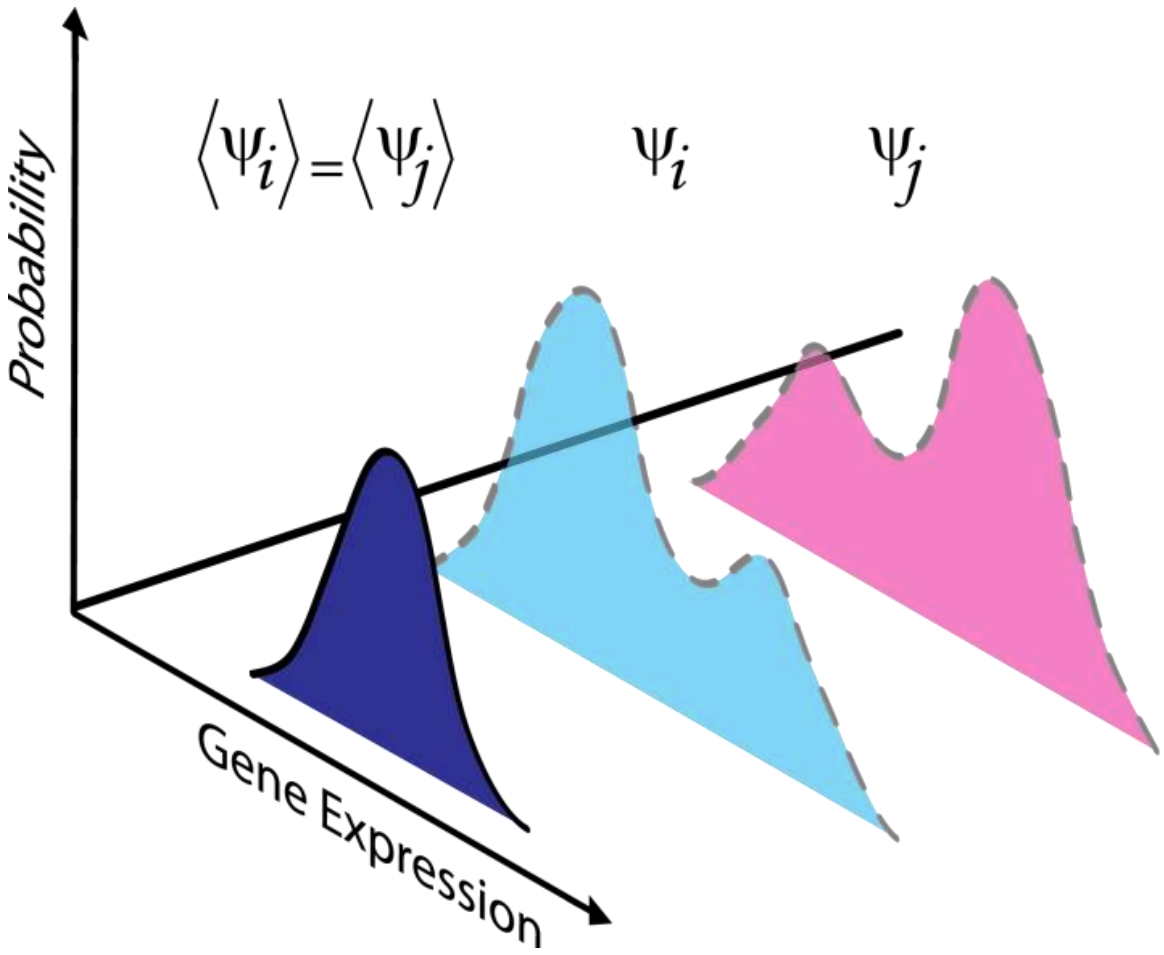

Figure 1.1: Ensemble average of two stable states shows an identical unimodal distribution. The probability of gene expression (ψ) at different states (i, j) from a genetically identical cell population can have ensemble averages that are equal (Dark blue distribution). Bimodal distributions are a special case of bistability. It has been shown that noise can induce bimodal distributions without bistability (56). Also, simulations have been shown to correlate the abandonment of bimodal distributions for unimodal distributions by bistable systems (57).

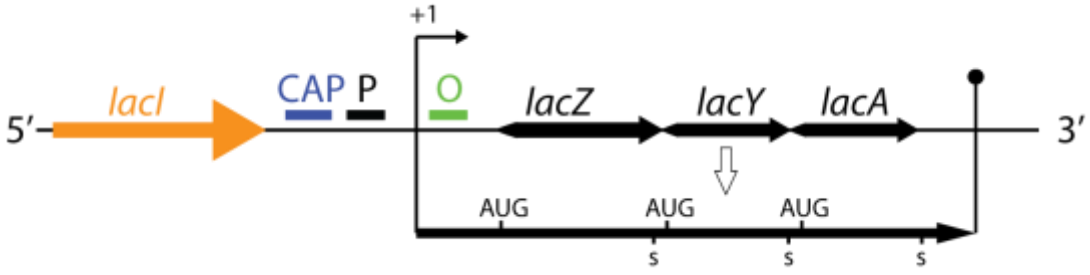

Figure 1.2: *Lac* operon. The cofactor cAMP binds the CAP protein recognition site and repressor lacI binds to the primary operator site (green) under high glucose concentrations and low lactose availability. Two auxiliary operators (not shown) are located between the end of *lacI* and CAP (O3) and O2 is 401 bp downstream of the primary operator site (green). All three operators are required for maximum repression in vivo (14). When lactose or a mimic such as IPTG is present then lacI dissociates from the binding site. This allows RNA polymerase to bind at the promoter and primary operator sequence for transcribing mRNA (lower line).

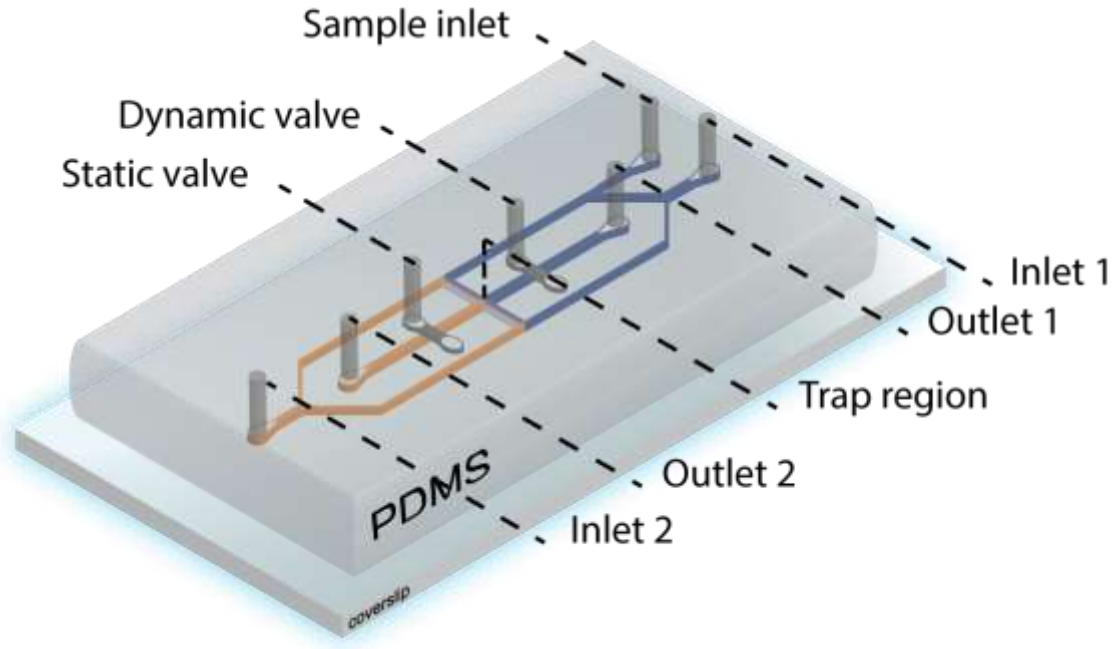

Figure 1.3: Microfluidic design of the single cell microbioreactor (SCM). We used standard two layer soft-lithography to fabricate microchannels with valve control. PDMS annealed layers (fluidic and control) were bonded to glass coverslips.

1.6 References

1. Wang, J.D., and P.A. Levin. 2009. Metabolism, cell growth and the bacterial cell cycle. Nat. Rev. Microbiol. 7: 822–7.

2. Lerman, J., and B.O. Palsson. 2010. Microbiology. Topping off a multiscale balancing act. Science. 330: 1058–9.

3. Scott, M., C.W. Gunderson, E.M. Mateescu, Z. Zhang, and T. Hwa. 2010. Interdependence of cell growth and gene expression: origins and consequences. Science. 330: 1099–102.

4. Elowitz, M.B., A.J. Levine, E.D. Siggia, and P.S. Swain. 2002. Stochastic gene expression in a single cell. Science. 297: 1183–6.

5. Rosenfeld, N., J.W. Young, U. Alon, P.S. Swain, and M.B. Elowitz. 2005. Gene regulation at the single-cell level. Science. 307: 1962–5.

6. Elf, J., G.-W. Li, and X.S. Xie. 2007. Probing transcription factor dynamics at the single-molecule level in a living cell. Science. 316: 1191–4.

7. Li, G.-W., and X.S. Xie. 2011. Central dogma at the single-molecule level in living cells. Nature. 475: 308–15.

8. Hong, S.H., X. Wang, H.F. O' Connor, M.J. Benedik, and T.K. Wood. 2012. Bacterial persistence increases as environmental fitness decreases. Microb. Biotechnol. .

9. Kussell, E., R. Kishony, N. Q Balaban, and S. Leibler. 2005. Bacterial persistence: a model of survival in changing environments. Genetics. 169: 1807–1814.

10. Kussell, E., and S. Leibler. 2005. Phenotypic diversity, population growth, and information in fluctuating environments. Science. 309: 2075–8.

11. 2007. Molecular Biology of the Cell [Hardcover]. Garland Science; 5 edition.

12. Lewin, B. 2000. Genes seven. Oxford University Press.

13. Roderick, S.L. 2005. The lac operon galactoside acetyltransferase. C. R. Biol. 328: 568–75.

14. Lewis, M., G. Chang, N.C. Horton, M.A. Kercher, H.C. Pace, et al. 1996. Crystal structure of the lactose operon repressor and its complexes with DNA and inducer. Science. 271: 1247–54.

15. Guido, N.J., X. Wang, D. Adalsteinsson, D. McMillen, J. Hasty, et al. 2006. A bottom-up approach to gene regulation. Nature. 439: 856–60.

16. Cai, L., N. Friedman, and X.S. Xie. 2006. Stochastic protein expression in individual cells at the single molecule level. Nature. 440: 358–62.

17. Kovarik, M.L., and N.L. Allbritton. 2011. Measuring enzyme activity in single cells. Trends Biotechnol. 29: 222–230.

18. Kovarik, M.L., P.K. Shah, P.M. Armistead, and N.L. Allbritton. 2013. Microfluidic chemical cytometry of peptide degradation in single drug-treated acute myeloid leukemia cells. Anal. Chem. 85: 4991–7.

19. Sia, S.K., and G.M. Whitesides. 2003. Microfluidic devices fabricated in poly(dimethylsiloxane) for biological studies . Electrophoresis. 24: 3563–3576.

20. Andersson, H., and A. van den Berg. 2003. Microfluidic devices for cellomics: a review. Sensors Actuators B Chem. 92: 315–325.

21. Vilkner, T., D. Janasek, and A. Manz. 2004. Micro total analysis systems. Recent developments. Anal. Chem. 76: 3373–85.

22. Ingham, C.J., and J.E.T. van Hylckama Vlieg. 2008. MEMS and the microbe. Lab Chip. 8: 1604–16.

23. Bennett, M.R., and J. Hasty. 2009. Microfluidic devices for measuring gene network dynamics in single cells. Nat. Rev. Genet. 10: 628–38.

24. Groisman, A., C. Lobo, H. Cho, J.K. Campbell, Y.S. Dufour, et al. 2005. A microfluidic chemostat for experiments with bacterial and yeast cells. Nat. Methods. 2: 685–9.

25. Unger, M.A., H.P. Chou, T. Thorsen, A. Scherer, and S.R. Quake. 2000. Monolithic microfabricated valves and pumps by multilayer soft lithography. Science. 288: 113–6.

26. Tanyeri, M., M. Ranka, N. Sittipolkul, and C.M. Schroeder. 2011. Microfluidic Wheatstone bridge for rapid sample analysis. Lab Chip. 11: 4181–6.

27. Meier, B., A. Zielinski, C. Weber, D. Arcizet, S. Youssef, et al. 2011. Chemotactic cell trapping in controlled alternating gradient fields. Proc. Natl. Acad. Sci. U. S. A. 108: 11417–22.

28. Hosokawa, M., T. Hayashi, T. Mori, T. Yoshino, S. Nakasono, et al. 2011. Microfluidic device with chemical gradient for single-cell cytotoxicity assays. Anal. Chem. 83: 3648–54.

29. Wang, Y., P. Shah, C. Phillips, C.E. Sims, and N.L. Allbritton. 2012. Trapping cells on a stretchable microwell array for single-cell analysis. Anal. Bioanal. Chem. 402: 1065–72.

30. Long, Z., E. Nugent, A. Javer, P. Cicuta, B. Sclavi, et al. 2013. Microfluidic chemostat for measuring single cell dynamics in bacteria. Lab Chip. 13: 947–54.

31. Roberts, E., A. Magis, J.O. Ortiz, W. Baumeister, and Z. Luthey-Schulten. 2011. Noise contributions in an inducible genetic switch: a whole-cell simulation study. PLoS Comput. Biol. 7: e1002010.

32. Assaf, M., E. Roberts, and Z. Luthey-Schulten. 2011. Determining the stability of genetic switches: explicitly accounting for mRNA noise. Phys. Rev. Lett. 106: 4.

33. Andrews, B.W., T.-M. Yi, and P.A. Iglesias. 2006. Optimal noise filtering in the chemotactic response of Escherichia coli. PLoS Comput. Biol. 2: e154.

34. Di Carlo, D., L.Y. Wu, and L.P. Lee. 2006. Dynamic single cell culture array. Lab Chip. 6: 1445–9.

35. Di Carlo, D., and L.P. Lee. 2006. Dynamic single-cell analysis for quantitative biology. Anal. Chem. 78: 7918–25.

36. Johann, R.M. 2006. Cell trapping in microfluidic chips. Anal. Bioanal. Chem. 385: 408–12.

37. Lutz, B.R., J. Chen, and D.T. Schwartz. 2006. Hydrodynamic tweezers: 1. Noncontact trapping of single cells using steady streaming microeddies. Anal. Chem. 78: 5429–35.

38. Neuman, K.C., and S.M. Block. 2004. Optical trapping. Rev. Sci. Instrum. 75: 2787–809.

39. Ashkin, A., J.M. Dziedzic, J.E. Bjorkholm, and S. Chu. 1986. Observation of a Single-Beam Gradient Force Optical Trap for Dielectric Particles. Opt. Lett. 11: 288–290.

40. Min, T.L., P.J. Mears, L.M. Chubiz, C. V Rao, I. Golding, et al. 2009. High-resolution, long-term characterization of bacterial motility using optical tweezers. Nat. Methods. 6: 831–5.

41. Min, T.L., P.J. Mears, I. Golding, and Y.R. Chemla. 2012. Chemotactic adaptation kinetics of individual Escherichia coli cells. Proc. Natl. Acad. Sci. U. S. A. 109: 9869–74.

42. Neuman, K.C., E.H. Chadd, G.F. Liou, K. Bergman, and S.M. Block. 1999. Characterization of photodamage to Escherichia coli in optical traps. Biophys. J. 77: 2856–63.

43. Landry, M.P., P.M. McCall, Z. Qi, and Y.R. Chemla. 2009. Characterization of photoactivated singlet oxygen damage in single-molecule optical trap experiments. Biophys. J. 97: 2128–36.

44. Ayano, S., Y. Wakamoto, S. Yamashita, and K. Yasuda. 2006. Quantitative measurement of damage caused by 1064-nm wavelength optical trapping of Escherichia coli cells using on-chip single cell cultivation system. Biochem. Biophys. Res. Commun. 350: 678–84.

45. Umehara, S., I. Inoue, Y. Wakamoto, and K. Yasuda. 2007. Origin of individuality of two daughter cells during the division process examined by the simultaneous measurement of growth and swimming property using an on-chip single-cell cultivation system. Biophys. J. 93: 1061–7.

46. McDonald, J.C., and G.M. Whitesides. 2002. Poly(dimethylsiloxane) as a Material for Fabricating Microfluidic Devices. Acc. Chem. Res. 35: 491 – 499.

47. Taylor, G.I. 1934. The Formation of Emulsions in Definable Fields of Flow. Proc. R. Soc. London.Series A, Contain. Pap. a Math. Phys. Character. 146: 501 – 523.

48. Schroeder, C.M., H.P. Babcock, E.S. Shaqfeh, and S. Chu. 2003. Observation of polymer conformation hysteresis in extensional flow . Science. 301: 1515–1519.

49. Brockman, C., S.J. Kim, and C.M. Schroeder. 2011. Direct observation of single flexible polymers using single stranded DNA. Soft Matter. 7: 8005.

50. Kim, M.-C., Z. Wang, R.H.W. Lam, and T. Thorsen. 2008. Building a better cell trap: Applying Lagrangian modeling to the design of microfluidic devices for cell biology. J. Appl. Phys. 103: 044701.

51. Chandrasekaran, A., and M. Packirisamy. 2008. Enhanced bio-molecular interactions through recirculating microflows. IET Nanobiotechnol. 2: 39–46.

52. Lin, C.M., Y.S. Lai, H.P. Liu, C.Y. Chen, and A.M. Wo. 2008. Trapping of Bioparticles via Microvortices in a Microfluidic Device for Bioassay Applications . Anal. Chem. 80: 8937–45.

53. Hosu, B.G., K. Jakab, P. Banki, F.I. Toth, and G. Forgacs. 2003. Magnetic tweezers for intracellular applications. Rev. Sci. Instrum. 74: 4158–4163.

54. Hertz, H.M. 1995. Standing-wave acoustic trap for nonintrusive positioning of microparticles. J. Appl. Phys. 78: 4845.

55. Cohen, A.E., and W.E. Moerner. 2005. Method for trapping and manipulating nanoscale objects in solution . Appl. Phys. Lett. 86: 93109.

56. To, T.-L., and N. Maheshri. 2010. Noise can induce bimodality in positive transcriptional feedback loops without bistability. Science. 327: 1142–5.

57. Shu, C.-C., A. Chatterjee, G. Dunny, W.-S. Hu, and D. Ramkrishna. 2011. Bistability versus bimodal distributions in gene regulatory processes from population balance. PLoS Comput. Biol. 7: e1002140.

Chapter 2

Background and Methodology

The hydrodynamic trap has the ability to confine target particles and cells without the need for external optical, magnetic, or acoustic forces. This technique relies on the sole action of fluid flow. The implementation of planar extensional flow for studying emulsion and biopolymers was originally developed in 1934 by G. I. Taylor with a four roll mill setup (1). Four independent rollers manually controlled could vary the flow field in order to generation planar extensional, shear, and rotational flow fields. Since, its inception, this technology has developed over years with computerized automation developed by Gary Leal for studying particle and drop dynamics in two-dimensional linear flows (2). Recently, this technique has been scaled down for use within a glass flow cell that could be mounted on a microscope. This microfluidic technique provided a direct method for studying the relaxation of single DNA molecules in extensional flow (3).

This technique has gained more utilization with the advent of soft-lithography for lab on a chip applications by Whitesides and the innovation for controlling microfluidic flow with elastomeric valves by Quake (4, 5). Through many iterations

of the development of this technique we were fortunate in our progress and I will discuss four key milestones in Chapter 3. In this chapter, I will provide an overview of our final implementation and the forces governing the trap's capabilities.

2.1 Overview of the single cell microbioreactor (SCM)

The single cell microbioreactor (SCM) consists of a microfluidic chip with auxiliary instruments for controlling fluid flow rate, outlet resistance, temperature, and image acquisition. These components all circumvent an inverted fluorescence microscope where the lab on a chip is mounted. We initially used custom LabVIEW software to integrate this technique for automated trapping of single fluorescent polystyrene beads (Spherotech). Using bright stable particles (i.e. no significant photobleaching or blinking) provided a simplistic trapping scheme for development and troubleshooting. Many iterations in microfabrication went into the development of this technique. We strived to keep designs simple as our intended purpose was to package this complete technique for dissemination across disciplines. We used standard two layer soft-lithography techniques to fabricate our microfluidic chip. While many iterations deviated from the simple mentality and provided interesting results, only those designs that were carefully planned and scrutinized before production gave consistent progress. While this statement is obvious, those design deviations provided enjoyment and encouragement during those periods of continued frustration.

The SCM provides automated trapping in the *xy*-plane with continued trap stability during nutrient exchange. Fig. 2.1 illustrates the components of the SCM. Two independent syringes mounted on syringe pumps (Harvard Apparatus, Cole Parmer) control the fluid flow and switch between different media conditions. There are currently two elastomeric valves positioned equal distance from the cross-

slot. One valve acts as the offset pressure and is static at a set value during the course of the experiment. The opposing valve is dynamic and is used to control the stagnation point. Below the microfluidic chip is a thermal plate that is regulated by water bath circulation. Our initial attempt for confining target particles was demonstrated with a simple proportional control model (6). By determining stagnation point position with corresponding dynamic pressure we could use a steady state offset pressure. This was fundamental importance of regulating target position however we quickly discovered that for longer observation time we would need to develop a more intuitive controller. This adaptive controller is at the heart of my work concerning implementation of the SCM for single cell analysis as will be discussed further in Chapters 3 and 4.

2.2 Microfluidic hydrodynamic trap

To achieve particle confinement using hydrodynamic trapping, we incorporated a cross-slot geometry into the design of the microfluidic device, as previously developed in our lab (6–8). The cross-slot flow geometry generates a planar extensional flow (Fig. 2.3), which is both irrotational and solenoidal as specified by the curl and divergence of the velocity vector field $\vec{V}$ at any point ($\nabla \times \vec{V} = 0, \nabla \cdot \vec{V} = 0$). This flow field can be specified by a velocity potential φ and stream function ψ:

$$\varphi = \frac{\dot{\varepsilon}}{2}(y^2 - x^2) \;\; ; \;\; \psi = \dot{\varepsilon} y x \tag{2.1}$$

where

$$\frac{\partial \varphi}{\partial y} = \frac{\partial \psi}{\partial x}, \qquad \frac{\partial \varphi}{\partial x} = -\frac{\partial \psi}{\partial y} \tag{2.2}$$

and the partial derivatives of the velocity potential or stream function yield the velocity vector components:

$$v_x = \frac{\partial \varphi}{\partial x} = -\frac{\partial \psi}{\partial y}, \qquad v_y = \frac{\partial \varphi}{\partial y} = \frac{\partial \psi}{\partial x} \tag{2.3}$$

The velocity vector is described as $\vec{V} = \dot{\varepsilon}\,(-x, y)$, where $\dot{\varepsilon}$ is the strain rate and x and y are the Cartesian coordinates along the inlet and outlet directions, respectively, relative to the stagnation point position. In brief, pressurization/de-pressurization of the on-chip control valve varies the flow resistance in one of the outlet channels relative to the opposing outlet stream, which allows for fine-scale control over the stagnation point position. In this way, single cells can be trapped in free solution by active flow control. Finally, it should be noted that cell trapping in 2D is achieved by controlling a single parameter (relative flow rates in an outlet channel along the extensional flow axis). The inlet flow direction (compressional axis) is a stable trapping direction, which does not require active feedback control. In this way, the flow field can be described as a saddle surface by the velocity potential function φ, wherein the outlet direction (extensional axis) is the unstable flow direction requiring active feedback control for trapping (Fig. 2.4).

2.3 Manipulating target particles

The conventional methods for confining target particles have been delegated to optical, magnetic and acoustic tweezers. Lasers have paved the way for researchers with precise control of target particles. Their ability for tracking and measuring forces of single molecules has provided many insightful discoveries on protein DNA interactions and processivity (9–11). Magnetic tweezers have also allowed manipulation of multiple particles with spatial-temporal arrangement capabilities (12–15). They have also provided the means to apply torque on cellular walls with

a magnetic bead (16). Acoustic tweezers have also provided a means for confining or aggregating target particles for manipulation and observation (17, 18). While all of these methods have opened up the possibility for single cell and molecule research, they have also inspired us to extend the field in free solution trapping using the sole action of fluid flow. The reasoning being is that these techniques have certain limitations when it comes to single cell analysis. For instance as briefly mentioned in Chapter 1 optical tweezers do not provide a direct method for long observation trapped of single cells without damage occurring. In concentrated solutions optical tweezers will aggregate cells into the trap potential. For magnetic tweezers the issue arises due to the magnetic field imposed on the cellular system which is not fully understood whether to cause detrimental perturbations (16). Acoustic tweezers also impose limitations due to thin layer metal deposition and patterning required for implementation in microfluidic systems. In addition, high frequency signals are needed in order to achieve potentials for spatial confinement without a flow field (19).

Overall these methods provide weak forces for confining target particles since the forces scale with the particle volume. To combat these limitations a electrophoretic method such as the ABEL trap was developed (20, 21). By applying voltage potentials to four nodes potential wells could be generated to confine target particles in solution. By generating quadrapolar fields electroosmotic flow can be generated to manipulate free diffusing particles in solution. However, the ABEL trap requires modifications to polydimethylsiloxane in order to increase the strength of electroosmotic flow. Even with these modifications using plasma discharge to make the surface hydrophilic, experimental quality diminishes within an hour due to the PDMS returning to its native hydrophobic state. In essence, the incorporation of glass flow cells and pH regulation is needed in order to maintain trapping potential. In addition, particle solutions needed to be dilute and

the user would need to wait extended periods of time until a particle reached the trap area for testing.

The hydrodynamic trap has the ability to trap target particles without any external forces mentioned above. Table 2.1 illustrates the differences between the trapping methods outlined in this section. The three conventional methods have forces scaling with the particle volume whereas electrophoretic and the hydrodynamic trap forces scale with the particle characteristic radius. This theoretically allows for a wider range of trapping objects from 10 nm to 100 μm with a smaller working force range. Using this approach with a passive trap in the compressional axis and active or feedback control loop in the extensional axis we can target single cell bacteria with strain rates ~1 s^{-1} and shear stresses two orders of magnitude lower than shake flasks (22, 23).

2.4 Feedback control

Feedback control has developed over the years and since the early 1900s proportional integral derivative (PID) controllers have been commercially available for industrial processes and manufacturing. Pneumatic valves also entered the market around this time and gain widespread use for industrial applications. Even with these latest industrial advances, early civilizations were implementing water level regulators similar to what is still currently used today. In your home appliances such as your stove, air conditioner, and water heater use some form of feedback control to maintain a desired condition set by the user. A simple control model was our first initial choice for developing our trapping scheme. In Fig. 2.2 the controller receives a desired control or set point y_{sp} from the user and then calculates an error or difference from the input signal y_m to produce an output signal p. This simple proportional controller output $p(t)$ is defined as:

$$p(t) = \bar{p} + K_c e(t) \tag{2.4}$$

where $e(t)$ is the difference between the set-point and the input signal, $\bar{p}$ is the steady-state offset pressure, and K_c is a gain value in order to translate the error value into a pressure response. The drawbacks of this initial controller was that it was sensitive to fluctuations of the flow field. In addition, a calibration curve was needed in order to find the linear response regime. These controllers will be discussed in greater detail in Section 2.6.

Many different feedback approaches have been used to regulate the spatial confinement of a single particle or cell. One first approach in the 1970s was to translate the whole system instead of the individual cell (24). This was accomplished by using a motorized *xyz* translation stage. First the target particle position was recorded in three dimension then the stage position was corrected in order to keep the particle in the focus plane. Alternatively, direct approaches rely on external force fields to manipulate the target particle within the system. Our approach was initially for *xy* manipulation and user input for adjusting the focus. In later iterations of our technique we incorporated automated piezo stage for focusing.

2.5 Fluid dynamics

For single phase flow, the motion fluid elements is defined using the Navier-Stokes equations and in vector form is defined by:

$$\rho\left(\frac{\partial \mathbf{v}}{\partial t} + \mathbf{v}\cdot\nabla\mathbf{v}\right) = -\nabla p + \mu\nabla^2\mathbf{v} + \mathbf{F} \tag{2.5}$$

where the left hand side represents inertial forces. The first and second terms on the right hand side are the pressure gradient and viscous forces which result from the divergence of the stress tensor. The last term $\mathbf{F}$ is the sum of other body forces

imposed on the flow field. Eq. 2.5 assumes that fluid is incompressible and Newtonian which generally can be applied to small molecule liquids. In addition, it is important to consider conservation of mass, which states that mass can neither be created nor destroyed within a system and the total energy is conserved. The continuity equation is a mathematical statement of conservation of mass this and is given by:

$$\frac{D\rho}{Dt} + \rho(\nabla \cdot \mathbf{v}) = 0 \tag{2.6}$$

For the determining the flow regime, we use a non-dimensional number called the Reynolds number. The ratio between convective and viscous effects in solution is given be the Reynolds number:

$$Re \equiv \frac{\rho UL}{\mu} \tag{2.7}$$

For low Reynolds numbers, we can approximate the fluid as being laminar. This means the fluid creates streamlines or parallel layers where no lateral mixing occurs by lateral diffusion (i.e. Taylor dispersion). For a stationary time point ($\frac{\partial \mathbf{v}}{\partial t} = \frac{D\rho}{Dt} = 0$) and going even further for low Reynolds numbers ($Re \ll 1$) where creeping or Stokes flow conditions are generated, then we can neglect the inertial term and Eqs. 2.5 and 2.6 become:

$$0 = -\nabla p + \mu \nabla^2 \mathbf{v} + \mathbf{F} \tag{2.8}$$

$$(\nabla \cdot \mathbf{v}) = 0 \tag{2.9}$$

These approximations simplify our solution and allow us to readily model this flow in 2D and 3D. The plot in Fig. 2.5 shows the velocity profile (*yz* slices) along the channel. The laminar flow profile remains consistent until reaching zero at the stagnation point ($\mathrm{v} = 0$ at $\mathrm{x} = \mathrm{y} = 0$).

2.5.1 Planar extensional flow

Planar extensional flow is generated by two inlets impinging at a cross-slot geometry. Fig. 2.3 shows the velocity map and streamlines for this flow field. As the fluid approaches the center of the geometry, it slows down ($\nu = 0$ at $x = y = 0$). Extending further from Eq. 2.1 we can describe the flow field in matrix form:

$$\begin{bmatrix} v_x \\ v_y \end{bmatrix} = \begin{bmatrix} -\dot{\varepsilon} & 0 \\ 0 & \dot{\varepsilon} \end{bmatrix} \begin{bmatrix} x - x_o \\ y - y_o \end{bmatrix} \tag{2.10}$$

where v_x, v_y are the velocity vector components in the x and y direction. The strain rate $\dot{\varepsilon}$ is calculated by using particle tracking of beads in solution using ImageJ software.

As briefly mentioned Chapter 1, this flow field has been used to drop dynamics and breakup under different strain rates in viscous solution (1, 2). This was also incorporated in the study of polymer relaxation of single and double stranded DNA in both glass and PDMS based flow cells (3, 25). After our prior work on developing the hydrodynamic trap (6), other groups found use in studying DNA sequencing using a manual trapping version (26). Also, biophysicists interested in cytoskeleton dynamics found great utilization of this flow field for studying actin polymerization and deformation *in vitro* (27). Exploiting this flow field, we were able to develop continuous particle manipulation and confinement under continuous or oscillatory flow conditions.

2.5.2 Stagnation point

With planar extensional flow at the center of the flow field is the region of great interest and importance. Defined by x_o and y_o in Eq. 2.7, the stagnation point is at the center of the cross slot assuming the outlets have equal resistance. Conservation of mass defines the movement of this stagnation point when outlet

flow rates are not congruent. When a pressure is applied to one of the outlet channels while keeping the resistance of the opposing outlet and inlet flow rate fixed, the stagnation point translates away from the path of least resistance. Essentially more fluid is directed toward the path of least resistance pushing the stagnation point away.

This method is analogous to the inverted pendulum problem, in the compressional axis the particle is passively trapped by the impinging fluid flow. In the extensional axis, the particle will move out of the stagnation point due to Brownian motion and flow perturbations. Brownian motion in one dimension can be described by the relation:

$$\langle x^2 \rangle = 2Dt \tag{2.11}$$

where D is the diffusion coefficient. The Einstein-Smoluchowski relation in conjuction with Stokes law for a spherical particle at low Reynolds numbers provides the diffusion coefficient:

$$D = \frac{k_B T}{6\pi\eta r} \tag{2.12}$$

where η is the viscosity of the fluid and r is the radius of the particle. Therefore the feedback frequency required for successfully trapping is calculated by rearranging Eq. 2.11 to form:

$$\frac{1}{t_x} = \frac{2D}{d_x^2} \tag{2.13}$$

where t_x is the response time of the feedback loop and d_x is the confinement constraint. Therefore, in the case where there is no bulk fluid motion, to keep the centroid of a 1 μm bead trapped within a 1 μm region in water ($\eta = 1\ cP$), the frequency of response will need to be at least $> \sim 1.8$ Hz. This translates to a reponse feedback time of $\approx$ 500 ms. The trap potential can be visualized by a

hyperbolic contour map of the velocity potential function in Eq. 2.1 (Fig. 2.4). This creates a semi-stable saddle point where the compressional axis and extensional axis are stable and unstable respectively.

2.5.3 Forces on target particle

To theoretically calculate the average stress exerted on a cell trapped at the stagnation point in a planar extensional flow, we analytically determined the velocity field and stress field for a spherical particle trapped at a stagnation point. Our assumptions were that the cell is spherical in shape with radius R and positioned symmetrically at the stagnation point, and creeping flow conditions are applicable (*e.g.*, low Reynolds number flow, $Re \ll 1$). Under these conditions, the pressure p and velocity field v_i are:

$$p = 5\mu R^3 \Gamma_{ij} \frac{x_i x_j}{r^5} \tag{2.14}$$

$$v_i = -\frac{5}{2} R^3 x_i \Gamma_{ml} \frac{x_m x_l}{r^5} + \frac{5}{2} R^5 \Gamma_{ml} \left[-\frac{1}{5r^5} (\delta_{il} x_m + \delta_{im} x_l + \delta_{ml} x_i) + \frac{x_i x_m x_l}{r^7} \right] + \Gamma_{ij} x_j \tag{2.15}$$

where the fluid viscosity is μ, the rate of strain tensor $\Gamma_{ij} = \dot{\varepsilon} x_j(-\delta_{i1} + \delta_{i2})$, and the origin is at the center of the sphere. The fluid velocity v_i is exactly zero at the surface of the sphere ($r = R$). Using the definition of the stress tensor σ_{ij}

$$\sigma_{ij} = -p\delta_{ij} + \mu \left(\frac{\partial v_i}{\partial x_j} + \frac{\partial v_j}{\partial x_i} \right) \tag{2.16}$$

and by performing the necessary gradient operations on the velocity vector, one can calculate the drag force F experienced on a hemisphere of the trapped object by integrating the stress vector $\sigma_{ij} n_j$ over one-half of the sphere. By performing this operation, we calculated that the flow force on one-half of the sphere is $F_{1/2} = 10\pi\mu\dot{\varepsilon}R^2/2)$. The average shear stress exerted on the trapped cell is then $\tau =$

$2F_{1/2}/A$, where A is the area of a cell. Assuming a strain rate $\dot{\varepsilon} = 1$ s^{-1}, a fluid viscosity of 1 cP, and a cell with ~1 um radius, we estimate an average shear stresses on the order of ≈1E-2 dyn/cm^2. This average shear stress within the hydrodynamic trap is two orders of magnitude lower than previously reported for batch culture in shake flask (≈4 dyn/cm^2) (22).

2.6 Particle tracking

During the trapping experiments, particles are confined by defining a region of interest (ROI). Because the compressional axis is stable, we define the ROI to be asymmetric that is long in the extensional and short in the compressional axis. Fig. 2.6 illustrates this concept for particle tracking. The methods of Gaussian fit feedback will be discussed further in Chapter 3. We provide a qualitative depiction of the Gaussian fit for particle center of mass in Fig. 2.7. As the particles fluorescence profile is plotted along the y-axis, the Gaussian fit updates the particles position at each iteration of the feedback control loop. By default the fitting algorithm will output the corresponding particles position to the nearest pixel. Care should be taken to change this to a double floating point numerical value as integer values will cause discretization in your plotted trajectory.

2.6.1 Tracking accuracy

For improved particle tracking with reduce the ROI to prevent extra particles from entering the field of view. In order to target a specific particle we implemented two different selection methods. The first method we chose to target only particles that were in close proximity to the center of the ROI (x_{sp} , y_{sp}). We iterated through the particle analysis array which by default orders particles based on their spatial location within the ROI. Particles in the top left corner are appending at

the beginning of the array and those in the bottom right corner appended at the end of the array. Using the total count of particles within our ROI we iterate through the array and probe for particle positions that best match (x_{sp}, y_{sp}). Using this method provided consistency until a particle enters the stagnation point right over the target particle. This causes errors in continued tracking of the original target particle. To circumvent this, I developed a second model for tracking target particles. This method probed the last iteration of the target particle position and only chose particles that matched. In addition, it also checked that the particles change in position was within an error tolerance. Therefore, particles rapidly entering the stagnation point even straight toward the stagnation point would be dismissed as there change in position was greater than the trapped target particle.

Tracking suffered ideally from maintaining particle focus. For bright stable particles the tolerance for out of focus images was greater than for tracking cells based on phase contrast. For cells more robust tracking methods had to be implemented including an edge detection algorithm. This method mapped deviations in greyscale pixels to determine the cells position. The best feature of this image operator was that it would also detect cells out of focus and provide time for the user to make adjustments. In phase contrast, the ideal image is a dark cell body with a bright "halo" around the cell. When cells become out of focus the body becomes brighter and the edge darker. This is why the edge detection operator within the IMAQ module of LabVIEW could still continue to track cells that became out of focus. Fig. 2.8 depicts our inline image processing workflow.

2.6.2 Measurement noise

Measurement noise is introduced by background fluctuations and detector noise. To circumvent those issues, we reduced the area over which we perform image

processing. We used the ROI as method to extract that region from the raw CCD image. This increased the speed at which image processing could be performed in-line and reduced the background noise of the image due to inhomogeneous field illumination.

For bright stable particles with very low background noise, tracking is robust since the polystyrene beads used do not photobleach or blink. The best accuracy a tracking system can achieve for a stationary particle is determined by the number of photons captured N in a time integral τ. This accuracy is defined by $\sigma/\sqrt{N}$, where σ is the width of the Gaussian point spread function (PSF) (28). This relation has been expanded to encompass detector and background noise by Yildiz et al. and Thompson et al. for tracking single molecules to within 1 nm accuracy (29, 30) as defined by the relation:

$$\sigma_\mu = \sqrt{\left(\frac{s_i^2}{N} + \frac{a^2/12}{N} + \frac{8\pi s_i^4 b^2}{a^2 N^2}\right)} \tag{2.17}$$

where the s_i is the standard deviation of the background b and a is the pixel size of the detector. In general, this variables of noise can be minized so that the limiting factor is N. However, in Chapter 3, I discuss implications of using PSF on the controller time delay.

2.7 Control theory

We initially began the project using the simplest control model than transitioned into a more adaptive controller. The standard block diagram for a closed feedback loop is illustrated in Fig. 2.9. The controller variable Y is an output of the systems response. To initialize the control you first must determine a set point value. Using this setpoint value the controller calculates the error using a transfer function

to convert back to the original input signal type. This error is than applied to the controller transfer function to calculate an output response (31).

2.7.1 Proportional control model

For proof-of-principle trapping of non-motile particles (˜2.2 μm diameter polystyrene beads), we used a simple proportional feedback controller (31):

$$p_i(t) = \bar{p} + K_c e_i(t) \tag{2.18}$$

where $\bar{p}$ is the offset pressure, K_c is the dimensionless proportional gain value, and e(t) is the error defined as:

$$e(t) = y_{sp} - y_m(t) \tag{2.19}$$

where y_{sp} and y_{m} are the set point and instantaneous cell centroid y-axis position, respectively. We found that the proportional controller resulted in robust and stable trapping for micron-sized and sub-micron particles, as previously demonstrated (6, 8, 25, 32).

2.7.2 Adaptive control model

Proportional only control models are prone to "ringing" or overshooting the setpoint value. Also, they require a calibration curve which translations valve pressure with stagnation point position within the linear regime. Therefore, we needed to develop a more intuitive controller for manipulating target cells for long time-scales. In the following discussion, when analyzing single cell images the origin of the Cartesian coordinate axis is the upper left corner of the image. The *y*-position increases from top to bottom, and *x*-position increases from left to right. The adaptive logic controller is based on a simple proportional controller, wherein:

$$p_i(t) = p_{i-1} + K_c e_i(t) = p_{i-1} + output \tag{2.20}$$

and

$$e(t) = y_{sp} - y_m(t) \tag{2.21}$$

where p_i is the updated pressure (to be applied to the on-chip valve), p_{i-1} is the value of the pressure from the prior iteration, K_c is the proportional gain, $e(t)$ is the offset error, y_{sp} is the set point value (trap center for cell in y-direction), and y_m is the cell center of mass position. The initial difference with this controller and Eq. 2.18 is that p_{i-1} is not fixed and does not require a calibration curve. The rule base for first determining the magnitude (G1,G2) of the gain K_c is defined as follows:

$$K_c = \begin{cases} G1 & if\ |e_{i-1}(t)| > |e_i(t)| \\ G2 & if\ |e_{i-1}(t)| \leq |e_i(t)| \end{cases} \quad ; \quad where\ G1 < G2 \tag{2.22}$$

We then proceed to determine the directionality of 'pushing' the target cell in either the $+y$ or $-y$ direction by using a Not Exclusive OR (XNOR) logic gate defined by the truth table (Table 2.2) where input A and B are defined by the inequalities:

$$A = \mathrm{e}_i(\mathrm{t}) < 0 \ = \ T\ or\ F \quad ; \quad B \ = \ |\, e_{i-1}(t)| \leq |e_i(t)| \ = \ T\ or\ F \tag{2.23}$$

and the output is defined as:

$$Output \ = \begin{cases} -K_c|e_i(t)|, & if\ A\ (XNOR)\ B = F \\ K_c|e_i(t)|, & if\ A\ (XNOR)\ B = T \end{cases} \tag{2.24}$$

With the origin of coordinate system set to be in the upper left corner of the image, the set of (x, y) positions are within the image plane.

Using this control logic, we can consider a few sample iterations of the controller. Assume that the control valve is situated below the cross-slot (*e.g.*, at $+y$ positions in the Fig. 2.6), and we choose the gain constant to have a positive initial value. Consider a trapped cell at the first position (1) above the set point

(at smaller y values) and moving away from the set point to position (2) so that A and B become F and T, respectively, then we determine the output to be $-G2|e_i(t)|$. Using Eqn (2.17), this results in a new applied pressure being smaller than the previous applied pressure, which moves the stagnation point above the target cell (*i.e.*, to smaller y values). This results in a net velocity of the cell toward the set point. On the next iteration, the target cell is at position (3), which has a smaller error than position (1). Therefore, A and B become F and F, respectively, resulting in an output $G1|e_i(t)|$. It is important to realize that the magnitude of this output is smaller than the output from the previous iteration. This is true given that $G1 < G2$, and the error has decreased. The resulting output of $G1|e_i(t)|$ creates a new applied pressure that is greater than the previous applied previous, thereby resulting in an applied velocity away from the set point. However, the applied velocity towards the set point will always be greater than the applied velocity away from the set point, given the controller logic conditions. This ultimately results in a net applied velocity toward the set point. As the $e_i(t) \rightarrow 0$, the resulting output magnitude will approach 0. The applied pressure will remain the same until target cell moves out of the stagnation point due to Brownian motion. The importance of this adaptive gain logic controller provides a slow controlled manipulation of the target cell toward the set point without overshooting the set point position (Fig 2.10).

2.8 Figures and tables

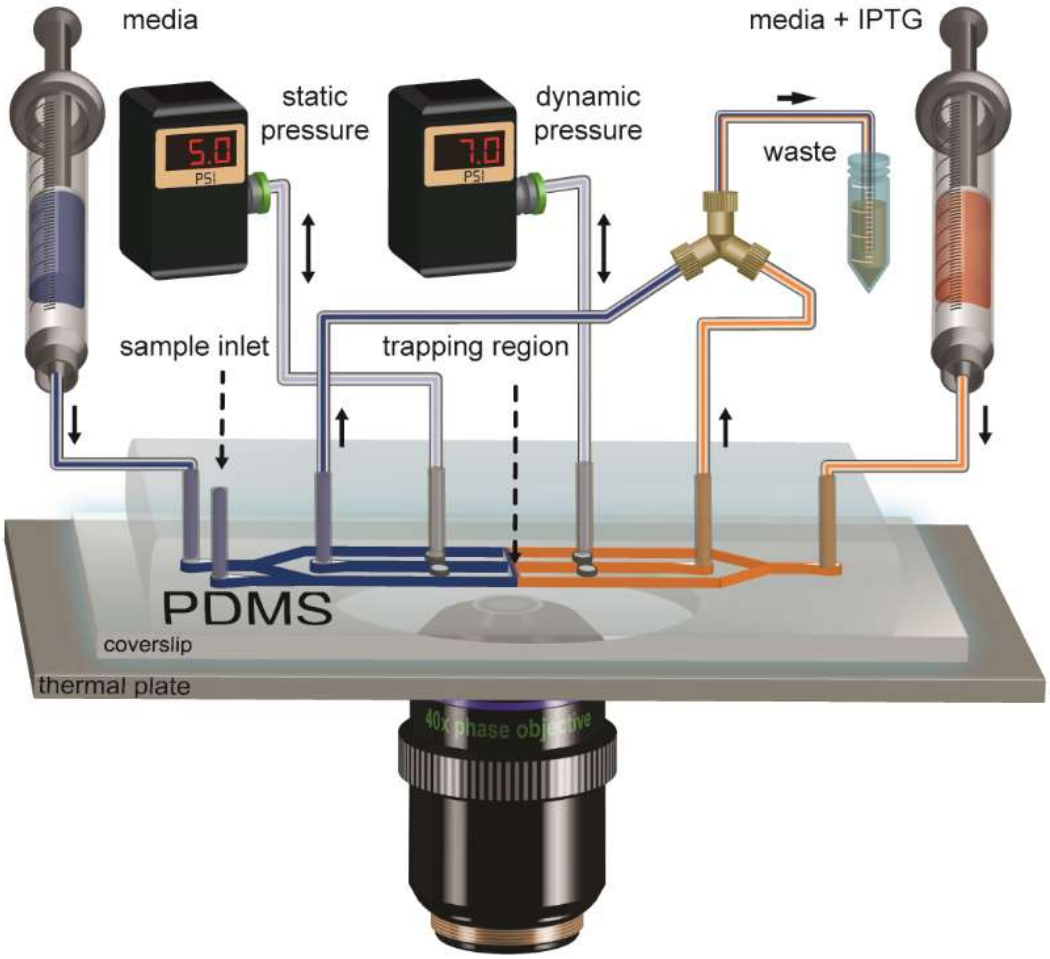

Figure 2.1: Experimental schematic of single cell microbioreactor (SCM). The integrated device consists of several key components, including: computer-controlled pressure regulators for controlling valve pressure, computer-controlled syringe pumps for delivering media into the device, and a thin-film thermal plate heater positioned underneath the device with thermocouple for controlling the temperature. The microfluidic platform is mounted on an inverted microscope equipped for phase-contrast and fluorescence imaging. The device allows for two distinct inlet media streams with a separate inlet for delivery of sample. Device components are integrated and controlled using a custom LabVIEW program.

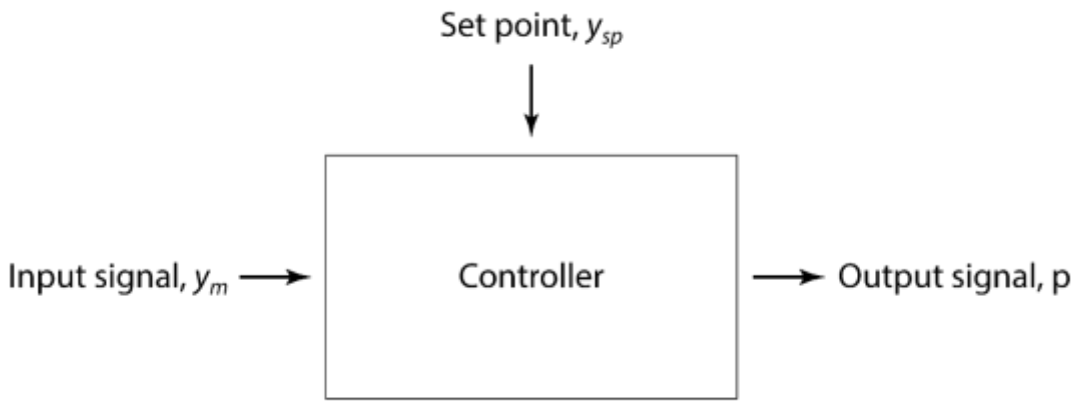

Figure 2.2: Schematic of a simple controller block diagram. Error is defined as the difference between setpoint and input signal. Output signal is the product of the error and a gain value.

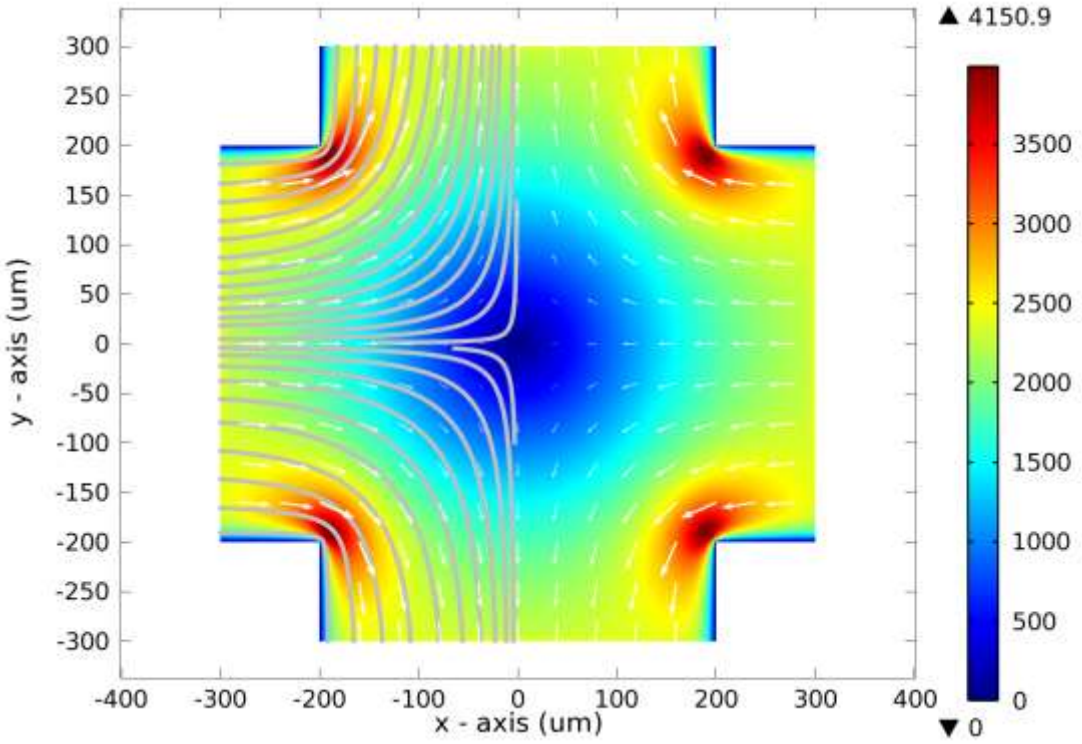

Figure 2.3: Velocity contour map for a cross-slot geometry. This CFD was performed with COMSOL using creeping flow (Re $\ll$ 1) and Q = 100 µl hr^{-1}

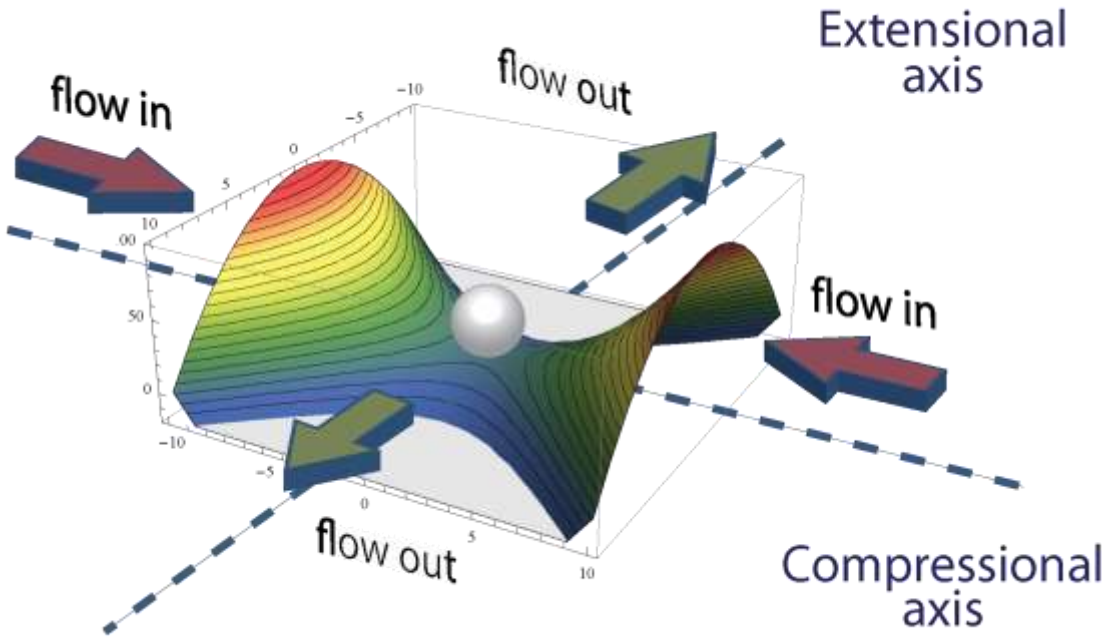

Figure 2.4: Velocity potential contour map. This color contour map depicts the velocity potential in Eq. 2.1. The compressional axis is a stable potential well and the extensional axis is a saddle point where active feedback control is required for trapping (6).

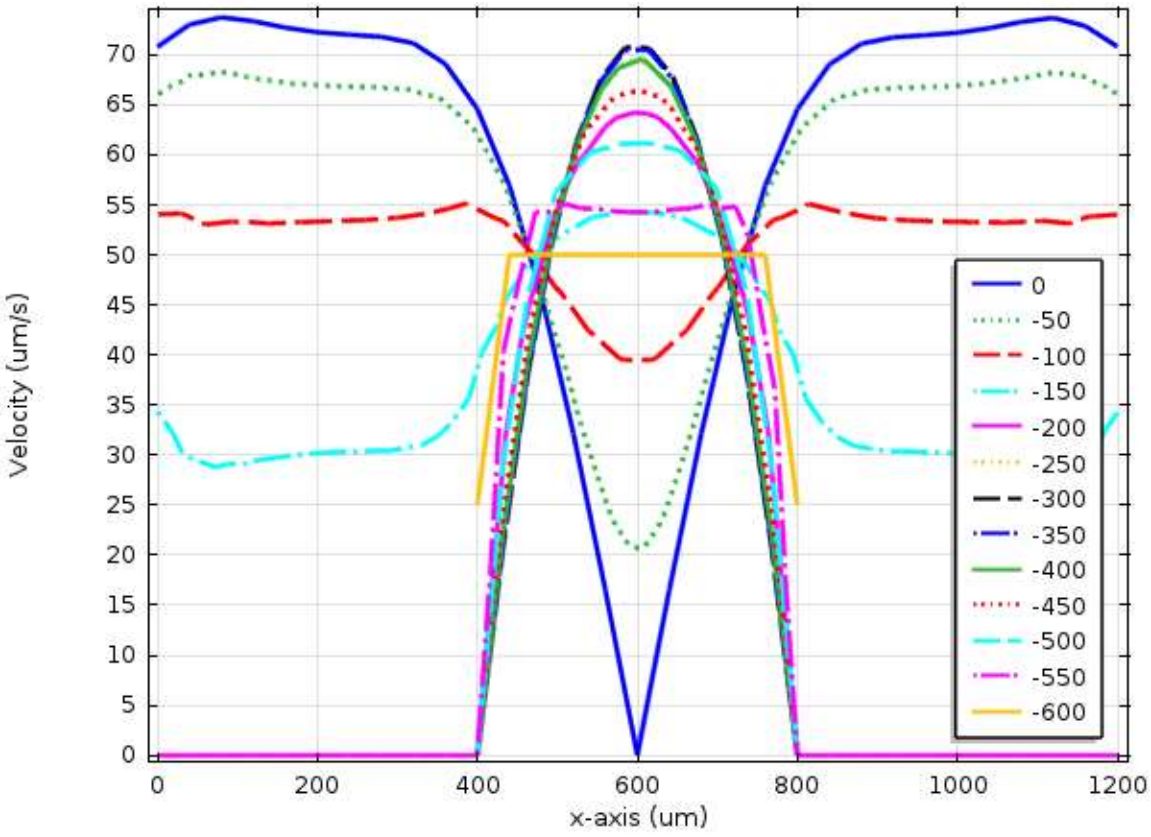

Figure 2.5: Velocity profile along *yz* channel cross-section. You can see the laminar flow profile along the channel until the velocity begins to decrease as it approaches the stagnation point. Each plot represents a different cross-section starting from -600 µm from the stagnation point. Channel dimensions are 400 x 30 µm with Q = 100 µl hr^{-1}

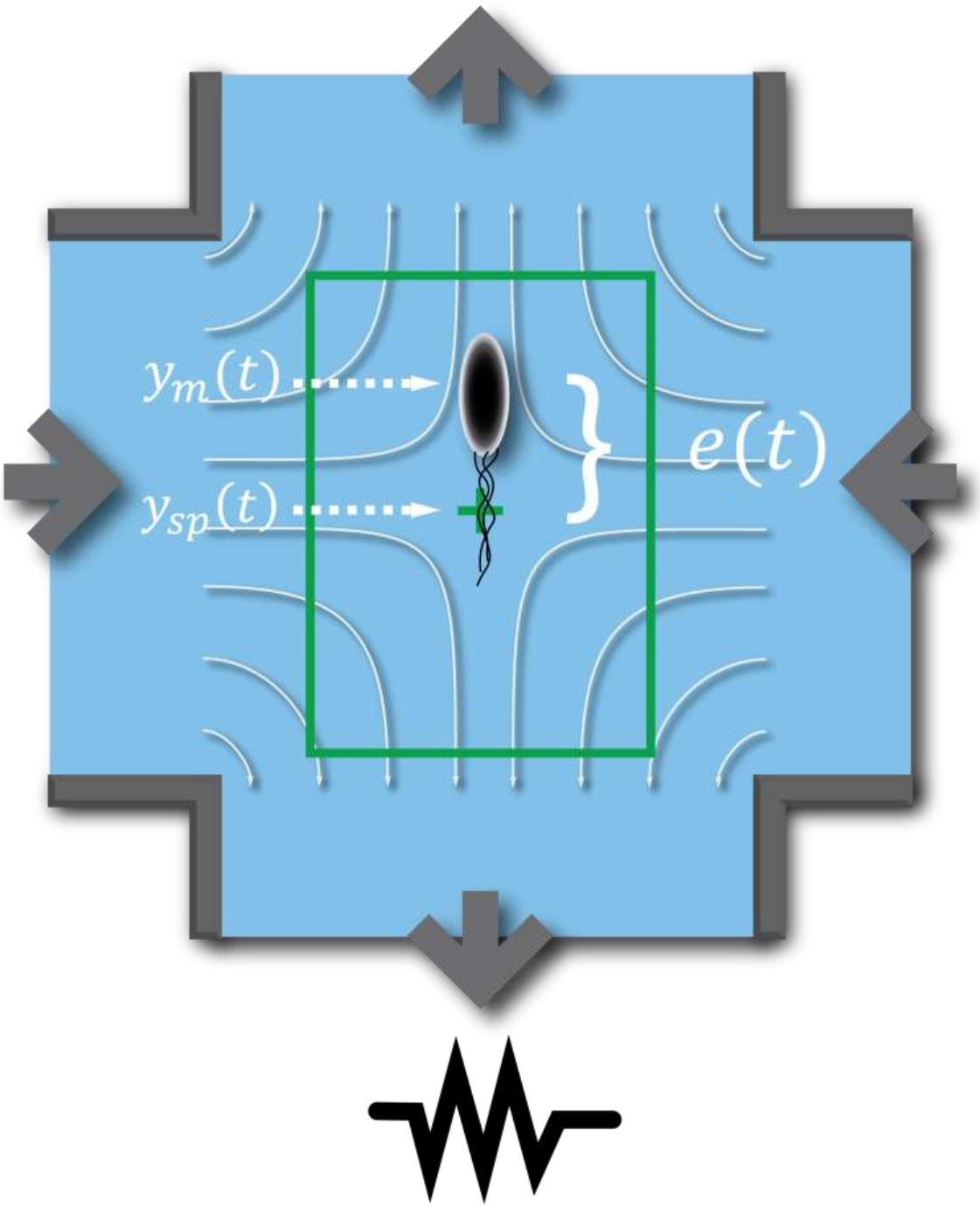

Figure 2.6: Cross-slot schematic displaying ROI and error. The user defines the ROI where the stagnation point is at the center. As the cell moves away from stagnation point the error is determined and used to calculate an output signal to bring the cell back to the desired setpoint.

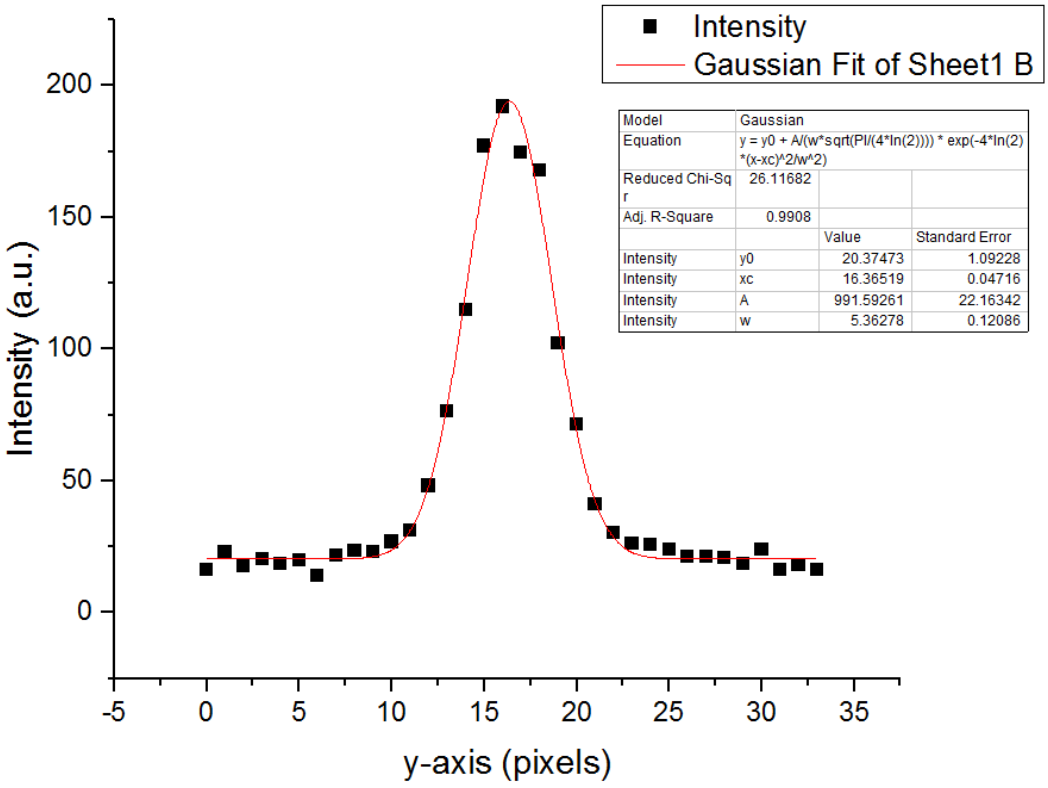

Figure 2.7: Fluorescence line scan profile across a fluorescent 2.2 µm bead. We fit a Gaussian to determine the peak location in y-axis and use this to define the location of the particle.

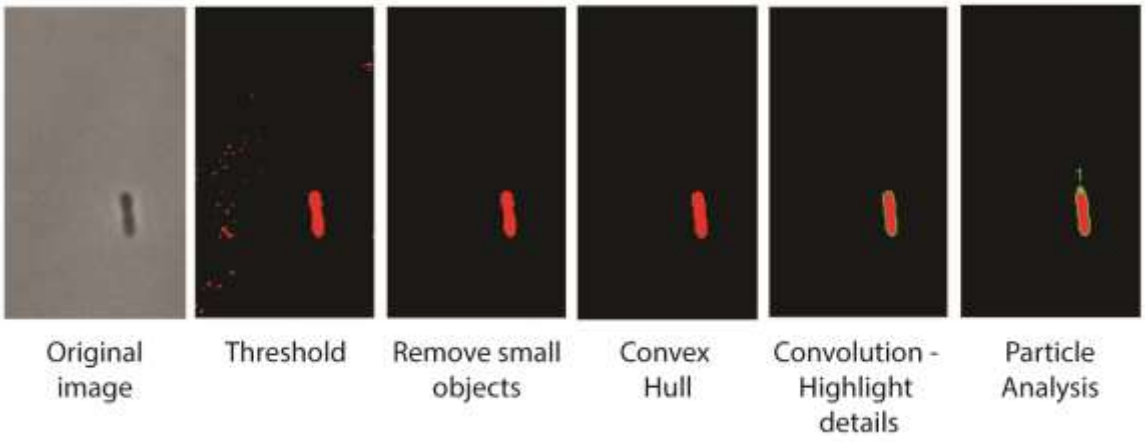

Figure 2.8: Inline image process algorithm for detecting the centroid position of a single cell. The process requires on the order of ˜3 ms to compute. Notice the clean background in the original image. This is due to modifications made to the channel geometry, discussed in Chapter 3.

Y = controlled variable
U = manipulated variable
D = disturbance variable
P = controller output
E = error signal
Ym = measured value of Y
Ysp = set point
$\tilde{Y}$sp = internal set point (used by the controller)
Yu = change in Y due to U
Yd = change in Y due to D
Gc = controller transfer function
Gv = transfer function for final control element
Gp = process transfer function
Gm = transfer function for measuring element and transmitter
Km = steady state gain for Gm

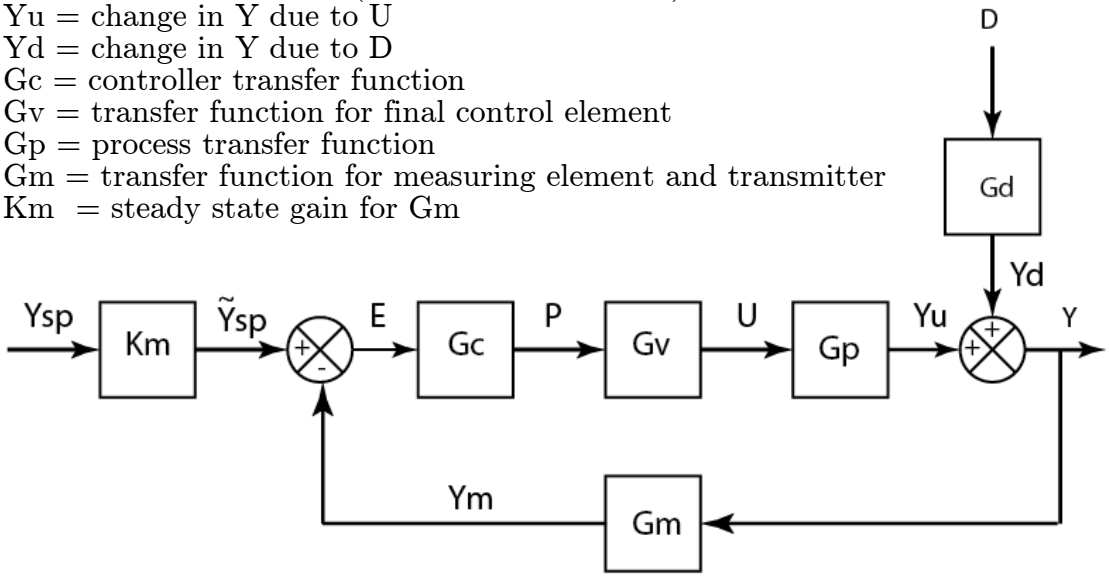

Figure 2.9: Schematic of a standard feedback control loop. The transfer functions G provide manipulation of the data stream to the appropriate units for use by the next process in the loop.

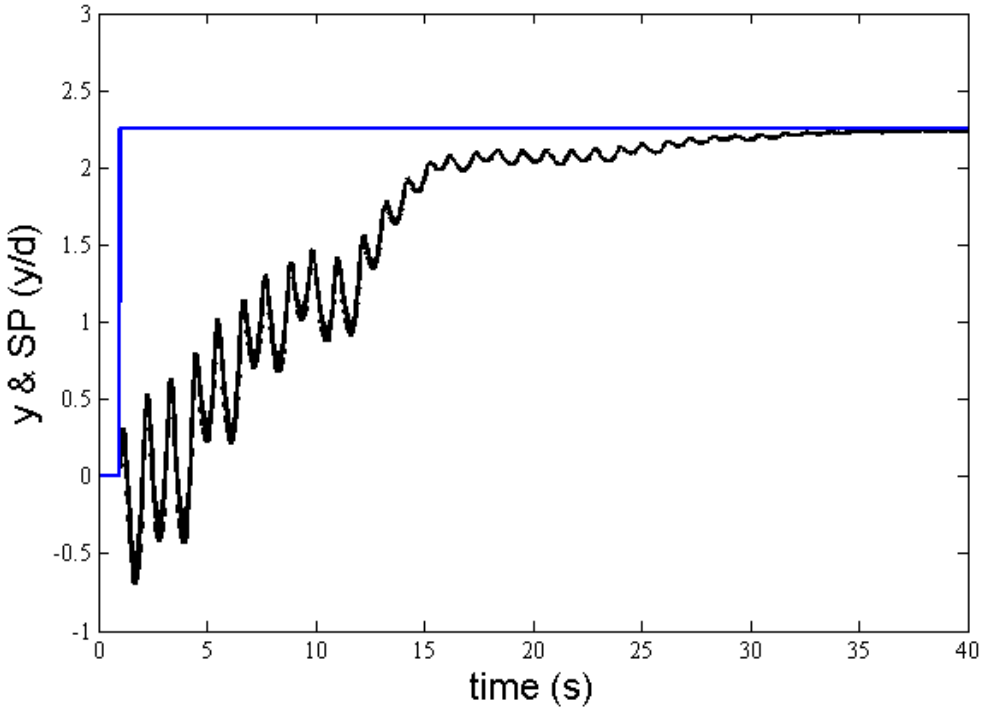

Figure 2.10: Adaptive controller simulation of trapped particle. Blue line indicates setpoint change from 0 → 2 and the black line is the trajectory of a 2.2 μm bead. Notice that the oscillations become smaller as the target approaches the setpoint. Gain parameters were G1 = 2 and G2 = G1*1.08.

Trapping Method	Stiffness (κ) (pN/nm)	Particle Size (μm)	Displacement[a] (nm)	Force (pN)	Force Scaling with Particle Size, R
Optical Tweezers	10^{-3}-1	0.05-10	2-100	0.1-100	R^3
Electromagnetic Tweezers	10^{-5}-10^{-4}	0.1-5	20-1000	0.01-10000	R^3
Diamagnetic Trap	~10^{-6}	1-100	~1000	0.01-1	R^3
Dielectrophoretic Trap	10^{-4}-10^{-2}	1-1000	20-200	0.1-100	R^3
Electrophoretic Trap	10^{-5}-10^{-4}	0.001-10	~100	0.005-500	R
Acoustic Trap	10^{-5}-10^{-4}	0.1-100	100-1000	0.1-400	R^3
Hydrodynamic Trap[b]	10^{-5}-10^{-4}	0.01-100	100-800	0.01-50	R

Table 2.1: Comparison of different trapping techniques. The hydrodynamic trap forces scale with the particle radius which allows for lower external force for trapping objects. This is important since the other three main methods of optical, magnetic an acoustic forces scale with the particle volume. (a) The average displacement of the cell from the trap center. (b) Indicates our hydrodynamic trap methods that we have developed.

.

INPUT		OUTPUT
A	B	
F	F	T
F	T	F
T	F	F
T	F	T

Table 2.2: XNOR truth table used by the adaptive controller.

2.9 References

1. Taylor, G.I. 1934. The Formation of Emulsions in Definable Fields of Flow. Proc. R. Soc. London.Series A, Contain. Pap. a Math. Phys. Character. 146: 501 – 523.

2. Bentley, B.J., and L.G. Leal. 1986. A computer-controlled four-roll mill for investigations of particle and drop dynamics in two-dimensional linear shear flows. J. Fluid Mech. 167: 219.

3. Schroeder, C.M., H.P. Babcock, E.S. Shaqfeh, and S. Chu. 2003. Observation of polymer conformation hysteresis in extensional flow . Science. 301: 1515–1519.

4. Sia, S.K., and G.M. Whitesides. 2003. Microfluidic devices fabricated in poly(dimethylsiloxane) for biological studies . Electrophoresis. 24: 3563–3576.

5. Unger, M.A., H.P. Chou, T. Thorsen, A. Scherer, and S.R. Quake. 2000. Monolithic microfabricated valves and pumps by multilayer soft lithography. Science. 288: 113–6.

6. Tanyeri, M., E.M. Johnson-Chavarria, and C.M. Schroeder. 2010. Hydrodynamic trap for single particles and cells. Appl. Phys. Lett. 96: 224101.

7. Tanyeri, M., M. Ranka, N. Sittipolkul, and C.M. Schroeder. 2011. A microfluidic-based hydrodynamic trap: design and implementation. Lab Chip. 11: 1786–94.

8. Johnson-Chavarria, E.M., M. Tanyeri, and C.M. Schroeder. 2011. A microfluidic-based hydrodynamic trap for single particles. J. Vis. Exp. : 1–5.

9. Qi, Z., R.A. Pugh, M. Spies, and Y.R. Chemla. 2013. Sequence-dependent base pair stepping dynamics in XPD helicase unwinding. Elife. 2: e00334.

10. Neuman, K.C., and S.M. Block. 2004. Optical trapping. Rev. Sci. Instrum. 75: 2787–809.

11. Landry, M.P., P.M. McCall, Z. Qi, and Y.R. Chemla. 2009. Characterization of photoactivated singlet oxygen damage in single-molecule optical trap experiments. Biophys. J. 97: 2128–36.

12. Lyuksyutov, I.F., A. Lyuksyutova, D.G. Naugle, and K.D.D. Rathnayaka. 2003. Trapping microparticles with strongly inhomogeneous magnetic fields. Mod. Phys. Lett. B. 17: 935–940.

13. Lyuksyutov, I.F. 2002. Nanoscale magnetic traps. Mod. Phys. Lett. B. 16: 569–576.

14. Gosse, C., and V. Croquette. 2002. Magnetic tweezers: Micromanipulation and force measurement at the molecular level. Biophys. J. 82: 3314–3329.

15. Hosu, B.G., K. Jakab, P. Banki, F.I. Toth, and G. Forgacs. 2003. Magnetic tweezers for intracellular applications. Rev. Sci. Instrum. 74: 4158–4163.

16. Tanase, M., N. Biais, and M. Sheetz. 2007. Magnetic tweezers in cell biology. Methods Cell Biol. 83: 473–93.

17. Evander, M., L. Johansson, T. Lilliehorn, J. Piskur, M. Lindvall, et al. 2007. Noninvasive acoustic cell trapping in a microfluidic perfusion system for online bioassays . Anal. Chem. 79: 2984–2991.

18. Hertz, H.M. 1995. Standing-wave acoustic trap for nonintrusive positioning of microparticles. J. Appl. Phys. 78: 4845.

19. Zheng, F., Y. Li, H.-S. Hsu, C. Liu, C. Tat Chiu, et al. 2012. Acoustic trapping with a high frequency linear phased array. Appl. Phys. Lett. 101: 214104.

20. Cohen, A. 2005. Control of Nanoparticles with Arbitrary Two-Dimensional Force Fields . Phys. Rev. Lett. 94: 118102.

21. Cohen, A.E., and W.E. Moerner. 2005. Method for trapping and manipulating nanoscale objects in solution . Appl. Phys. Lett. 86: 93109.

22. Fridley, K.M., M.A. Kinney, and T.C. McDevitt. 2012. Hydrodynamic modulation of pluripotent stem cells. Stem Cell Res. Ther. 3: 45.

23. Lutz, B.R., J. Chen, and D.T. Schwartz. 2006. Hydrodynamic tweezers: 1. Noncontact trapping of single cells using steady streaming microeddies. Anal. Chem. 78: 5429–35.

24. Berg, H.C. 1971. How to track bacteria. Rev. Sci. Instrum. 42: 868–71.

25. Brockman, C., S.J. Kim, and C.M. Schroeder. 2011. Direct observation of single flexible polymers using single stranded DNA. Soft Matter. 7: 8005.

26. Dylla-Spears, R., J.E. Townsend, L. Jen-Jacobson, L.L. Sohn, and S.J. Muller. 2010. Single-molecule sequence detection via microfluidic planar extensional flow at a stagnation point. Lab Chip. 10: 1543–9.

27. Kantsler, V., and R.E. Goldstein. 2012. Fluctuations, Dynamics, and the Stretch-Coil Transition of Single Actin Filaments in Extensional Flows. Phys. Rev. Lett. 108: 038103.

28. Selvin, P.R., T. Lougheed, M. Tonks Hoffman, H. Park, H. Balci, et al. 2007. Fluorescence Imaging with One-Nanometer Accuracy (FIONA). CSH Protoc. 2007: pdb.top27.

29. Yildiz, A., and P.R. Selvin. 2005. Fluorescence imaging with one nanometer accuracy: application to molecular motors. Acc. Chem. Res. 38: 574–582.

30. Thompson, R.E., D.R. Larson, and W.W. Webb. 2002. Precise nanometer localization analysis for individual fluorescent probes. Biophys. J. 82: 2775–83.

31. Seborg, D.E., T.F. Edgar, and D.A. Mellichamp. 2003. Process Dynamics and Control. Wiley.

32. Tanyeri, M., and C.M. Schroeder. 2013. Manipulation and confinement of single particles using fluid flow. Nano Lett. 13: 2357–64.

Chapter 3

Experimental Methodology

In this chapter, I discuss the development of the hydrodynamic trap into the single cell microbioreactor. I will discuss four generations with changes in geometry, particle tracking and controller implementation. I will leave more detailed experimental procedures for discussion in Chapter 4. Now I turn the focus towards the general advances for the majority of my research in developing the hydrodynamic trap for single cells. The methods outlined here can generally be applied to almost any cross-slot geometry.

3.1 First generation microdevice: Particle trap

The initial development of the hydrodynamic trap commenced with a simple two inlet and two outlet channel geometry arranged in a cross-slot fashion. This quickly spurred disadvantages as our sample could not be turned off readily. It was important that our initial bead concentration was not to dilute to allow for continuous testing and honing of the trapping parameters. In addition, over

concentrated solutions provided problems in tracking a single bead at a time. We therefore modified our channel geometry to incorporate a flow focusing sample inlet. To control the stagnation point position elastomeric valves were used to apply pressure and constraints to the channel cross sectional area. These valves were not added independently. They were a result of soft-lithography fabrication steps taken to implement their function. This innovation for valves on chip were originally introduced by Quake (1). For testing and tuning purposes we used bright Nile red fluorescent polystyrene beads. Fluorescence excitation was conducted using a mercury arc lamp (Olympus). A filter cube with excitation wavelength centered around 550nm, dichroic at 532 nm, and emission long pass filter at 545 nm was used to capture the entire emission spectrum of the fluorescent bead. This was important since were initially using a CCD camera (AVT) and wanted to ensure frame rate acquisition above 30 fps.

For introducing fluid flow we used one syringe pump (Harvard Apparatus) that was easily integrated into LabVIEW using custom code available from the manufacturer. Also, a template code was used and adapted from the LabVIEW code exchange for PHD2000 (Harvard Apparatus). To ensure equal flow rate from all four inlets on our microfluidic chip we used a four way junction (Upchurch scientific). The sample bead solution was also injected via syringe pump and regulated by a T-valve.

Before manipulating the pressure valves, water was forced into the cavity to remove any residual air. The pressure lines were filled with water to prevent air from diffusing through the thin membrane and into the micro channel. Before experiment tests began distilled deionized water (ddH_20) with 0.01% v/v Triton X100 (Sigma-Aldrich) was used to fully wet the microchannel and prevent beads from adhering to the surface. Once all external equipment was set, the device was pressurized by blocking all outlets with pin needles and forcing fluid into the

system. Any remaining trapped air or bubbles in the microchannel was forced into the PDMS. Outlet lines were added and combined into a waste reservoir at same height and length to ensure no added pressure difference was introduced.

3.1.1 Two layer PDMS microfluidic device

Using standard soft-lithography techniques we implemented a two layer fabrication scheme to include elastomeric valves. We patterned two 3 inch silicon wafers with negative photoresists (MicroChem) using a 5080 dpi transparency mask (University of Illinois printing). One wafer was used for the fluidic channels and the second for the valve layer. By defining the photoresist channel height and PDMS thickness we could establish an overheard membrane thickness. We found that a 30 μm channel height and 70 μm PDMS thickness provided sufficient linear response of the valve pressure and stagnation point position. The valve layer was confined to a 100 μm for easy visualization of feature edges for hole punching of inlets and aligning two PDMS layers. The different layer thickness is illustrated in a cross-section slice of the PDMS device before plasma bonding to a coverslip (Fig 3.1). Overall the whole assembled microfluidic PDMS chip was kept to a thickness of ~ 5 mm. This thickness ensures stable inlet and outlet ports for adding PFA microfluidic lines (Upchurch Scientific) with 24 gauge metal fittings (School of Chemical Sciences, Machine Shop). Full details on the fabrication of this microfluidic device is provided in Section 3.7

3.1.2 Flow focused geometry

In order to provide a steady sample stream to the cross-slot we incorporated a flow focus with two inlet channels at 30^{o} to sample stream plane. On the left side of side of the geometry where the sample inlet was placed we could readily observe

unequal distribution of flow. This was seen be a shift in the sample stream or lack thereof. These unbalanced inlet streams were due to trapped air or bubbles off chip. The four way junction would cause instabilities if not properly flushed. In addition trapped solution at each metal fitting would cause resistance in that inlet stream. Therefore to ensure equal volumetric flow rates from all inlets the device was flushed with volumetric flow rates up to ~5000 μl hr^{-1} for ~30 s. Fig. 3.2 illustrates this channel geometry with flow focus.

3.1.3 Gaussian fit feedback

For determining the centroid of our target fluorescent particle we used a best fit of the maximum emission count in the y dimension. After, defining a region of interest (ROI) with a rectangle box the coordinate space origin was fixed in the upper left corner of the ROI. The ROI was placed so that the center was at the stagnation point for an initial valve pressure Beads were not tracked until reaching the extensional axis where the stagnation point lies. An intensity profile along this extensional axis was recorded in real time. With the intensity data stream we used the general Least Squares (LS) method for fitting to a Gaussian curve (Fig 2.7) in the form of:

$$f = a \cdot e^{\left(-\frac{(y-y_o)^2}{2\sigma^2}\right)} + c \tag{3.1}$$

where a is the amplitude, y_o is the center of the particle along the y-axis (*i.e.* extensional axis), σ is the standard deviation, and c is the offset. Since our target particle was bright and stable, the LS method provided sufficient fitting for determining x_o by minimizing the residue of the fit with the following formula:

$$\frac{1}{N}\sum_{i=0}^{N-1} w_i\,(\mathcal{F}_i - f_i)^2 \tag{3.2}$$

where N is the length of f (in this case intensity values), w_i is the i^{th} element of the the weight, $\mathcal{F}_i$is the i^{th} element of the best Gaussian fit, and f_i is the i^{th} element of f. However, for a dim fluorescent particle or target such as for a single molecule where background noise may contribute to outliers in the fitting a Least Absolute Residual may be more appropriate. Additionally, a point spread function (PSF) could be used over the entire image to fit a 2D Gaussian could be incorporated (2). However, since we are dealing with inline image processing in real-time for feedback control the time required for fitting the PSF as well as the low frame rate required for sufficient photon capture would significantly decrease our feedback frequency.

3.2 Second generation microdevice: Cell sorting

The next undertaking was application directed as we sought to sort non-fluorescent target particles from a heterogeneous mixture. Fig. 3.3 illustrates the additions to the first generation for accomplishing this goal. On the outlet channels extra valves we placed in order to direct fluid to a specific bypass channel for collecting the target sample or sorted particle. Initially, the sample was introduced via flow focusing to the cross-slot. The flow rates were kept comparably low at ˜$10 - 20$ μl hr^{-1} in order to provide sufficient time for the user to select the desired target particle for capture. Once the desired particle entered the field of view, a ROI was created around this target and translated to the center or stagnation point. As the target particle was actively trapped, the ROI was minimized to reduce any tracking deviation of the controller to an alternate particle. Flow rate was gradually increased to wash out extraneous sample mixture while adjusting controller gain parameters to maintain trap stability of the target particle. After sufficient time to remove any remaining sample mixture, the outlet channel valves were

compressed and the bypass was opened. Fluid flow along with target particle were sorted to the bypass channel and collected in a separate collection tube.

3.2.1 Phase image processing

Until now I have outlined the ideal case for a bright fluorescent stable particle. This ideal case minimizes the background noise contribution when implementing a controller for particle tracking. However, most desired samples of interests, especially cells, do not have sufficient intrinsic fluorescent properties to determine centroid position. Different stains and membrane dyes can be incorporated in order to track via fluorescence. However, this puts limitations on studies of the behaviour of the cell since some of these stains (*e.g.* DAPI) affect cellular activity (3). Furthermore, constant irradiation of bound dye would either photobleach and/or cause irradiative damage to bound cellular structures (4, 5). To prevent cellular damage, we opted to incorporate phase contrast imaging for detecting cell centroid. Phase contrast imaging is a form of brightfield microscopy with the addition of a condenser and annulus for creating a phase shift (δ) which is determined by the relation:

$$\delta = \frac{2n_m\Delta}{\lambda} \tag{3.3}$$

where n_m is the refractive index of the medium, λ is the wavelength of incident light and Δ is the optical path difference (OPD $= (n_s - n_m)t_s$). Phase shifts are invisible to the eye however the Nobel winning invention by Frits Zernike in 1934 changed this by incorporating the annulus to translate a variation in phase into a change in amplitude displaying a high contrast image. Using phase contrast we are able to produce a high contrast image of a transparent bacteria. This enables us to perform threshold image processing to calculate the centroid. Fig. 2.8

illustrates our inline image processing for particle detection and centroid determination.

3.2.2 Particle sorting

Many techniques including the original Beckman flow cytometer paved the way for rapid screening of sample cells (6). A specific fluorescent indicator could be added to the sample preparation in order to screen for certain cellular properties (7–9). Since this innovation many developments have incorporated sequential sorting of detected target cellular phenotypes or characteristic. By incorporating a magnetic fluid or emulsion the target cell could be translated into a specific collection stream with an applied electrical field. While these methods provide high throughput screening and sorting, our approach was to enable visualization for deciding on the desired target cell. The user can visualize in real – time the sample solution without added staining to detect the desired cellular morphology. This enabling technology provides usefulness to field samples with heterogeneous cellular composition. We make no claims towards the high-throughput capabilities of our technique. However, cell sorting in the hydrodynamic trap was our first step towards providing a technique that can be implemented without the high cost of flow cytometry methods.

3.3 Third generation microdevice: Cell growth

Our next objective was to trap single cell bacteria for extended periods of time in order to study growth within the hydrodynamic trap which will be discussed further in Chapter 4. For observing a target particle over long time scales we wanted to simplify our channel geometry. We combined all of our initial inlets into one inlet which split into two streams on chip to generate the left and right

impinging fluid flow at the cross-slot. We added a sample inlet at the left impinging flow elbow. I initially tried to incorporate flow focusing upstream, however this proved unsuccessful causing flow instabilities as well as provided sharp channel features which were prone to clogging.

Before sample introduction the device was flushed with 0.01% Triton X 100 and then bovine serum albumin (BSA) 1 mg/ml was added to coat the channel surface to prevent cells from adhering to the surface. In the previous generation of our design temperature control was not needed as the heterogeneous sample mixture was fixed in EtOH. However, for live cell imaging and growth with added thin film heating elements underneath the device coverslip. We calibrated this temperature by plating cells on the surface and adjusted controller settings until we were able to observe optimal growth conditions. Fig. 3.4 displays our calibration for temperature control.

3.3.1 One inlet geometry

Combining the fluid flow and regulating the fluid streams on chip provided continued stability over extended periods of time. Fig 3.5 illustrates the one inlet channel geometry used for this long term observation trapping. This allowed for trapping single bacteria cells for growth studies. By using one inlet we negated the use of the four way junction off chip for a single inlet tubing. This significantly reduced setup time and also reduced air or bubble formation upstream.

3.3.2 Long observation trapping

Over the course of an experiment fluid parameters would fluctuate. This was attributed to the mechanical nature of the syringe pump. Since our fluid flow was volumetric at ~100 μl hr^{-1} pressure within the device would vary. Mechanically driven syringe pumps have the tendency to produce pulse flow. This would cause

an unsteady fluid flow rate over time. Care was taken to ensure the mechanical drive train of the syringe pumps was well lubricated with PTFE grease to reduce this pulse flow effect. In addition, the quality of flow rate produced varied depending on the position of the drive train during the course of the experiment. Also the position of the syringe piston determined flow quality as the contact between the piston and the barrel was not uniform. Measures were taken in order to ensure the syringe was cleaned and flushed after each use. Otherwise, the piston would develop burrs and loose performance.

3.4 Final generation microdevice: SCM

This final generation was the development of the single cell microbioreactor (SCM) for investigating gene expression under continuous or periodic nutrient conditions. Exploiting advantages in each generation we developed the two phase channel geometry in order to switch nutrient conditions while maintaining trap stability. Using this approach we were able to induce plasmids for fluorescent protein expression. We captured the fluorescence signal using an EMCCD (Andor iXon) in conjunction with our CCD for continuous phase contrast tracking.

Nutrient conditions could be exchanged by varying the flow rates between each inlet stream so that one stream would completely encompass the cross-slot region. We implemented this fluid exchange by creating custom LabVIEW code that would alternate the flow rates based on a square wave or sine function. In addition, flow conditions could also be binary with only an off or on state.

One of the major disadvantages was incorporating image processing with phase contrast over the previous generations. Sophisticated image processing steps could be added such as Fourier transform and edge detection to eliminate any background contributions due to PDMS producing phase artifacts. However, the more complex the inline image processing became the more the frequency response

of the trapped suffered. There was a fine balance between required frequency response and image analysis. To circumvent this I extended the microfabrication steps to include an increase channel height at the cross-slot region. This created a clean background for improved particle tracking. We chose to only increase the channel height at the cross slot by design. This was because we had already established working parameters for the 70 μm thick elastomeric membrane for a 30 μm channel height.

3.4.1 Two phase channel geometry

Fig. 3.6 illustrates our design for the SCM. This design was influenced by our previous generations as well as our development of an alternative trapping technique within the Schroeder group. This alternative technique was based on incorporating the Wheatstone bridge in a microfluidic system. Using this approach, plugs or sampling could be performed on continuous flow of sample mixture(10). I adapted this geometry for single cell trapping.

Introducing cell samples proved challenging as placement of the sample inlet would cause asymmetry of the flow profile at the cross − slot in the compressional axis. However, after a few iterations the sample inlet was placed at one of the elbows on the initial flow phase region of the SCM chip. Due to this asymmetry of the channel geometry the trapped cell was offset from the center of the compression axis. Essentially the extensional axis was translated from the center of the cross − slot. After switching to the alternate fluid phase we found that the cell would translated ˜ $15 - 20$ μm to center position. This provided us with a clear indication when the cell was exposed to the alternate nutrient condition.

3.4.2 Nutrient switching

For studying gene expression within the SCM we switched between bacteria culture media Lysogeny Broth (LB) and M9 minimal media with or without 1 mM concentration of Isopropyl β-D-1-thiogalactopyranoside (IPTG). This molecule is a lactose mimic that is routinely used for inducing protein expression systems with the *Lac* operator. It has also been the method of choice in single molecule stochastic protein expression studies within a single cell (11–13). The advantages of using this molecule over lactose is that it does not metabolize within the cell. Therefore, for batch protein expression this molecule can produce high yields at low concentrations. For single molecule studies this simplifies rate reaction studies. Recently, this expression system has been incorporated in a whole cell model (14, 15).

By incorporating waveforms for controlling the fluid exchange we could induce periodically from 30s to 2 min dwell times. We chose this time range for our proof principle demonstration of gene expression within the hydrodynamic trap. To best of our knowledge this is the first demonstration of gene expression in free solution with continuous fluid flow without requiring external force fields. Fig. 3.7 illustrates this fluidic exchange of TAMRA dye while trapping a fluorescent polystyrene bead.

3.4.3 Non-homogeneous channel height

In order to incorporate a raised or increased channel height at the cross – slot, I used a double patterning step in the microfabrication process. I patterned and developed my fluidic layer on a silicon wafer using negative photoresist as previously done then patterned again using a more viscous negative photoresist. Since my fabrication was limited by using my eyes only for aligning the pattern I

chose a 1 mm diamond to rest on the cross − slot. The cross slot has an expanded region in the xy plane as well as an increase height in the z dimensions. Extending the PDMS / solution interface away from the stagnation point position in the z direction provides a more homogeneous background noise (Fig. 3.8). Using the same flow rate conditions as the uniform cross-slot geometry the mean fluid velocity decreases due to the expansion of the cross-sectional area as seen in the relation:

$$Q = \vec{v} \cdot \vec{A} \tag{3.4}$$

where Q is the volumetric flow rate, $\vec{v}$ is the flow velocity and $\vec{A}$ is the vector cross-sectional area or surface of the channel. In addition the streamlines change in the yz plane. Both of these differences can be visualized by the contour map of the velocity using computational fluid dynamic (CFD) modelling (COMSOL Multiphysics 4.2) (Fig. 3.8).

3.4.4 Improved temperature control

During our initial implementation of temperature control we realized that the thin film heaters fluctuated in the z dimension when actuated. During the course of the experiment these deviations would add to the fluctuation of the cell in the z dimension when trapped. Therefore, we explored mounting procedures to minimize this imposed fluctuation in the z direction. However, mounting procedures would retain through their integrity over the course of the experiment. We then put our focus on developing an alternative temperature regulation method. Using a temperature regulated water bath for circulating water, we designed a thermal plate that could be mounted on the microscope stage. This thermal plate was designed to add or exchange thermal plate insets for better heating coverage depending on the device geometry. For phase contrast imaging at 40x (Olympus)

this was not problem since we were not dealing with an oil immersion objective and our working distance of our objective was ~2mm.

3.4.5 Gain schedule control model

As discussed in the Chapter 2, a more adaptive controller was implemented for the final generation. This controller provided a gentle mechanism of controlling the rate of translation of the cell to the stagnation point. This reduced oscillations along the extensional axis as compared to the simple proportional control model. .We used an XNOR relation for determining particle position and direction of motion in deciding the appropriate feedback response (Section 2.6).

3.5 Characterization of the SCM

Appropriately constructing the valve membrane thickness and corresponding relation between stagnation position and applied pressure provides a linear restoring force of the form $P = -K_c\,(y - y_o)$ where y_o is a desired set point along the extensional axis. When the gain K_c is appropriately tuned a ~1 μm particle can be confined to within a 1 μm displacement at 30 fps imaging acquisition. This level of confinement can be visualize in trajectory of a trapped target particle (Fig 3.9). The power spectrum can be plotted to determine the corner frequency (f_c) of the trapped target particle (Fig. 3.9). The relation between this frequency and the trap stiffness k is provided by the relation:

$$k = 2\pi\gamma f_c \tag{3.5}$$

where the viscous drag coefficient is defined as $\gamma = 6\pi\eta r$. From this the force of the trap can be calculated using the Hookian spring model $F = kx$. We

experimentally observed trap stiffness on the order of $k = 1.9 \times 10^{-4}$ pN/nm and compares well to the theoretical calculation using:

$$k = 6\pi\eta R\dot{\varepsilon} \tag{3.6}$$

where η is the viscosity, R is the radius of the particle, and $\dot{\varepsilon}$ is the strain rate. Using water at a viscosity of 11 cP and a strain rate of ~1 s^{-1} we calculate a trap stiffness to be $k = 2 \times 10^{-4}$ pN/nm for a 2.2 μm diameter bead.

3.6 Trapping single cells

Trapping single cells within the hydrodynamic trap required all the advances previously mentioned including threshold image analysis which eroded and diluted the cell silhouette for better tracking. We were able to trap single cells such as *Oscillospira guilliermondii, Escherichia coli,* Osteoblasts, and red blood cells. The hydrodynamic trap aligns the long axis of the cell with the extensional axis for non-spherical cell morphologies. Since the bulk of my research was aimed at *O. guilliermondii* and *E. coli* confinement, I will focus my discussion on these two cell types. During the sorting of *O. guilliermondii,* trapping of spirochaetes and large protozoa were possible by adjusting image process and gain parameters. During *E. coli* experiments we observed run and tumble events similar to observations by Min et al. (16) in an optical trap. In plotting the power spectrum we were also able to observe both the peaks for the body and flagellum rotation. However, our methods of targeting cell position capture were not as robust as back focal plane interferometry since we relied on image process for determining the centroid position. This produced a bias in our data set as fluctuations in particle position were intrinsic to camera acquisition noise. Appendix 3.7 contains details on cell sample preparation.

3.6.1 *Oscillospira guilliermondii*

The *Oscillospira spp.* are found consistently in the rumen contents of cattle and sheep. These large morphological distinct bacterium are a part of the gut ecosystem. It has been postulated that presence of certain phenotypes or morphologies are dependent on diet (17). Rumen samples of Norwegian reindeer stored in EtOH were provided by Prof. Roderick Mackie at the University of Illinois. The samples contained large vegetative debris that would clog the microfluidic channels. We used filter paper (Whatman) to remove any debris over ~25 μm since our channel height was 30 μm. Our target morphology for cell sorting was that of *O. guilliermondii* with distinct $5-10$ μm length rod shape and septation lines running orthogonal to the long axis of the cell. Additionally, this morphology forms a round central spore which is depicted in Fig. 3.10. This unique morphology is a model candidate for targeting and tracking by eye. The controller also has the potential of automating this selection with current LabVIEW image operations from the IMAQ module to target this distinct morphology.

3.6.2 *Escherichia coli*

For growth analysis experiments, we used *E. coli* strains MG1655 and BLR(DE3). Overnight cell cultures were grown in LB (Lysogeny Broth) medium + 100 μg/mL ampicillin inoculated from a single colony on an LB agar plate. Following overnight culture in an incubated shaker at 37 ^{o}C, the starter culture was diluted 1:100 in fresh LB medium + ampicillin. The serially diluted sample was then cultured for 3 hr on an incubated shaker at 37 ^{o}C. Next, the cell samples are introduced into the microfluidic device to monitor cell growth during trapping in free solution at a constant flow rate.

For real-time gene expression experiments, standard PCR and ligation techniques were used to clone a gene encoding for a variant of the yellow fluorescent protein (Venus) downstream of two lac operators on a strong T5 promoter (Qiagen, pQE80L plasmid). Cloning was performed using BLR(DE3) competent cells (a derivative of BL21), which improves exogenous plasmid yields. Cells were transformed with plasmid vectors using heat shock methods. For preparing cells for on-chip experiments, the BLR strain was cultured using identical methods used for growth experiments, except the cells from overnight cultures were diluted 1:100 in M9 minimal media with 0.5% v/v glycerol + ampicillin. The media used for inducing gene expression contained 1 mM IPTG and was otherwise identical to the dilution media (M9 minimal media with 0.5% v/v glycerol + ampicillin).

Intracellular dynamic experiments were performed with *E. coli* strain MG1655 –*lac* with a chromosomal Tet operator binding array located at the atpI locus. Initially, cells are grown in rich media containing a glycerol carbon source (EZ Rich Defined Medium (RDM) + 0.5% glycerol v/v), conditions under which Tet repressor proteins are localized along the binding array. During these experiments the cell environmental conditions in the SCM are switched to media containing 200 ng/mL anhydrotetracycline (aTc). The presence of aTc induces the unbinding of TetR from the tandem array, followed by intracellular diffusion of TetR-Venus proteins. Using the SCM, we are able to observe the rapid release and subsequent intracellular diffusion of the Tet repressor within the nucleoid region of Gram-negative bacteria.

3.7 Experimental details

Below we provide the details governing the experimental design, development and implementation of the SCM for single cell analysis.

3.7.1 Fabrication of the SCM

We use standard soft-lithography protocols for fabricating the SCM using SU-8 negative photoresist. For this device, the fluidic layer is spin coated twice to incorporate a raised region ('ceiling') at the cross-slot. See Appendix A and B for the fabrication protocol and mask design.

3.7.2 Microscope setup and PC integration

Using an inverted Olympus microscope (IX-71), we mounted and Andor iXon+ EMCCD camera to the trinoc port. Using a tube C-mount adapter, we attached an AVT Stingray CCD camera to the eyepiece of the trinoc port. This allowed for simultaneous phase-contrast and fluorescence acquisition through the trinoc light path. An adjustable tube C-mount adapter was attached to the EMCCD to match the focal length of the CCD. We then incorporated two Uniblitz shutters to alternate between phase-contrast acquisition and fluorescence acquisition. Two syringe pumps (Cole Parmer and Harvard Apparatus PHD 2000) were used to switch between nutrient streams. Two pressure transducers (Proportion Air) were incorporated and using luer lock adapters we added PTFE tubing 24 Gauge with 24 Gauge metal connectors. This tubing was filled with ddH_2O and connected to the SCM device chip valves. Pressure of 10 psi was added to force ddH_2O into the valve, thereby removing the trapped air. This allowed for continuous use of the SCM without air accumulation in the fluidic channels. Once the media was pumped into the device, all outlets were blocked and fluid was forced at a rate 1000 μL hr^{-1} until the trapped air was compressed. After stopping the pumps, if the trapped air expanded in size, then a leak could be present in the device. Once the device was pressurized, the remaining air should continue to dissolve into the

PDMS if no leaks are present. Finally, the device is ready for cell sample and media. See Fig. 3.11 for the setup and depiction of the overall experimental setup.

All components except the temperature regulation were controlled via PC integration. Both pressure transducers (Proportion Air) were control by a BNC cable box (NI 2110) connected to a PCI card (NI 6229). Both syringe pumps were connected by RS232 VISA with USB PC adapter and integrated with LabVIEW using the appropriate SDK supplied by the manufacturer. EMCCD (Andor iXon) and CCD (AVT Stingray) were connected by the manufacture supplied PCI cards and integrated into custom LabVIEW code using Andor SDK and IMAQ Vision Acquisition Module, respectively.

3.7.3 Automation: Feedback controller interface

Automated particle trapping is achieved using either a linear feedback or adaptive gain schedule control algorithm implemented using a custom LabVIEW code. The LabVIEW code captures images from a CCD camera and transmits an electric potential (voltage) to a pressure regulator, which actively modulates the position (partially open/closed state) of an on-chip dynamic pneumatic valve. As the valve position changes, the hydrodynamic flow rate in one outlet line is adjusted, thereby re-positioning the stagnation point and enabling hydrodynamic trapping. The steps in the feedback loop are sequentially and iteratively executed at the rate of image capturing (10-60 Hz). The LabVIEW code executes the following steps during each feedback loop cycle:

Image capture. An image is acquired for a "target" particle in the trapping region of the microfluidic device using fluorescence microscopy with a 10x objective lens (NA: 0.4) and a CCD camera.

Particle tracking. Particle centroid position is determined, and the particle tracking algorithm is initiated. Particles are localized by fitting the emission

intensity profile of the particle to a Gaussian peak fit, from which the centroid position is determined.

Flow field control. The updated pressure intended for the on-chip dynamic valve is calculated using a feedback control algorithm with a proportional controller. In this way, the action of the valve is to re-position the stagnation point, which exerts a hydrodynamic force on the particle in order to steer the particle toward the trap center.

The LabVIEW code records the following data for every image captured during particle trapping: 1) time elapsed, 2) centroid (x,y) position of the trapped particle, 3) position of the trap center, 4) distance of the particle from the trap center, 5) pressure applied to the on-chip valve. In addition, the code also records a movie of the trapped particle in AVI file format.

The steps for initiating hydrodynamic trapping using our interface is outlined here.

1. Run the custom-built LabVIEW code, which automates particle trapping.
2. Using the microscope x-y translation stage, position the trapping region (cross-slot) at the center of the camera view. Bring the trapping region into focus of the objective lens and adjust the camera settings to optimize imaging conditions.
3. Choose a rectangular region of interest (ROI) within the camera's field of view such that the center of the ROI will be the position of the trap center.
4. Initialize the offset pressure applied to the on-chip valve. In one of the outlet channels, a 100-200 μm wide constriction is introduced to provide an offset pressure for the on-chip valve. The constant off-set pressure enables the on-chip valve to adjust the stagnation point position in the

vicinity of the center of the channel cross-slot. For most experiments, the offset pressure is set between 0-12 psi depending on the channel dimensions (height and width), the constriction width, and the specifications of the on-chip valve (valve size, membrane thickness, etc.).

5. Initiate the feedback controller and adjust the proportional gain to optimize trap response. The feedback controller will adjust the pressure applied to the on-chip valve in order to move the stagnation point position, which minimizes the error or the distance between the particle position and the set point (trap center). Depending on the flow rate and the on-chip valve position, there is an optimal proportional gain value, which increases trap stability and eliminates unwanted particle oscillations or "ringing".
6. Trap a particle. The LabVIEW code will automatically trap one of the particles entering the trapping region. Once a desired particle is trapped, it is possible to shut off the sample flow and isolate the trapped particle in buffer solution, if desired.
7. Monitor the trapped particle and maintain particle focus within the image plane using manual focus or an automated focus microscope setup. It may be necessary to slightly adjust the proportional gain of the feedback controller in order to ensure trap stability during the course of a long time-scale trapping event (minutes to hours).

3.7.4 Cell strains and culture media

The details on culture media and cell strains used are provided in Tables 3.1 and 3.2.

3.8 Figures and tables

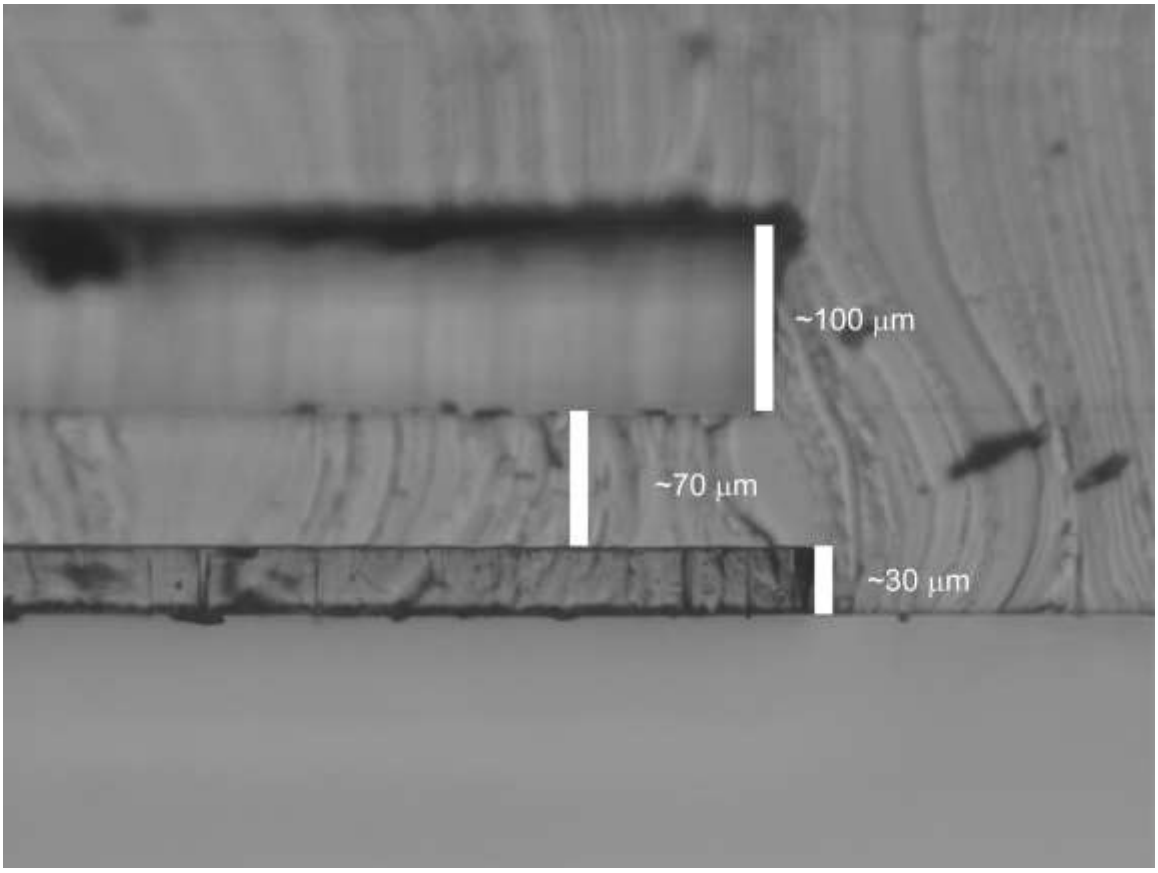

Figure 3.1: PDMS slab cross-section of SCM. From bottom to top you see the fluidic layer, valve membrane, and pressure valve. To make these layers apparent it is ideal to chop down with a razor blade than slicing with a scalpel. The striation patterns is the tool markings from chopping down.

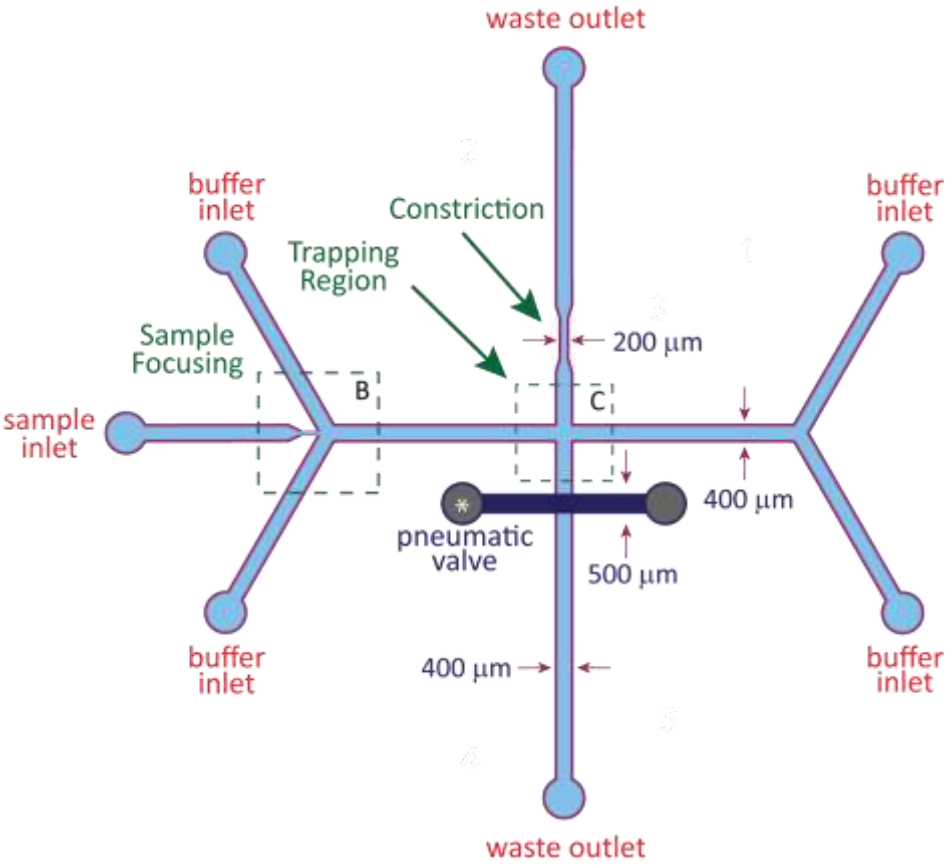

Figure 3.2: First generation of the hydrodynamic trap. There is sample focusing, constriction offset pressure, and a pneumatic valve for controlling the stagnation point position. A four way junction off-chip separates one syringe line into four inlets.

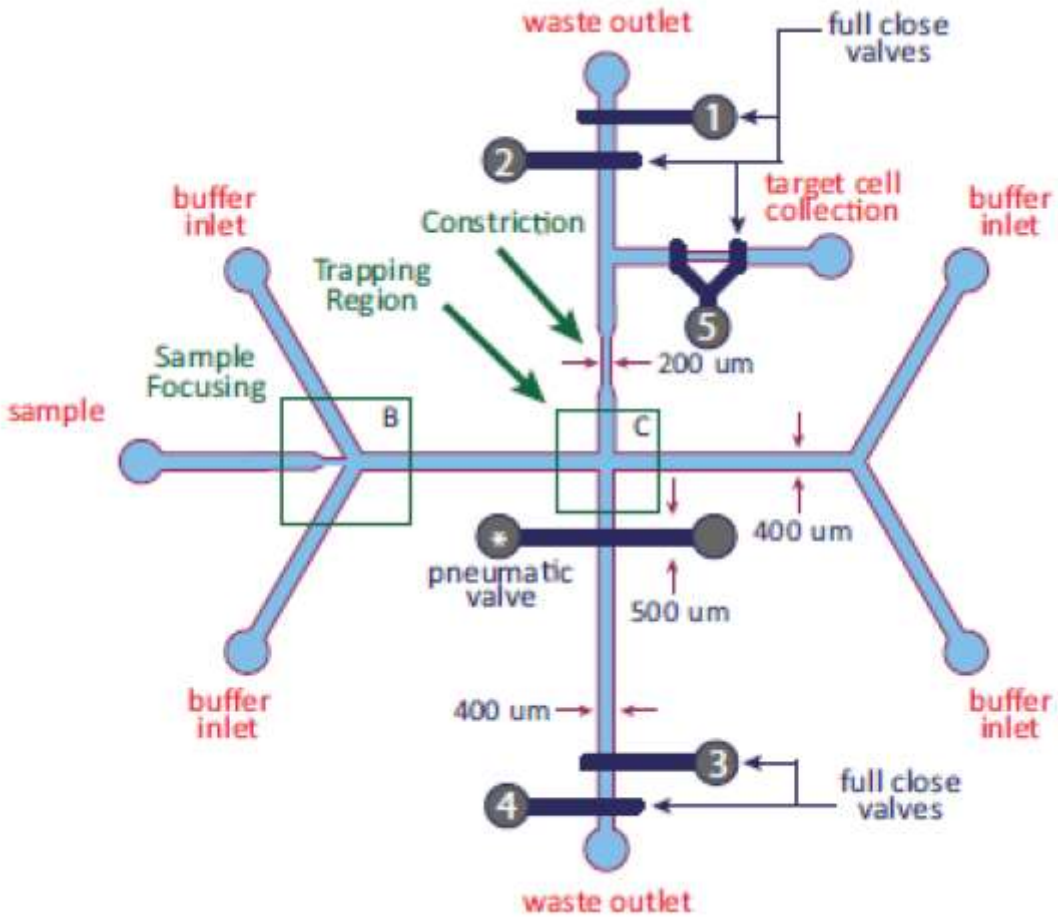

Figure 3.3: Second generation hydrodynamic trap for cell sorting. During the rinse step the trapped cell can be further analysed to confirm the target cell morphology. After the rinse, valves 1, 2, 3, and 4 are closed and valve 5 is opened. This guides the target cell to the collection outlet. After collection, valves are switched back to their initial state and sample flow is turned on for another sorting cycle. Channel dimensions were 400 x 30 μm.

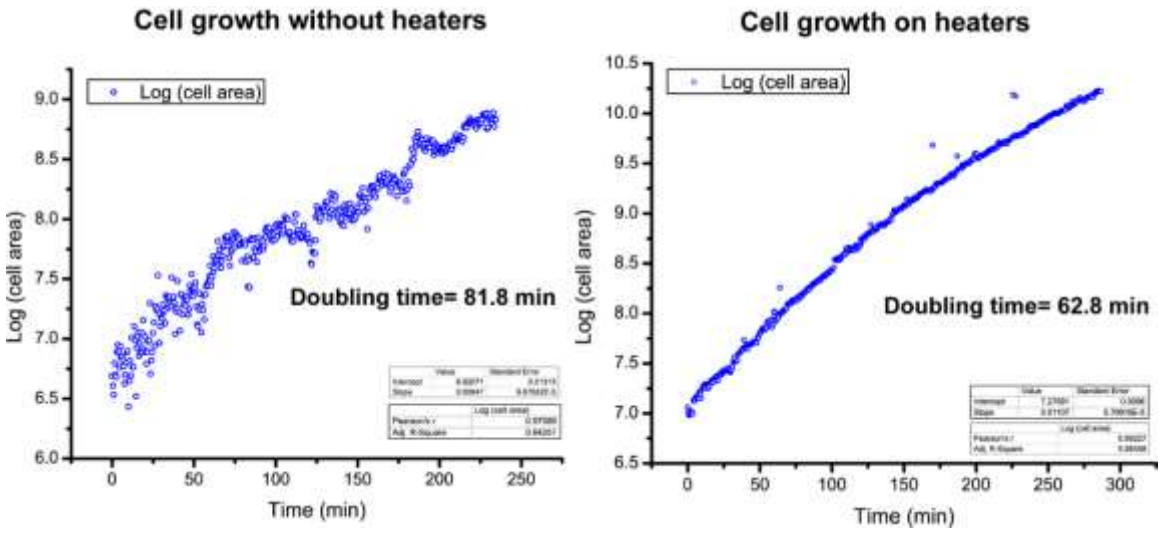

Figure 3.4: Temperature calibration for thin film heaters. Cells were plated in the microdevice and total cell area was recorded over time. When heat was off cell growth was not consistent as compared to cells grown on a well temperature regulated surface. *E. coli* strain BLR(DE3) in M9 minimal media.

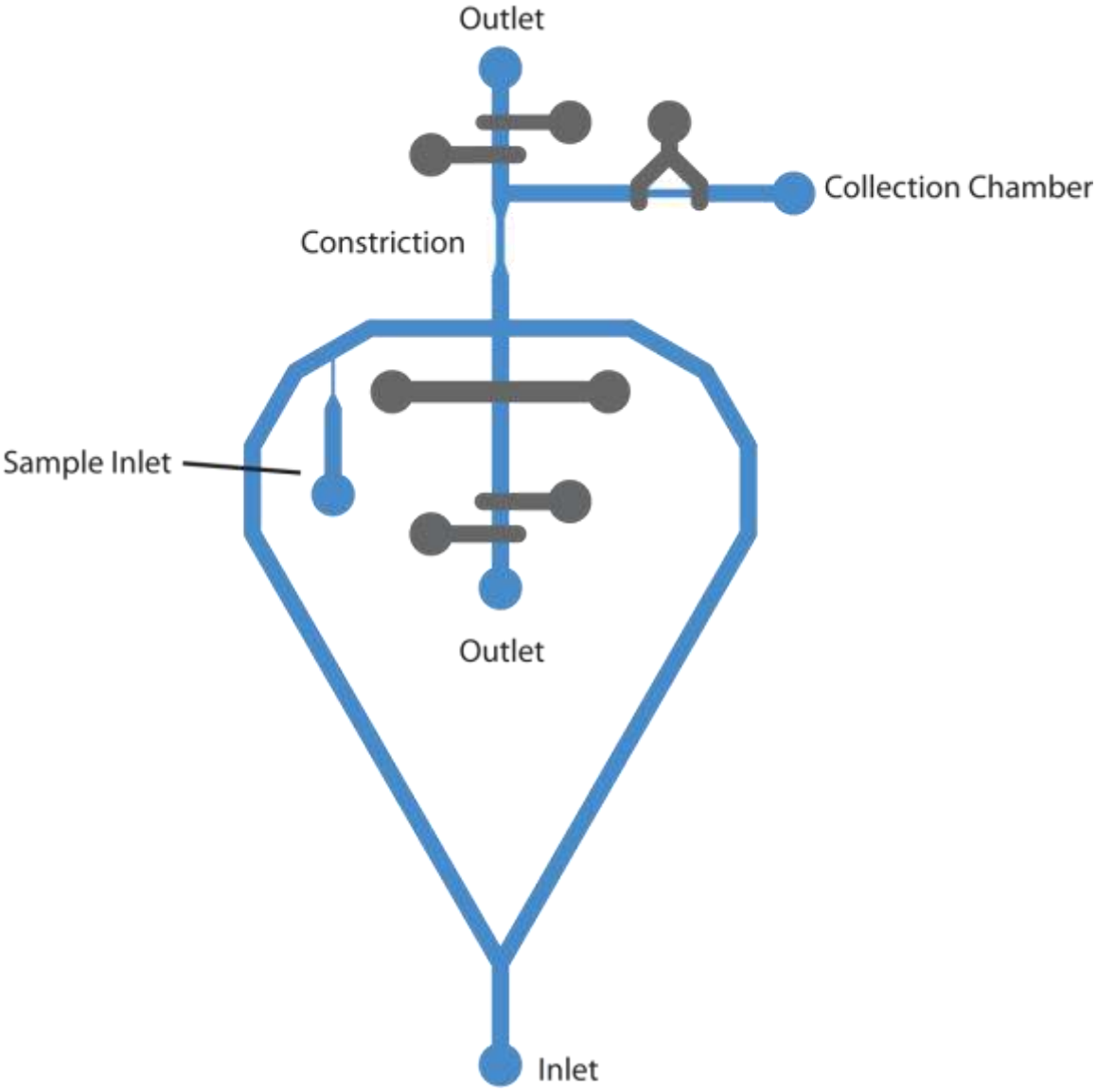

Figure 3.5: Third generation microdevice for cell growth. Fluid flow was combined to one inlet for improved trap stability over extended time scales. Channel dimensions are 400 x 30 m.

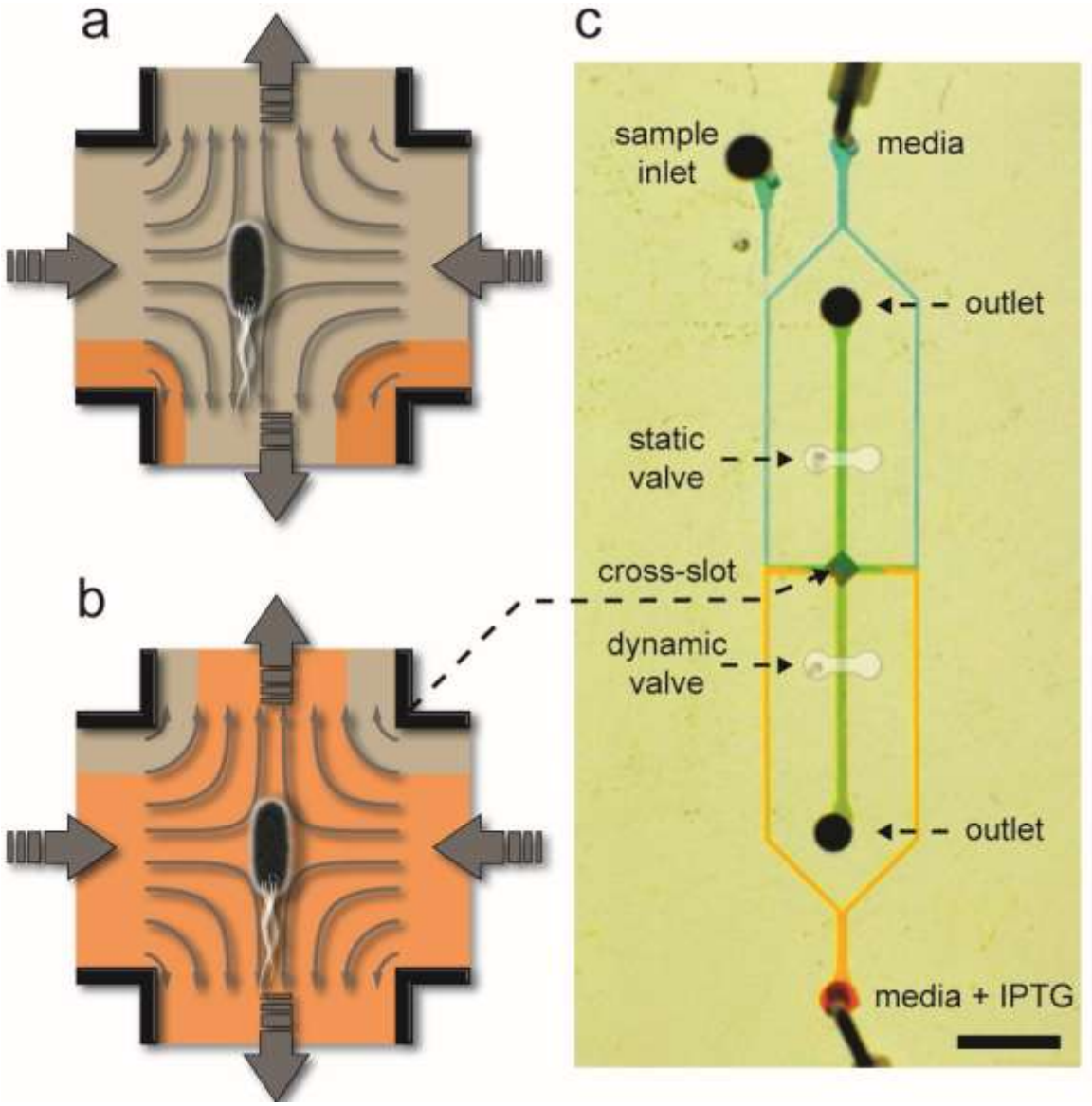

Figure 3.6: Microfluidic device and schematic of trapping mechanism in the SCM. (a,b) Schematics of cell confinement in cross-slot region (not to scale), and the transitioning of growth environments from Medium A to Medium B. (a) A single cell is initially grown in Medium A (tan color), followed by (b) rapid switching of the cell environment to Medium B (orange color) while confining the cell in free solution. (c) Optical micrograph of the SCM. Scale bar: 3 mm.

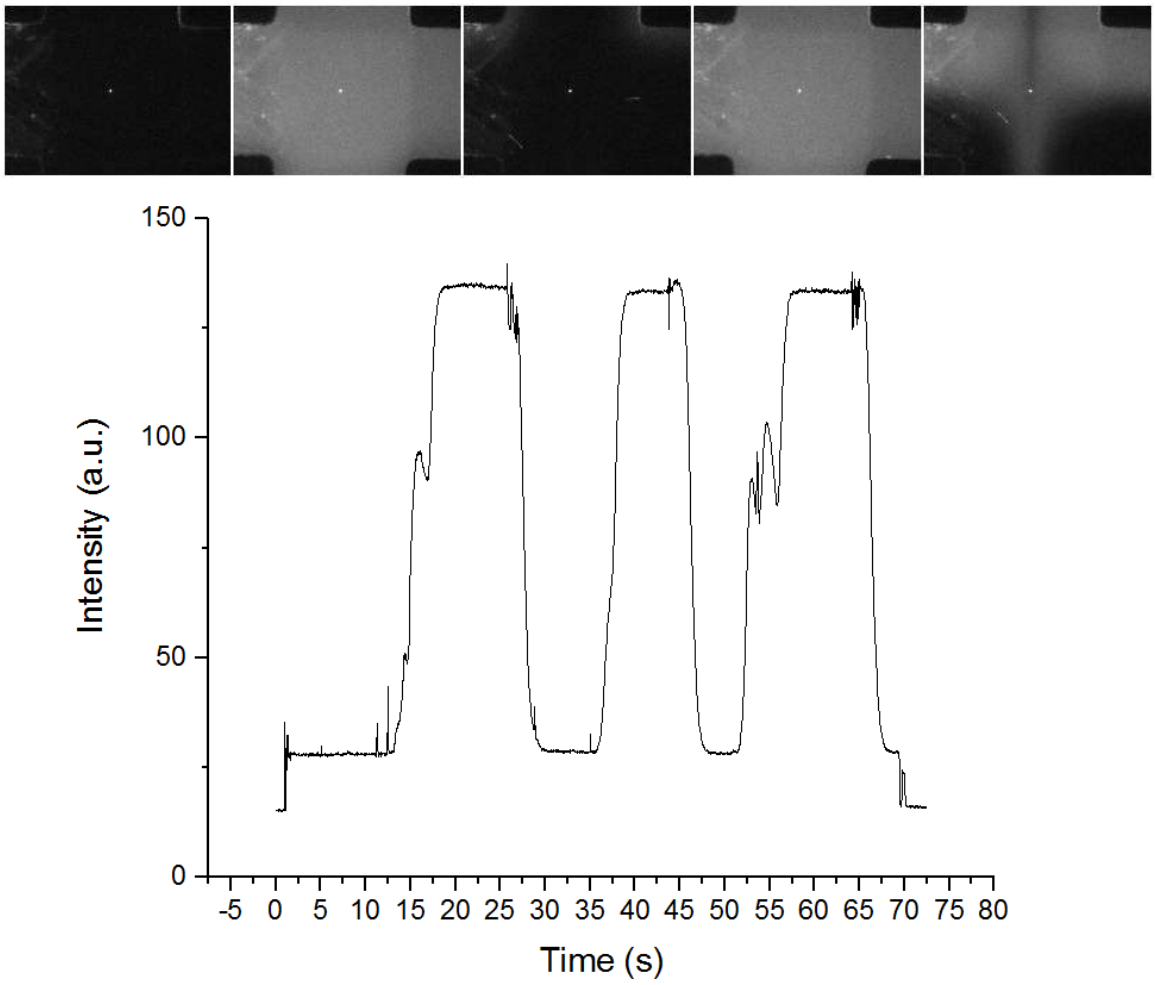

Figure 3.7: Intensity profile of flow switching in SCM. Top panel shows TAMRA dye being switch off and on while maintaining particle trap stability. Graph show intensity profile along y-axis at x = 0 (i.e. at the stagnation point).

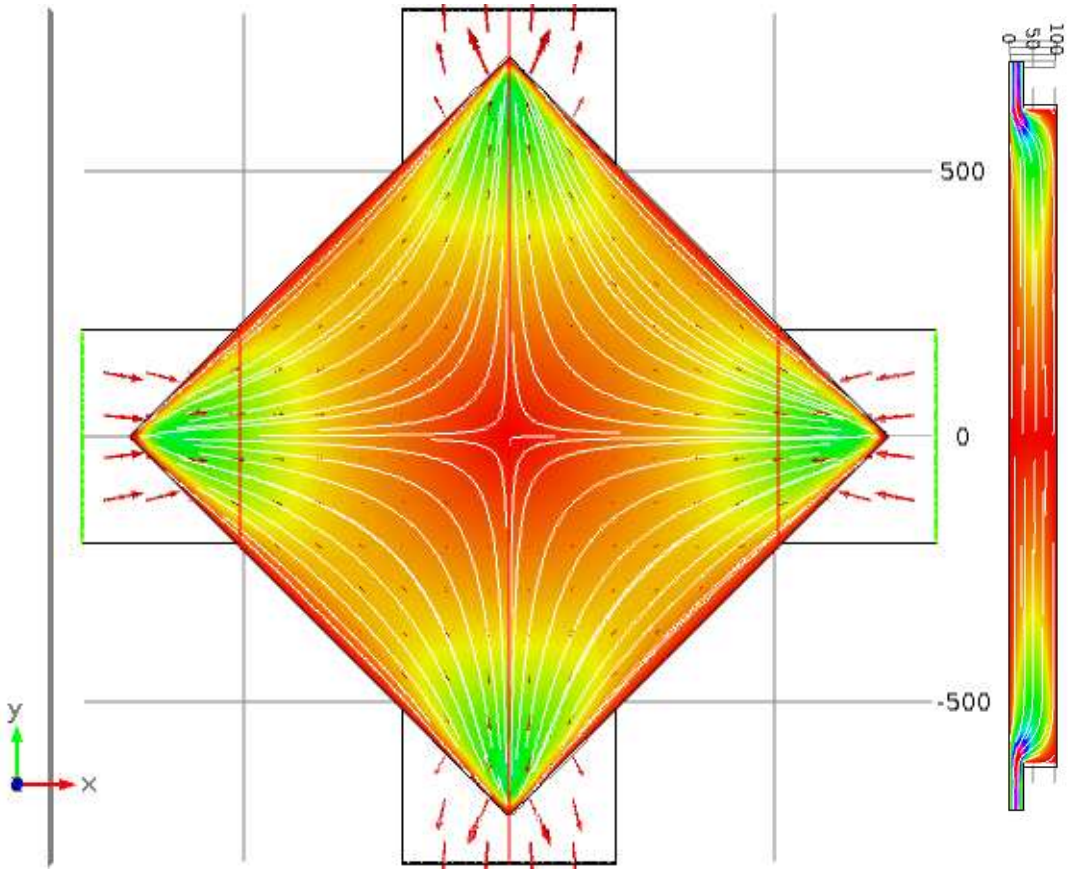

Figure 3.8: Computational fluid dynamics (CFD) of SCM cross-slot with diamond. On the right is yz cross-section along y-axis at x = 0. Channels are 400 x 30 μm and diamond is 1 mm with a height of a 100 μm. Solution acquired using water at room temperature with creeping flow (Q = 100 μl hr^{-1}).

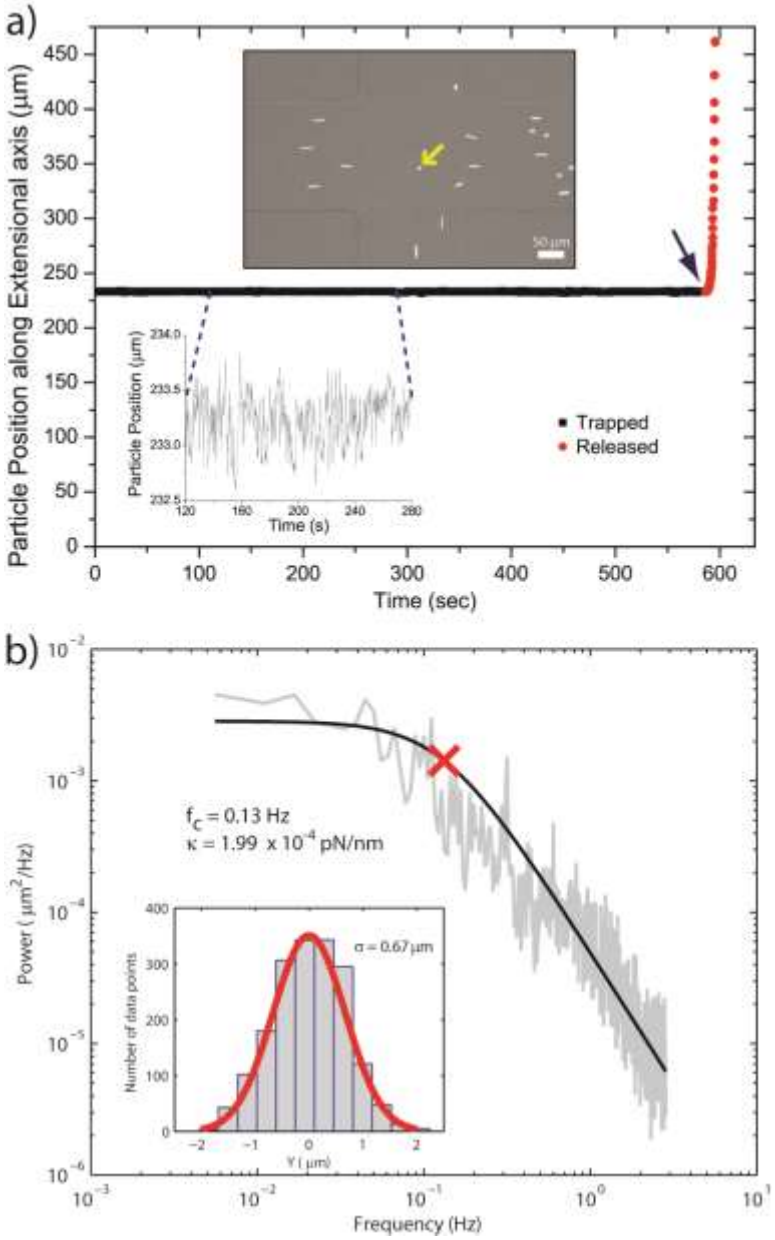

Figure 3.9: (a) Trajectory for a trapped particle along the extensional axis (squares). When the particle is released from the trap (arrow), it escapes along one of the outlet channels (circles). Insets: (Bottom) Rescaled particle trajectory between 120–280 s. (Top) Micrograph of a bead trapped at the stagnation point. (b) Power spectrum of a trapped polystyrene bead (2.2 μm diameter) along the extensional axis. Inset: Histogram of displacements of a trapped bead (2.2 μm diameter) from the trap center. Reprinted with permission from (18).

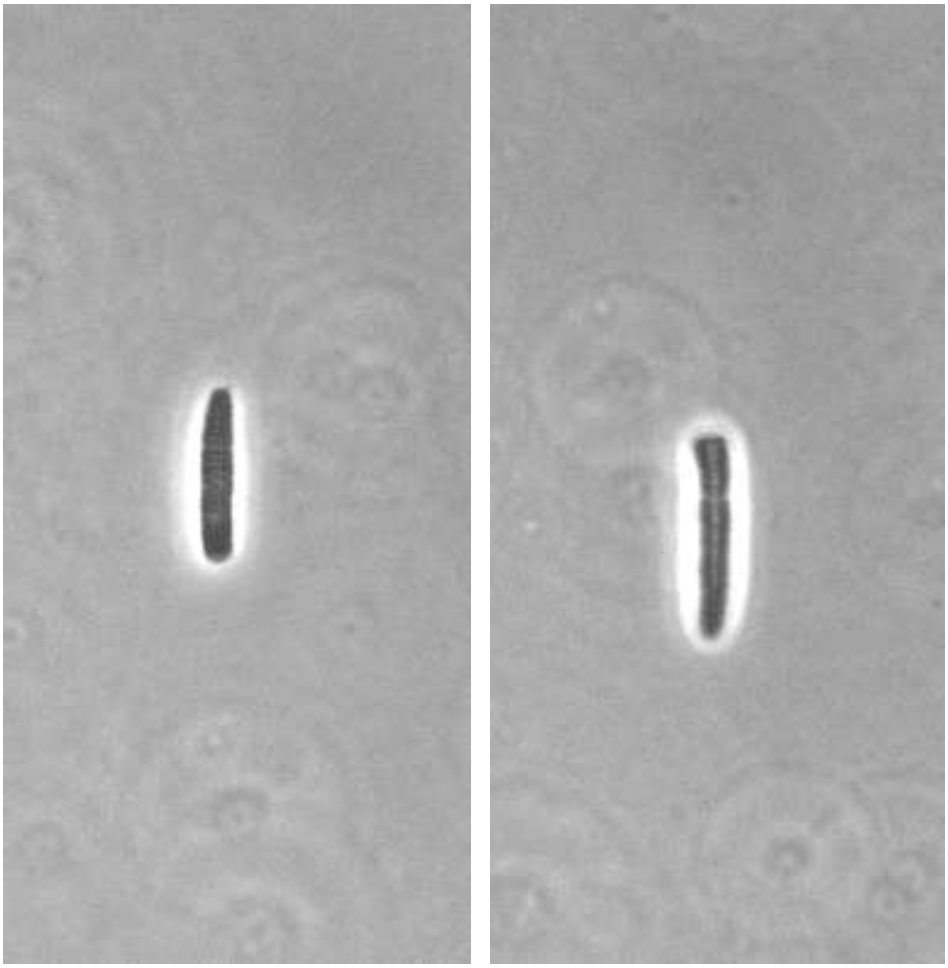

Figure 3.10: *Oscillospira guilliermondii* in the hydrodynamic trap. This cell has a distinct morphological shape that is ideal for user selection and screening from a heterogeneous cell sample.

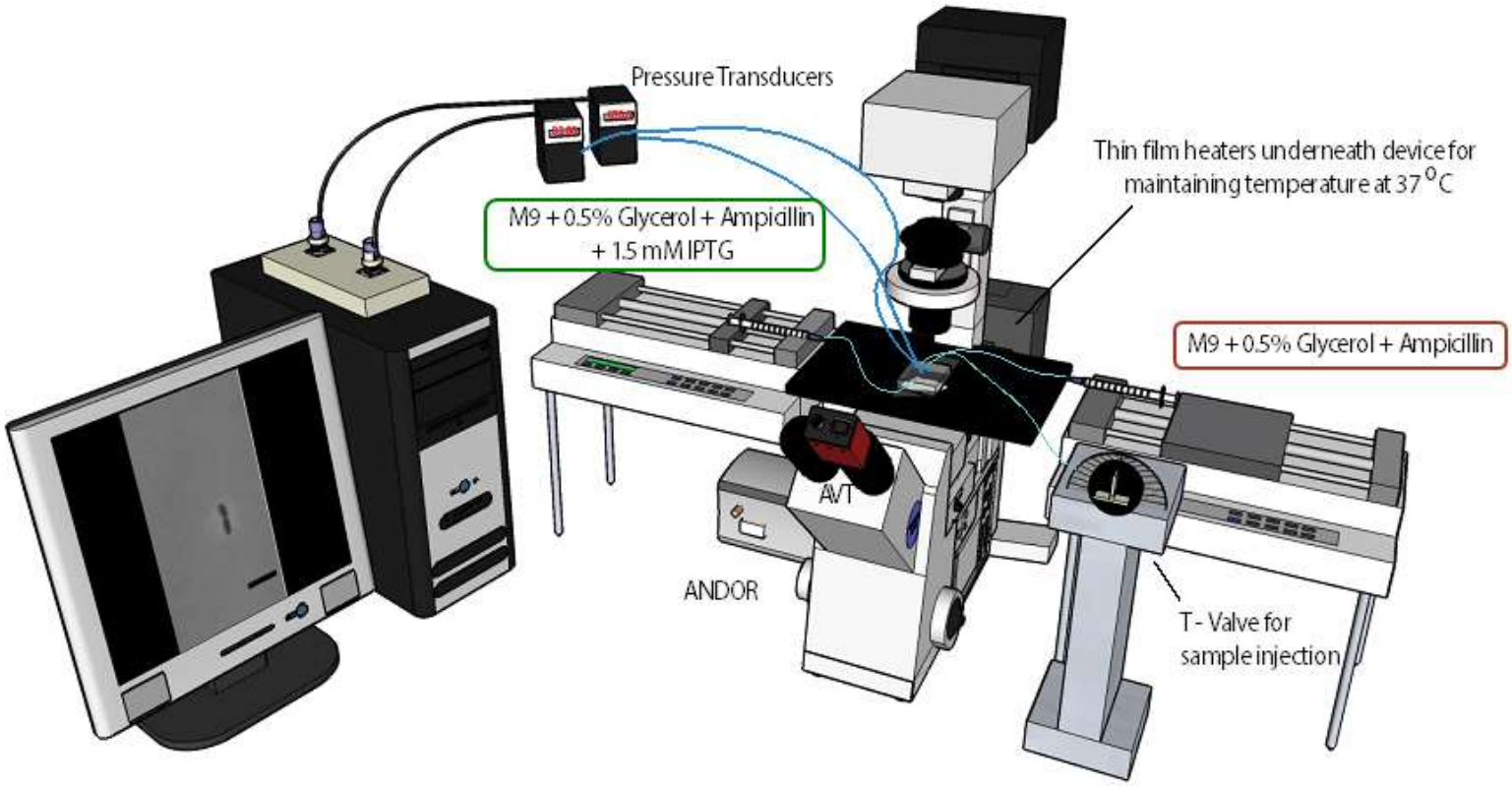

Figure 3.11: Experimental setup of the SCM. The setup consists of two sets of syringe pumps and pressure transducers. Phase contrast imaging is capture by the CCD camera, while fluorescence intensity is captured by the EMCCD. All components are interfaced with the PC except for temperature control.

Medium	Components (per L)
Lysogeny Broth (LB)	– 10 g tryptone – 5 g yeast extract – 10 g NaCl
M9 minimal media	– 200 mL 5X M9 salts ▪ Na_2HPO_4 ▪ KH_2PO_4 ▪ NaCl ▪ NH_4Cl – 2 mL 1 M $MgSO_4$ – 100 µL 1 M $CaCl_2$ – 10 mL 50% glycerol – 1 mL thiamine hydrochloride – 50 mL 10% casamino acids – H_2O to 1 L
EZ Rich Defined Medium (RDM)(Teknova)	– 10 mL 0.132 M K2HP04 – 100 mL 10X ACGU – 200 mL 5X Supplement EZ – 10 mL 50% v/v glycerol – Sterile H_20 to 1 L

Table 3.1: Growth culture medium components. Ampicillin (100 µg mL^{-1}) was added to the respective medium for ampicillin resistant *E. coli* strains. Where indicated, 1 mM IPTG or 200 ng ml^{-1} aTc was added to the media.

Strain	Plasmid	Antibiotic Resistance
MG1655	None	None
BLR (DE3) competent cells	pQE80L with Venus	Amp
MG1655 –lac atpI<tetO>	pBH74 expressing TetR +Venus using 0.2% arabinose	Amp

Table 3.2: Constructs used for the live single cell analysis. The construct with $< tet0 >$ chromosomal binding array at the atpI locus was provided by Prof. Tom Kuhlman. *Oscillospira spp.* samples (not shown) were provided by Prof. Roderick Mackie.

3.9 References

1. Unger, M.A., H.P. Chou, T. Thorsen, A. Scherer, and S.R. Quake. 2000. Monolithic microfabricated valves and pumps by multilayer soft lithography. Science. 288: 113–6.

2. Yildiz, A., and P.R. Selvin. 2005. Fluorescence imaging with one nanometer accuracy: application to molecular motors. Acc. Chem. Res. 38: 574–582.

3. Zink, D., N. Sadoni, and E. Stelzer. 2003. Visualizing chromatin and chromosomes in living cells. Methods. 29: 42–50.

4. Tian, F., E.M. Johnson, M. Zamarripa, S. Sansone, and L. Brancaleon. 2007. Binding of porphyrins to tubulin heterodimers. Biomacromolecules. 8: 3767–3778.

5. Valdez, R., E. M Johnson, J. A Belcher, J. F Fuini, L. Brancaleon, et al. 2009. Porphyrins affect the self-assembly of tubulin in solution. Biophys. Chem. 145: 98–104.

6. Tuchin, V. V, A. Tárnok, and V.P. Zharov. 2011. In vivo flow cytometry: a horizon of opportunities. Cytometry. A. 79: 737–45.

7. Akerlund, T., K. Nordström, and R. Bernander. 1995. Analysis of cell size and DNA content in exponentially growing and stationary-phase batch cultures of Escherichia coli. J. Bacteriol. 177: 6791–7.

8. English, B.P., V. Hauryliuk, A. Sanamrad, S. Tankov, N.H. Dekker, et al. 2011. Single-molecule investigations of the stringent response machinery in living bacterial cells. Proc. Natl. Acad. Sci. U. S. A. 108: E365–73.

9. Cormack, B.P., R.H. Valdivia, and S. Falkow. 1996. FACS-optimized mutants of the green fluorescent protein (GFP). Gene. 173: 33–8.

10. Tanyeri, M., M. Ranka, N. Sittipolkul, and C.M. Schroeder. 2011. Microfluidic Wheatstone bridge for rapid sample analysis. Lab Chip. 11: 4181–6.

11. Elf, J., G.-W. Li, and X.S. Xie. 2007. Probing transcription factor dynamics at the single-molecule level in a living cell. Science. 316: 1191–4.

12. Yu, J., J. Xiao, X. Ren, K. Lao, and X.S. Xie. 2006. Probing gene expression in live cells, one protein molecule at a time. Science. 311: 1600–3.

13. Cai, L., N. Friedman, and X.S. Xie. 2006. Stochastic protein expression in individual cells at the single molecule level. Nature. 440: 358–62.

14. Roberts, E., A. Magis, J.O. Ortiz, W. Baumeister, and Z. Luthey-Schulten. 2011. Noise contributions in an inducible genetic switch: a whole-cell simulation study. PLoS Comput. Biol. 7: e1002010.

15. Assaf, M., E. Roberts, and Z. Luthey-Schulten. 2011. Determining the stability of genetic switches: explicitly accounting for mRNA noise. Phys. Rev. Lett. 106: 4.

16. Min, T.L., P.J. Mears, L.M. Chubiz, C. V Rao, I. Golding, et al. 2009. High-resolution, long-term characterization of bacterial motility using optical tweezers. Nat. Methods. 6: 831–5.

17. Roderick, S.L. 2005. The lac operon galactoside acetyltransferase. C. R. Biol. 328: 568–75.

18. Tanyeri, M., E.M. Johnson-Chavarria, and C.M. Schroeder. 2010. Hydrodynamic trap for single particles and cells. Appl. Phys. Lett. 96: 224101.

Chapter 4

Applications of the SCM

In this chapter, I will discuss the results of three applications of the hydrodynamic technique and the final application of the SCM which encompasses all features for single cell analysis which include trapping, transition, and observing single cell trajectories. I provide an overview for each application followed by discussion on different aspects pertaining to each application.

4.1 Cell sorting of *O. guilliermondii*

The 2nd iteration (Fig. 3.3) of the hydrodynamic trap offers an excellent platform to isolate and sort single cells based on cell morphology from diverse biological samples. Our initiative for this project was to answer key biological questions by performing sequencing on uncultivated microorganisms with a distinct morphology. In Fig. 4.1 you see heterogeneous cell sample, which includes *Oscillospira spp.* extracted from the rumen of Norwegian reindeer (1). The hydrodynamic trap

enables isolation of morphologically distinct cells and rinses extraneous DNA away for pure collection.

4.1.1 Target selection in cell suspensions

The automated trapping algorithm provides the user with the ability to decide which target cell to confine. Selection is achieved by drawing a ROI with the center at the desired cell location and translating the ROI as the cell approaches the extensional axis. The rumen samples obtained were dense with gut fauna and flora. As described in Chapter 3, we took care to dilute the sample and removed large debris to prevent clogging of are microchannel. However, we believe that there was a trade-off between filter selection and abundance of *Oscillospira spp.* It is possible that in our filter procedure removing large vegetative debris that some *Oscillospira* was also lost in the process. The species *O. guilliermondii* at times seemed extremely difficult to observe. Without flow focusing larger cellular morphologies seemed to move toward the walls of the microchannel. Smaller cell morphologies tended to retain their position at the max velocity stream at the center of the laminar flow profile. There was a trade-off between increasing the flow focus and decreasing the response of the user input. Increasing the flow focus with our current geometry required higher flow rates. However, this puts a limit on the reaction time of the user to select the target cell for confinement.

Current flow cytometry methods dilute sample concentration and create a spatial-temporal distribution of cells in a single file stream (2). However, these methods provide high throughput screening and our designed for very high flow rates. Alternatively, methods using contract and expansion of the fluid profile could work in regard with this design. Flow focusing in the xy plane is achieved by placing square or elliptical regions staggered along a fluid channel. As the fluid reaches this region, the cross-section increases expanding the concentration of cells

in solution. This staggered repeating expansion and contraction reshapes the density profile to provide a steady narrow stream of cells (3, 4). However, to readily increase trap stability we increased the viscosity of our sample solution using 20% w/v glycerol ($\eta \approx 11$ cP). This provided an improved trapping experience for sorting this unique cell morphology.

4.1.2 Genomic analysis

For this genomic sequencing, we provided two samples of ≈10 cells and ≈50 cells of *O. guilliermondii* for whole-genome-amplification. The purity of 10 count sample was estimated ≈80% with some slight background noise resulting from bacterial contamination. However, this contamination was also present in the negative control for whole-genome-amplification.

The 10 *Oscillospira*-like cells were extracted using DNeasy blood and tissue kit (Qiagen). Given the low amount of genomic DNA, two consecutive rounds of whole genome amplification were conducted to prevent increasing the yield of genomic DNA. The first round is isothermal multiple displacement amplification by phi29 polymerase (Repli-G kit, Qiagen), followed by PCR-based amplification of DNA fragments ligated into library pairs at both 3'- and 5'-end of the fragmented genomic DNA (GenomePlex, Sigma Aldrich). A negative control, comprising of 300 µl of 1X PBS without cells, was subjected to the same experimental protocol as the 10 Oscillospira cells. The amplified genomic DNA (named as Osci-10) is shown in Fig. 4.2, with a fragmented size range of 300-1000bp. To ensure purity with both *Oscillospira* product and negative control, amplification of the V1-V3 hypervariable region of 16S rRNA was done using conserved 11F and 519R primers. This provided the correct bright band for Oscillospira sample at ≈500bp. However, there was also a lower band intensity at ≈500bp for the negative control. This

suggests that bacterial contamination is also present in the negative control. The contamination might possibly arise from remnant bacterial genomic DNA present in the DNA polymerase. Whole genomic amplification is extremely sensitive, and can amplify minute amount of DNA. However, we believed that since the signal intensity obtained from the Oscillospira sample is markedly higher than that from negative control, the background noise should be relatively low for subsequent sequencing efforts.

Using the amplified genomic DNA product of Oscillospira sample and negative control we amplified the Oscillospira specific 16s rRNA gene using Osci-67F and Osci-460R. The first row of the gel shows a band at ≈400bp from the Oscillospira sample and an incorrect band at ≈100bp for the negative control which possibly indicates primer dimer formation. The slightly lower signal intensity of Oscillospira-specific 16S rRNA gene amplicons as compared to the total bacteria may be due to the incomprehensive coverage of the Oscillospira-targeting primers Osci-67F and Osci-460R. The primers were designed from a limited number of Oscillospira sequences, and may not be able to fully amplify out all Oscillospira present in this sample. Alternatively, the lower signal intensity can also be related to a lower amplification efficiency of Osci-67F and Osci-460R primer pair. To further this we performed a $1/16^{th}$ lane titanium shotgun sequencing to understand the presence of a possible bacterial contamination. In doing so we estimated a 50% chance that full sequencing would provide promising results of forming contigs (Fig. 4.3)

From this we therefore decide to sort ≈50 cells and return for more amplification. However, after repeating the sequencing we still had a considerable level of bacterial contamination present (Fig 4.4). At the current time, other methods of whole-genome-amplification were being performed on chip (5) and then

amplified further off chip. However, our technique provided proof principle demonstration for sorting target cells from a heterogeneous sample. Possible methods that we did not explore would be to wash out remaining cells after trapping the target cell then rinse with a DNAase that would degrade any exogenous or "hitchhiker" DNA. We took the advances of our trapping technique from this project and sought next to study live single cell analysis.

4.2 Single cell growth of *E. coli*

We used the single cell microbioreactor (SCM) to observe the growth of single living *E. coli* cells in free solution for extended periods of time (up to ≈5 doubling times) (Fig. 4.5). Overnight cultures were diluted into fresh LB medium and delivered into the SCM through the sample inlet stream (Fig. 3.6). Pure LB medium (LB + ampicillin) was delivered through the two media inlet streams (Fig. 3.6), while maintaining the device at 37 ^{0}C. During cell trapping and growth experiments, the sample inlet stream was closed, and a constant volumetric flow rate of 100 μl hr^{-1} was maintained in the two inlet media streams to facilitate flow-based trapping of single cells in solution. Based on the flow field kinematics and the applied flow rates, we estimated the average shear stress experienced by a single cell due to flow (Chapter 2). Due to laminar flow conditions in the microdevice and the confinement of cells at a zero-velocity position (stagnation point), the average shear stress is ≈1E-2 dyn cm^{-2}, which is two orders of magnitude lower than cells experience when grown in a large volume shake flask (6).

For cell growth experiments, the controller gain constant Kc was set to ensure robust cell trapping, but was generally not fine-tuned to maximize trap stiffness. We found that these 'relaxed' trapping conditions were more robust to flow perturbations, which are generally uncommon, but are important to consider

during long time scale trapping experiments (≈4+ hours). In any case, the feedback controller can be fine-tuned to yield a tighter trap stiffness, if desired. In addition, a cell trapped in the 2D image plane is free to diffuse in the z-direction, defined as the direction perpendicular to the image plane. At the beginning of a cell growth experiment, single cells are selected at the mid-plane of the fluidic channel. During the course of an experiment, cells traverse ≈20 μm from the centre plane of the channel. The flow profile in the z-direction is parabolic in shape, which leads to a factor of ≈2x change in the local flow rate of the cell, which has relatively minor effect on the applied shear force due to flow. Finally, to facilitate phase-contrast imaging during single cell trapping experiments, we modified the fluidic channel geometry to incorporate an increased channel height at the cross-slot, which reduced background intensity due to PDMS boundaries.

Growth analysis was performed by tracking cell length as a function of time (Figs. 4.5a and 4.5b). Cells were observed to increase in size over time, followed by a distinct cell division event. Following cell division, we generally chose to trap and retain one of the daughter cells, and the second cell is advected away into the waste stream. In LB medium, *E. coli* showed a mean doubling time of ≈42 min in the SCM (average of 40 cells) (Fig. 4.5c). Interestingly, by observing the lineage of a single cell over multiple doubling times, the SCM allows for quantification of growth rates as a function of generation number (Fig. 4.5d).

4.2.1 Non-perturbative technique for cell growth

Given our calculations on the shear stress of cell in the hydrodynamic trap (Chapter 2) and our growth data showing extended trapping trajectories of single cells in free solution we conclude that our technique, while not currently high-throughput, provides a means for analyzing single cells under non-perturbative conditions for

extended periods of time. Previous trapping methods as mentioned in Chapter 1 that have higher trapping stiffness are able to trap cells for a growth cycle until the cell ceases to divide due to damage caused by the external force field.

4.2.2 Growth phenotypes

In addition to cell growth measurements, the SCM also allows for direct observation of cell shape and phenotype during growth. Interestingly, we observed different phenotypes for *E. coli* cells that were initially prepared from stationary state cultures compared to those that were prepared from log-phase cultures. Cells prepared from log phase cultures that are preconditioned by avoiding changes in media conditions before entering the SCM divide readily, with mother cells dissociating from progeny (Fig. 4.5e). On the other hand, cells from stationary state cultures were prone to grow in long filamentous chains with distinct cellular poles with each division (Fig. 4.5f). For both cases (filamentous versus non-filamentous growth), however, the average growth rates were similar as a function of generation number. Overall, cells appeared to adapt to the chemostatic growth environment in the SCM over subsequent generations, which is shown in the average increase in growth rate with increasing generation number (Fig. 4.5d).

4.2.3 Comparison to batch culture growth

In general, single cell experimental data is consistent with bulk analysis performed using absorbance measurements in a 96 well plate format. In bulk experiments, the doubling time of *E. coli* was found to be ≈60 min in LB medium (Fig. 4.6) and ≈111 min in M9 minimal media at 37 $^{\circ}$C (Fig. 4.7). Determining growth rates in single cell measurements (via cell length) is fundamentally different than determining growth rates in bulk experiment (via absorbance at 600 nm), which

leads to slight differences in these quantities. The SCM provides a chemostatic environment by continuous delivery of fresh nutrients with continuous removal of metabolic excretion of by-products. In this way, single cells in the SCM are not affected by population-level signalling or cell crowding that occurs in dense cell cultures in bulk experiments. Moreover, bulk measurements of cell growth may be prone to evaporation in 96 well plates, wherein individual wells are open to the atmosphere. Evaporation can be mitigated by floating a layer of oil on top of each well, but this approach can induce anaerobic growth conditions. In our observation, this effect has only been observed at time scales beyond the log phase.

4.3 Single cell gene expression of *E. coli*

In addition to cell growth experiments, we studied gene expression in single *E. coli* cells using time-lapse fluorescence microscopy (TLFM) and a fluorescent reporter protein (Venus) as a proxy for gene expression (Fig. 4.8). For these experiments, we directly observed intracellular levels of fluorescence in single cells upon switching the growth medium surrounding a single cell from M9 minimal media with 0.5% v/v glycerol to M9 with glycerol + 1 mM IPTG (Fig. 4.8a, top panel). M9 media was chosen as the preferred growth medium for these experiments due to low levels of auto-fluorescence. A major advantage of the SCM is a precise and accurate knowledge of the initial time in the experiment (time zero in Fig. 4.8c, top panel), defined as the time at which the growth environment surrounding a cell is exchanged from one well-defined medium to a second well-defined medium. The transition time for exchanging the medium around a single cell is on the order of the inverse strain rate ε^{-1}($\approx$1 sec).

Upon transitioning cells to media containing IPTG, gene expression was induced by a standard double de-repression mechanism (Chapter 3). In brief, *E. coli* was transformed with a plasmid containing a strong T5 promoter regulated by two lac

operators. In the absence of the IPTG inducer, this plasmid enables tight repression that minimizes the basal level or leaky expression of the fluorescent protein. At the beginning of each experiment, we targeted and trapped cells with low levels of intracellular fluorescence, such that the fluorescence intensity was approximately equal to the background signal. During these experiments, we first observed single living cells in M9 media without inducer for ≈10 min, following by switching the media surrounding a cell to M9 containing IPTG.

Using this approach, we recorded the intracellular fluorescence intensity values after a single step change in cell growth media (from 0 to 1 mM IPTG) at 5 min intervals using TLFM. In all cases, we observed an exponential increase in intracellular fluorescence intensity, but the rate of increase was dependent on the cell growth rate over an observation time period of ≈80 min (Fig. 4.8b). Differences in the rate of increase in intracellular fluorescence levels can be attributed to slight differences in individual cell growth rates or small differences in initial cell dimensions. For these experiments, single cell growth rates varied within the general range of $\approx 80 - 100$ min in M9 media. We observed that single cell growth rates did not significantly vary between growth in M9 medium or M9 medium + 1 mM IPTG. Finally, we performed a series of control experiments to ensure that TLFM imaging conditions resulted in no significant amounts of photobleaching. To characterize the effect of photobleaching, we observed intracellular fluorescence levels in single cells pre-induced with M9 + 1 mM IPTG, followed by a switch to M9 medium without IPTG (Fig. 4.9). During the first 10 min, the total fluorescence signal decreased due to cell division, followed by a slight decrease for longer time windows (>100 min). The slight decrease in the fluorescence over long time scales can be attributed to the cell growth and dilution of the fluorescent

protein. This fluorescence decrease has also been reported in gene expression studies at the single cell level using an agarose pad method (7).

Following single-step change experiments, we studied the response of single cells to periodic, time-dependent 'forcing' functions or 'waveforms' in inducer concentration. In these experiments, we exposed cells to a periodic square wave signal of on/off induced states (1 mM/0 mM IPTG, respectively) with a 2 min period in the cycle. Periodic forcing experiments showed a difference in intracellular fluorescence levels over the course of 80 min compared to single-step change experiments (Fig. 4.8b). In particular, periodic forcing experiments appeared to show a delay in the onset of gene expression by ≈5 min. In addition, we generally observed a slower rate of increase in fluorescence intensity for periodic step changes in inducer concentration compared to a single step change (Fig. 4.8b). Finally, we prepared an integrated time series of fluorescence images obtained from single cells during the course of a periodic step change experiment, which amounts to a z-projection stack or time series of the fluorescence emission (Fig. 4.8c, bottom image). Due to the presence of the sample inlet channel on one side of the microdevice, there is a miniscule imbalance in the flow rates on either side of the device, which results in a slight shift in the x-position of a single cell (conveniently denoting a switch in growth medium), which can be seen in Fig. 4.8c. Overall, these experiments provide proof-of-principle demonstration of precise, time-dependent control over cell environmental conditions, coupled with simultaneous phase-contrast imaging and TLFM, for observing dynamic gene expression at the single cell level.

4.3.1 Plasmid induction

We used a model plasmid vector for expressing Venus fluorescent protein. IPTG entering the cell binds to LacI repressors bound to the two operators on the

plasmid. This releases the repressor proteins promoting transcription of the fluorescent protein downstream. We chose this high copy number plasmid to ensure protein yield that would give high fluorescence emission for observation. Initially our TLFM setup was not ideal for detecting low fluorescence signals. Using a mercury arc lamp which provided ≈15 mW we were not well suited to perform TIRFM or high incident excitation. Also, our exposure times could not be increased without decreasing our feedback response of our control loop.

4.3.2 Two camera acquisition

As discussed in Chapter 3, we utilized the trinoc port of our inverted fluorescence microscope. This provided us dual image acquisition without procuring an expensive dual image adapter. However, using two different cameras with 16 bit and 10 bit pixel dimensions, proved difficult in mapping fluorescence emission with phase contrast imaging. For these experiments we used phase contrast imaging for growth results and fluorescence imaging for gene expression results separately.

4.3.3 Periodic nutrient conditions

Nutrient conditions could be switched periodically using two syringe pumps integrated in the LabVIEW. Square wave periodic switching was ideal with these mechanical syringe pumps. The lag time between start and stop of the mechanical drive train hindered sinusoidal waveforms. Pressure driven flow would be better suited for implementing a sinusoidal waveform. However, for our proof of principle demonstration, syringe pumps sufficed in providing step induction and discrete on / off periodic induction of single cell *E. coli.*

4.3.4 Comparison to batch gene expression

We used 96 well plates to perform gene expression of *E. coli* BL21 (DE3). Gene expression was not affected by adding 1 mM IPTG during the well plate run (Fig. 4.6 and Fig. 4.7. Gene expression in batch correlates well with growth rate in batch as well. We observed similar results with our single cell gene expression studies. Total fluorescence intensity increase with the growth rate of the trapped single cell. We observed sharp drops in total fluorescence due to cell division.

4.4 Intracellular diffusion in *E. coli*

To further demonstrate proof-of-principle operation of the SCM, we used the platform to observe intracellular diffusion of transcription factor proteins upon rapid exchange of cell growth media (Fig. 4.10). In particular, we directly observed the unbinding dynamics of Tet repressor proteins (TetR) fused with YFP (Venus) from a tandem binding array incorporated in the *E. coli* chromosome at the aptI locus (8, 9). Initially, cells are grown in a rich media containing a glycerol carbon source (EZ Rich Defined Medium (RDM) + 0.5% glycerol v/v), conditions under which Tet repressor proteins are localized along the binding array. During these experiments, at time t = 9 s, the cell environmental conditions in the SCM are switched to media containing 200 ng/mL anhydrotetracycline (aTc). The presence of aTc induces the unbinding of TetR from the tandem array, followed by intracellular diffusion of TetR-Venus proteins. Using the SCM, we are able to observe the rapid release and subsequent intracellular diffusion of the Tet repressor within the nucleoid region of Gram-negative bacteria (Fig. 4.10), with a clear definition of the time at which the change in the surrounding medium occurs. Intracellular diffusion events were observed by incorporating a Dual View imaging system (Photometrics DV2) to simultaneously overlay phase-contrast and fluorescence images during data acquisition.

It is important to note that the SCM allows for a precise and accurate definition of the time point of release and motion of intracellular repressor proteins, which facilitates analysis of the diffusion process. Our platform enables the rapid exchange of cell environmental conditions while maintaining single cells in free solution, whereas alternative methods of observing these diffusion events mainly rely on surface-immobilized bacteria and exchanging the surrounding medium by rinsing flow-through channels (10–12). Generally speaking, surface-immobilization techniques are contact based methods that rely on convection or diffusion for media exchange. The SCM allows for rapid exchange of media and fluid streams in free solution, which is a key advantage for single cell experiments.

4.4.1 Chromosomal binding array for colocalization

As discussed in Chapter 3, the chromosomal binding array provides a means for co-localizing proteins within the intracellular space of *E. coli* (8, 9, 13–15). This fluorescence repressor operator system (FROS) allows probing the intracellular space of bacteria. This innovation is provided by exploiting the insertion of an intermediary sequence or "landing-pad". This sequence is amplified from plasmid extraction of pTKS/CS. This intermediate sequence has an antibiotic selection for screening. Next pTKRED containing λ − red and I-SceI endonuclease is transformed into the cell. Also, pTKIP-neo containing the TetO binding array is transformed into the cell. Using ITPG and arabinose induction pTKRED expresses λ − red and I-SceI respectively. Then I-SceI excises both the intermediate and TetO binding array. Finally, λ − red promotes homologous recombination of the binding array into the chromosome at the atpI locus.

To achieve bright distinct fluorescent spots we explored different growth conditions. We found that RDM media describe in Chapter 3 was best for this

purpose. This media provided cells with optimal growing conditions for observing TetR protein dynamics after release with aTc. Our growth media is outlined in Table 4.1.

4.4.2 Image acquisition for fluorescence mapping

This task was by far the most complex of any imaging schemes that I have incorporated with the hydrodynamic trap. I incorporated a Dual View system (Photometrics) in order to simultaneously acquire phase-contrast and fluorescence emission with a single EMCCD camera. Transforming the trap to work in the Andor SDK was a feat in itself. Andor SDK was a nest of sequential frame loops operating the camera. We then overlaid the resulting images to show the intracellular dynamics within the defined cell shape given by phase-contrast. The Dual View system split the incoming light at 630 nm. We incorporated a FF01 – 655/15 filter for bright field illumination. The filter cube contained ZT488rdc dichroic and FF01 488lp emission filter. The Dual View system utilized a HQ535-30nm filter for the short wavelength fluorescence emission channel. Fig. 4.11 illustrates the fluorescence spectrum for this Dual View system.

4.5 Figures and tables

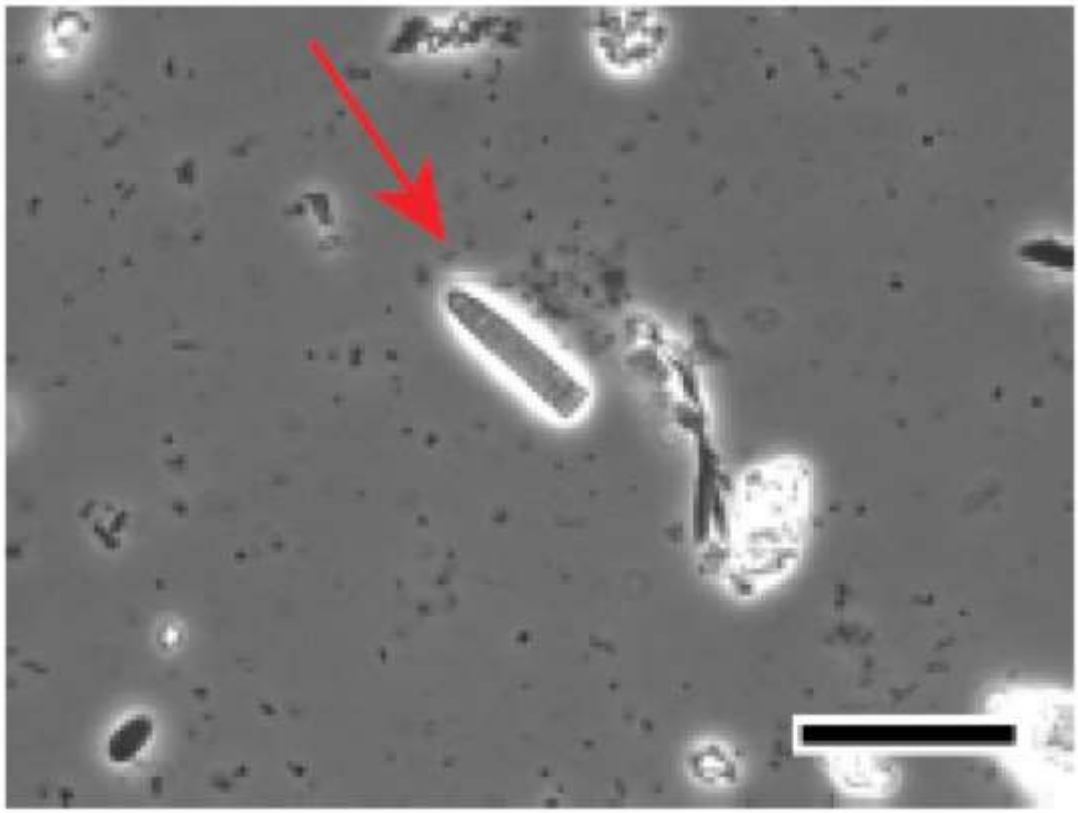

Figure 4.1: *Oscillospira* spp. in a heterogeneous rumen sample. *Oscillospira guilliermondii* (red arrow) has the unique septation pattern and promotes quick identification for cell sorting. Scale 20 μm.

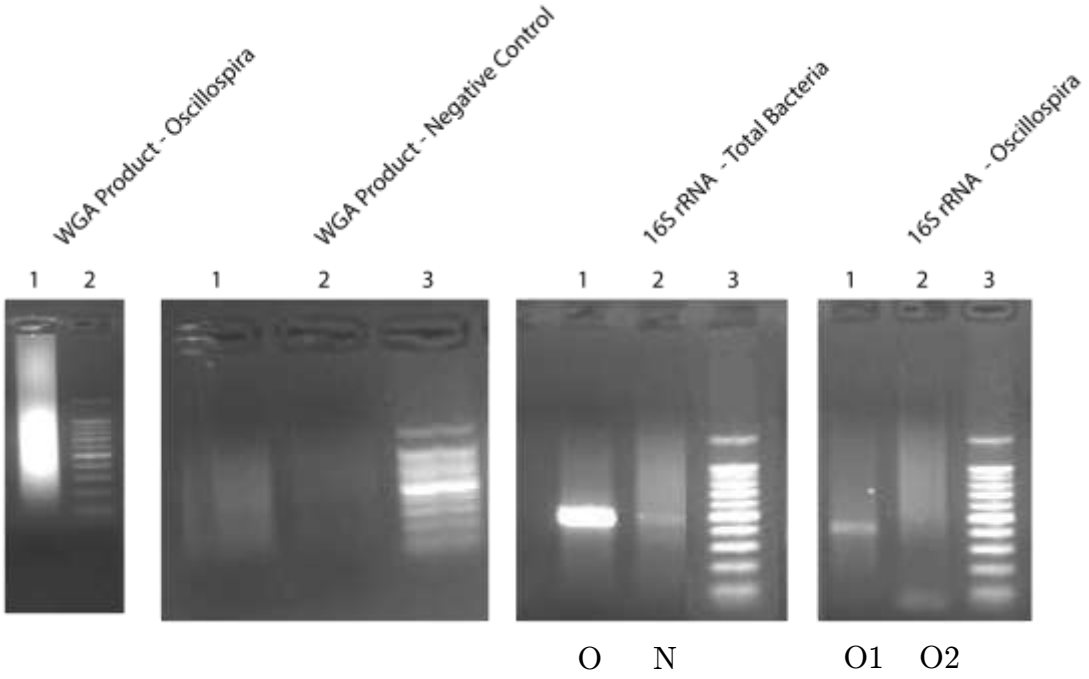

Figure 4.2: Whole genomic amplification of collected *O guilliermondii.* Whole genome amplification was done for ˜10 sorted *Oscillospira spp.* cells. There was a fragmented band ranging from $300 - 1000$bp. There seemed to be a slight bacterial contamination with the amplification step since the negative control (1X PBS, no cells) showed a slight band as well. Total bacteria 16s rRNA showed a bright band ˜500bp for O = *Oscillospira*. However, it continued to show a correct band for the negative control (N). For specific targeting *Oscillospira* primers there was a noticeable be less concentrated band then total bacteria for O1. A 100 bp ladder (Promega) was used.

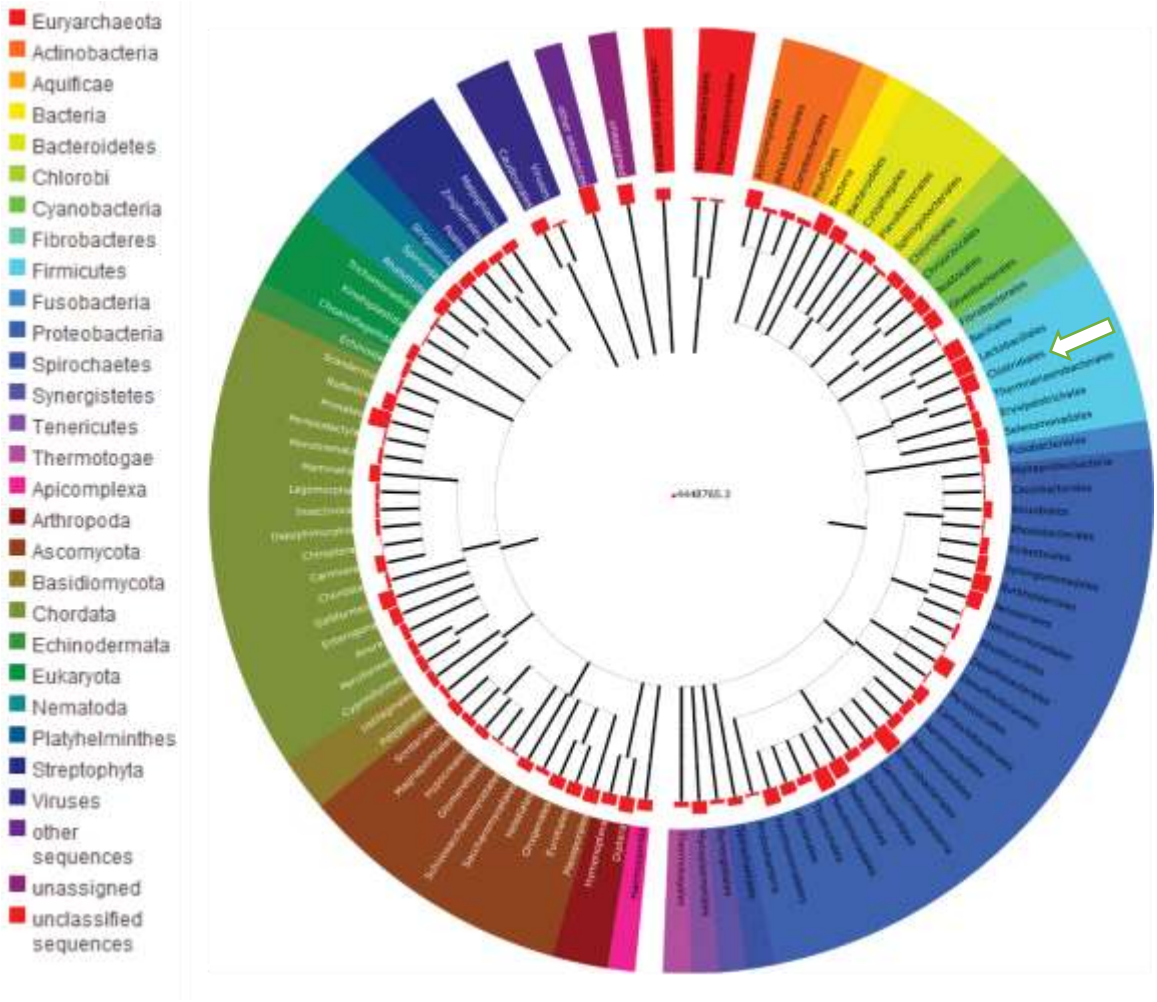

Figure 4.3: Phylogenetic tree of ten collected *Oscillospira* spp. cells. On the left shows the color chart based on phylum. The tree on the right is color coded based on phylum. *Oscillospira* spp. falls under the phylum Firmicutes and order Clostridiales (white arrow). This tree was constructed based on $1/16^{th}$ lane titanium shotgun sequencing for ˜10 *Oscillospira spp.* cells (MG-RAST).

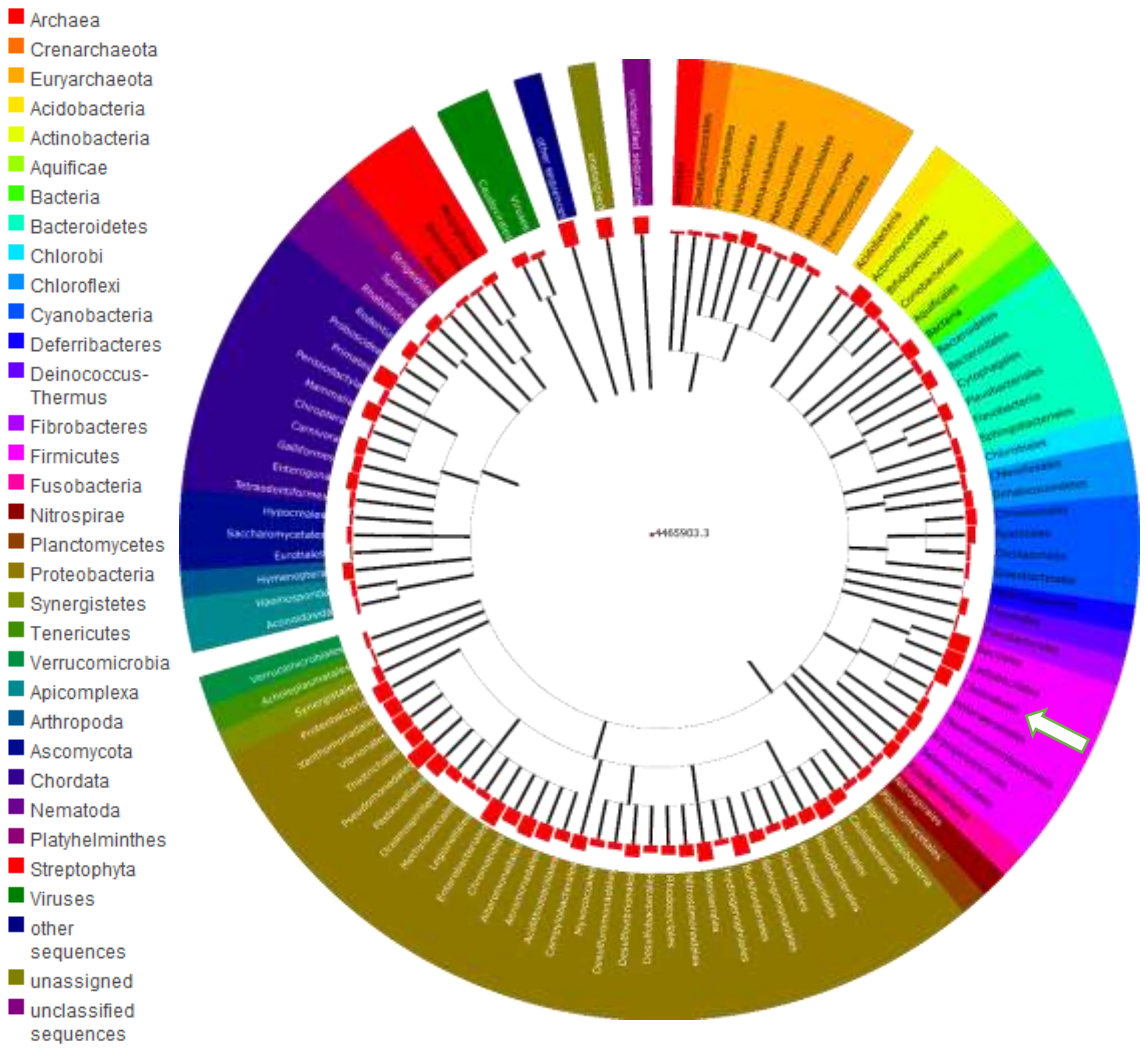

Figure 4.4: Phylogenetic tree of ten collected *Oscillospira* spp. On the left shows the list of phylum. The tree on the right is color coded based on phylum. *Oscillospira* spp. falls under the phylum Firmicutes and order Clostridiales (white arrow). This tree was constructed based on 1/16th lane titanium shotgun sequencing for ~50 *Oscillospira spp.* cells (MG-RAST).

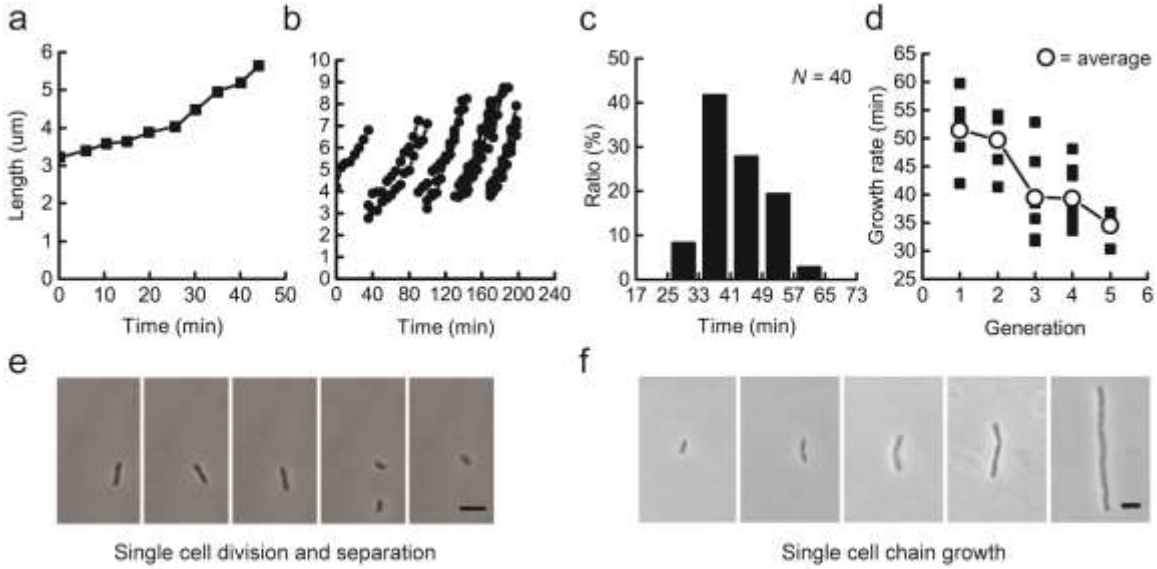

Figure 4.5: Single cell growth dynamics monitored over long time scales using the SCM. (a,e) Single cell growth trajectory and time-lapse images for a cell growth event. For dividing cells, the user has the ability to select, trap, and continue experiments with one of the daughter cells. (b,f) Multiple cell growth trajectories and time-lapse images originating from a single cell growing in a filamentous morphology. (c) Histogram of doubling times showing an average of 42.5 min (N = 40 cells). (d) Doubling time distribution as a function of cell generation in the SCM. (e,f) Time-lapse phase-contrast images of cell growth trajectories quantified in (a) and (b), respectively. Scale bars: 5 = μm.

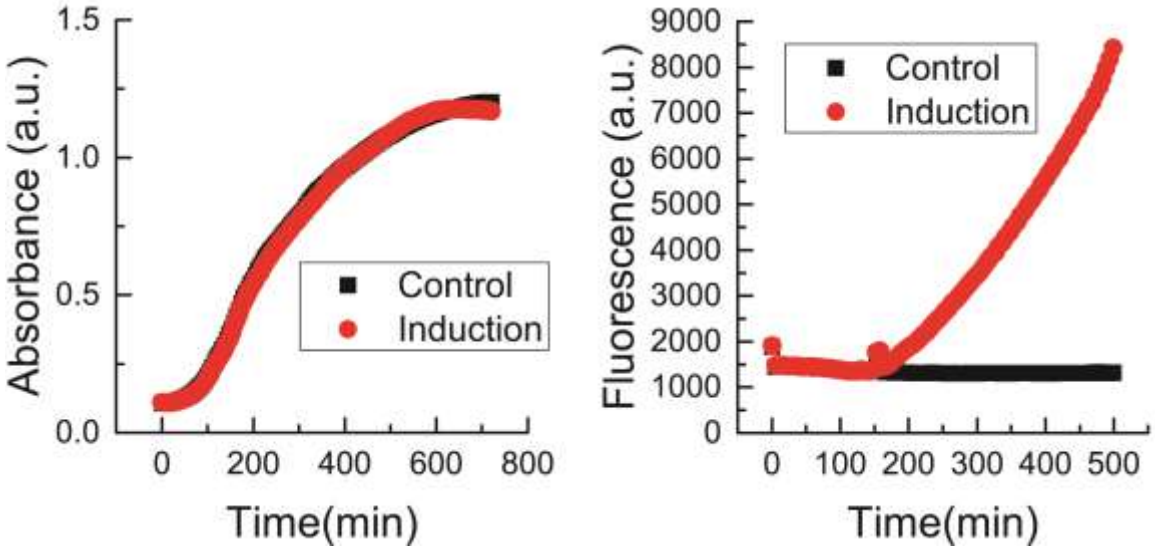

Figure 4.6: Bulk cell culture analysis to determine growth rates and cell doubling times in LB media. Data shows an average of three replicates in a 96-well plate for growth and fluorescence of BLR(DE3) pQE80L in LB medium at 37 °C. Induced media contains 1 mM IPTG. The doubling time was determined to be ˜60 min.

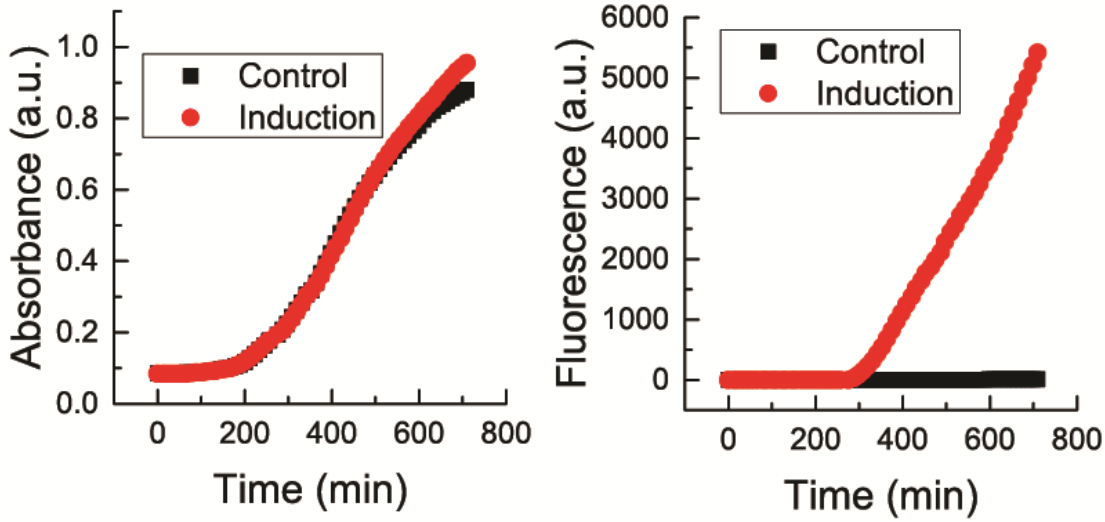

Figure 4.7: Bulk cell culture analysis to determine growth rates and cell doubling times in minimal media. Average of three replicates within a 96-well plate for growth and fluorescence of BLR(DE3) pQE80L in M9 minimal media + 0.5% v/v glycerol medium at 37 °C. Induced media contains 1 mM IPTG. The doubling time was determined to be ˜111 min under these conditions.

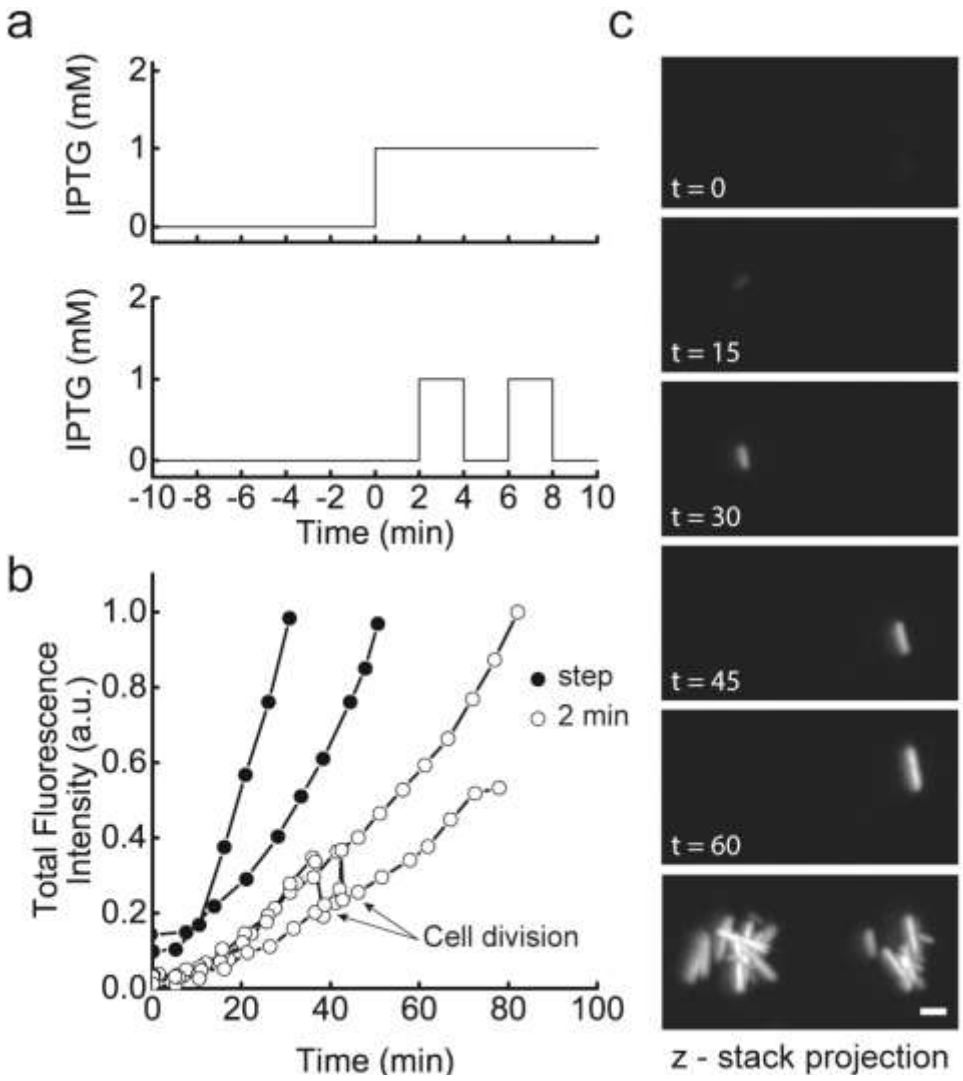

Figure 4.8: Quantifying intracellular gene expression upon rapid environmental changes in the SCM. (a) Time-dependent concentration profiles of inducer (IPTG), showing a single step change (top panel) and a periodic step change with a 2 min period (bottom panel). (b) Intracellular fluorescence intensity following a single step change or periodic step change in IPTG. Cell division is denoted by a decrease in fluorescence due to a decrease in cell volume after division. (c) TLFM images of a single cell undergoing periodic step change in IPTG (2 min period) for 1 hr. The bottom image contains a z-projection stack over the time course of the experiment. During a change in the cell environmental conditions by switching the inlet flow streams, a cell moves ˜20 μm laterally along the compressional axis due to the asymmetric flow design in the device. Scale bar: 5 μm.

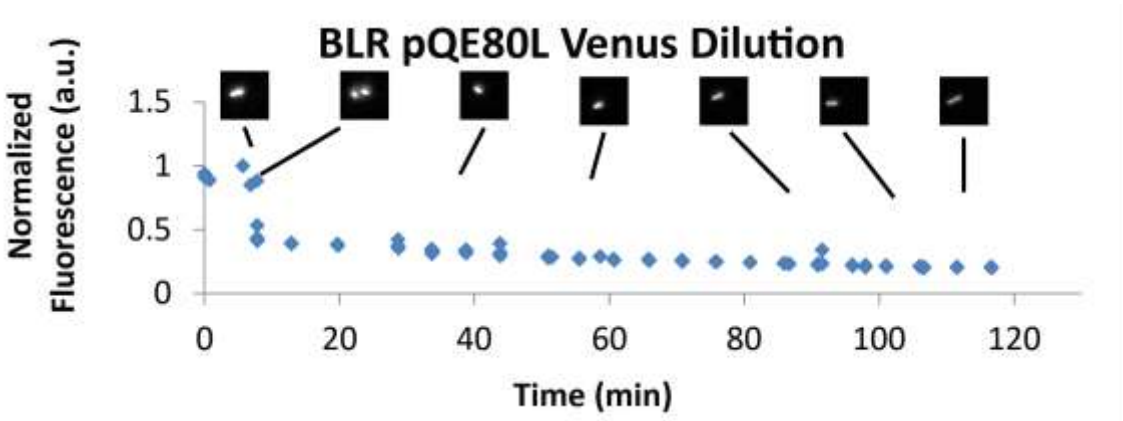

Figure 4.9: Control experiment to characterize photobleaching. We observed the total normalized intracellular fluorescence due to time-lapse fluorescence microscopy imaging. The overall decrease in fluorescence as a function of time is mainly due to dilution upon cell growth and division.

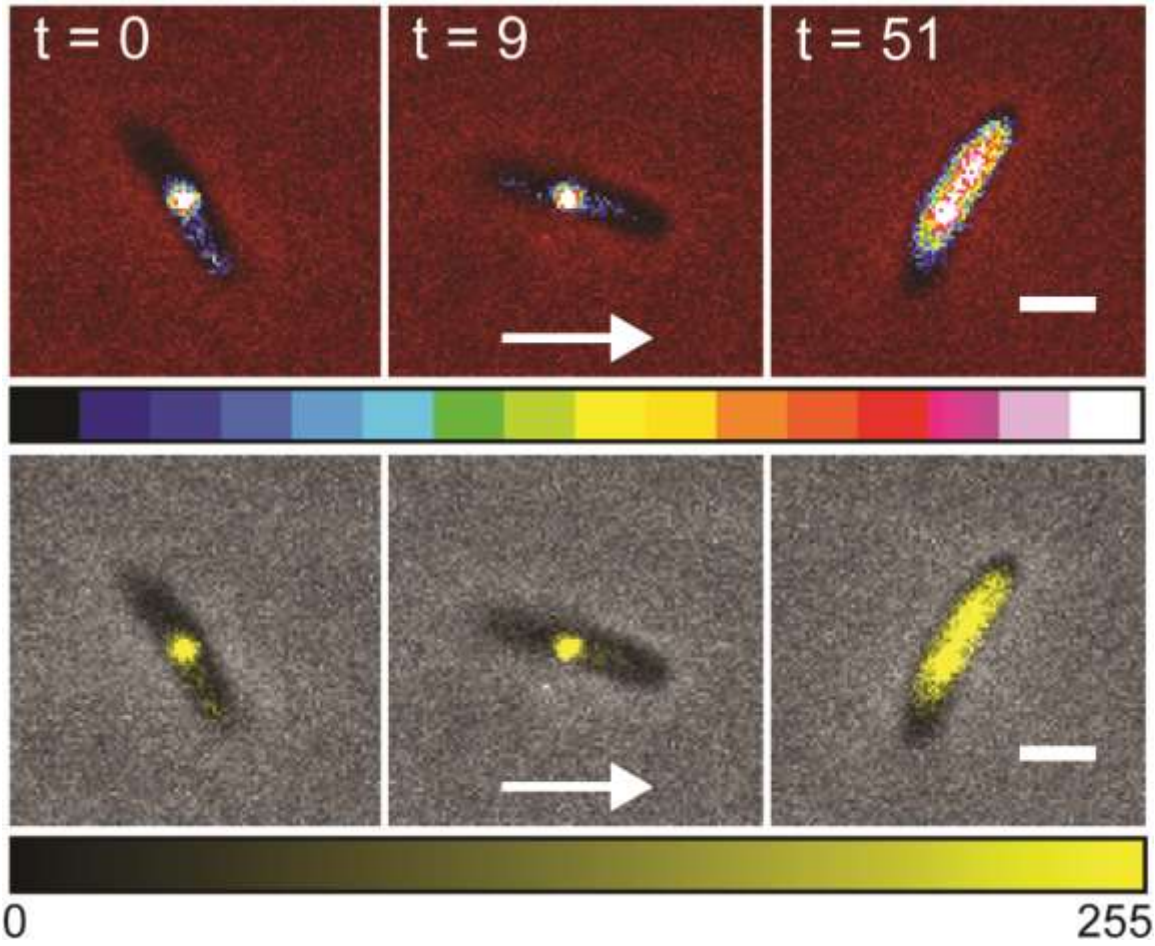

Figure 4.10: Direct observation of intracellular diffusion. We observed diffusion of the Tet repressor after a single cell is rapidly transitioned to media containing 200 ng mL^{-1} aTc, which induces unbinding of TetR from a chromosomal binding array. Fluorescence images are shown in the top panel, with fluorescence intensity represented by a color scale. Phase-contrast images superimposed with fluorescence intensity are shown in the bottom panel. Scale bar: 2 μm.

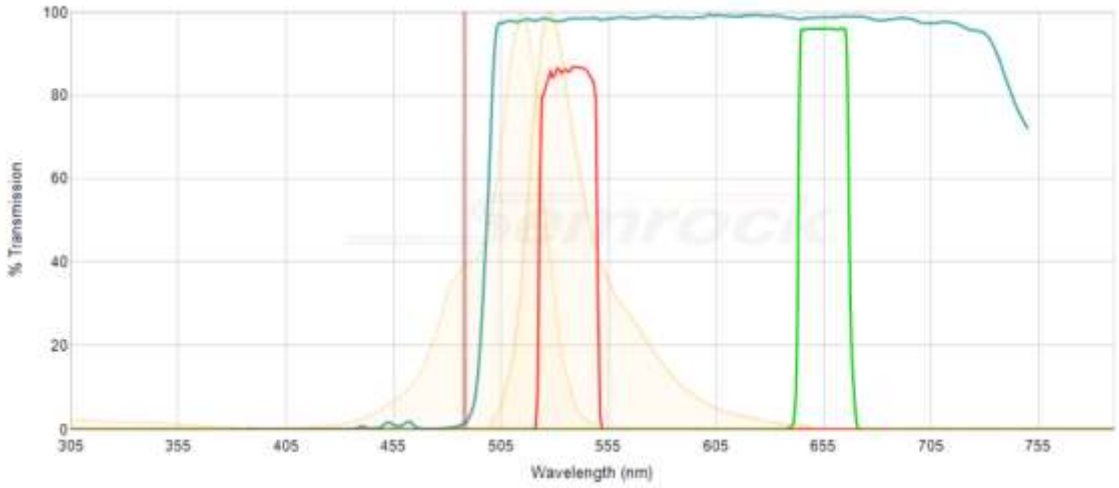

Figure 4.11: Dual VIEW filter scheme. Using a 488 nm laser, we used a 488 long pass emission filter (blue). For brightfield phase illumination we established a 30nm bandpass centered at 655. The Dual View system split wavelength in to upper and lower at 630 nm. For the short wavelength channel we added 30 nm bandpass centered at 535 nm. Venus excitation and emission spectra are orange in the background.

4.6 References

1. Mackie, R.I., R.I. Aminov, W. Hu, A. V Klieve, D. Ouwerkerk, et al. 2003. Ecology of uncultivated Oscillospira species in the rumen of cattle, sheep, and reindeer as assessed by microscopy and molecular approaches. Appl. Environ. Microbiol. 69: 6808–15.

2. Quake, S.R. 2000. From Micro- to Nanofabrication with Soft Materials. Science (80-.). 290: 1536 – 1540.

3. Zhang, J., M. Li, W.H. Li, and G. Alici. 2013. Inertial focusing in a straight channel with asymmetrical expansion–contraction cavity arrays using two secondary flows. J. Micromechanics Microengineering. 23: 085023.

4. Gossett, D.R., H.T.K. Tse, S.A. Lee, Y. Ying, A.G. Lindgren, et al. 2012. Hydrodynamic stretching of single cells for large population mechanical phenotyping. Proc. Natl. Acad. Sci. U. S. A. 109: 7630–5.

5. Marcy, Y., C. Ouverney, E.M. Bik, T. Lö sekann, N. Ivanova, et al. 2007. Dissecting biological " dark matter" with single-cell genetic analysis of rare and uncultivated TM7 microbes from the human mouth. Proc. Natl. Acad. Sci. U. S. A. 104: 11889–94.

6. Fridley, K.M., M.A. Kinney, and T.C. McDevitt. 2012. Hydrodynamic modulation of pluripotent stem cells. Stem Cell Res. Ther. 3: 45.

7. Rosenfeld, N., J.W. Young, U. Alon, P.S. Swain, and M.B. Elowitz. 2005. Gene regulation at the single-cell level. Science. 307: 1962–5.

8. Kuhlman, T.E., and E.C. Cox. 2010. Site-specific chromosomal integration of large synthetic constructs. Nucleic Acids Res. 38: e92.

9. Kuhlman, T.E., and E.C. Cox. A place for everything: chromosomal integration of large constructs. Bioeng. Bugs. 1: 296–9.

10. Groisman, A., C. Lobo, H. Cho, J.K. Campbell, Y.S. Dufour, et al. 2005. A microfluidic chemostat for experiments with bacterial and yeast cells. Nat. Methods. 2: 685–9.

11. Long, Z., E. Nugent, A. Javer, P. Cicuta, B. Sclavi, et al. 2013. Microfluidic chemostat for measuring single cell dynamics in bacteria. Lab Chip. 13: 947–54.

12. Bennett, M.R., W.L. Pang, N.A. Ostroff, B.L. Baumgartner, S. Nayak, et al. 2008. Metabolic gene regulation in a dynamically changing environment. Nature. 454: 1119–22.

13. Bintu, L., N.E. Buchler, H.G. Garcia, U. Gerland, T. Hwa, et al. 2005. Transcriptional regulation by the numbers: models. Curr. Opin. Genet. Dev. 15: 116–24.

14. Kuhlman, T., Z. Zhang, M.H. Saier, and T. Hwa. 2007. Combinatorial transcriptional control of the lactose operon of Escherichia coli. Proc. Natl. Acad. Sci. U. S. A. 104: 6043–8.

15. Kuhlman, T.E., and E.C. Cox. 2012. Gene location and DNA density determine transcription factor distributions in Escherichia coli. Mol. Syst. Biol. 8: 610.

Chapter 5

Conclusions and Future Directions

The SCM allows for direct observation of the intracellular dynamics during rapid media exchange for single cells in free solution. This technique provides a new method for observing single cell growth in an on-chip fashion. In this way, the SCM truly enables a chemostatic environment for observing the growth of single cells, allowing for continuous delivery of fresh nutrients with continuous removal of metabolic waste. Using the SCM, we observed cell growth for long time scales (~5 cell divisions) and across several generations of daughter cells. In this way, the SCM allows for cell growth dynamics to be characterized for the full lineage of a single cell, with measurements of growth over successive generations for cells grown in free solution. Interestingly, our results suggest that as cells adapt to the chemostatic growth environment in the SCM, the average growth rates increase with subsequent generations. Moreover, the SCM facilitates stable confinement of motile bacteria, which attempt to actively swim away from the trap center during growth experiments.

In addition to cell growth measurements, the SCM allows for direct characterization of intracellular fluorescence levels and gene expression as a function of the dynamic cell growth environment. Here, we incorporate phase-contrast imaging and TLFM to simultaneously observe cell phenotype and intracellular fluorescence levels over time. In this work, we use the SCM to induce single step changes and time-dependent, periodic step changes in the cell growth medium while confining and observing a single cell in free solution and maintaining a constant total volumetric flow rate. During these experiments, cell division events are clearly observed in the dynamic trajectories. These experiments serve as proof-of-principle validation of the SCM for characterizing gene expression and cell growth.

Finally, we used the SCM to directly observe intracellular diffusion of transcription factor proteins following a rapid change in the cell growth environment. In this way, the SCM effectively provides a new method for rapid on-demand nutrient switching while enabling observation of a 'target' cell in free solution. Importantly, the SCM allows for precise knowledge of 'time zero', or the time at which a cell is transitioned from one medium to a different medium. In our experiments, we used aTc as the stimulus to release Tet repressor proteins bound to a chromosomal binding array. Using this approach, we are able to control and subsequently observe the intracellular diffusive dynamics of the Tet repressor, thereby allowing for characterization of the spatial distribution of transcription factors in a target cell.

In this work, we presented an integrated two-layer microfluidic device capable of confining single cells for long time scales in free solution. The SCM is able to sustain constant nutrient conditions or periodic 'forcing' of well-defined growth media while allowing for direct analysis. Overall, the microfluidic bioreactor

presented in this work provides a new method for sustaining or dynamically controlling environmental conditions, measuring growth rates, detecting gene expression, and observing intracellular dynamics in single cells suspended in free solution.

5.1 Comparison to other single cell techniques

Our research encompasses a method for free solution confinement using the sole action of fluid flow. No barriers or external force fields were required for our technique. Through the study and research of techniques such as optical, magnetic, acoustic, and electrophoretic, we became inspired to extend the field even further. As stated previously, our technique provides a non perturbative method as observed by growth rates and increased cell fecundity over generations. We have extensively characterized our trapping technique with quantitative work within the Schroeder group (1). Our approach was not to tackle the issue of high-throughput single cell analysis but rather provide a cost effective technique for researchers across disciplines to study single cells. Recently published works have utilized planar extensional flow for applications such as cell deformation, cell to cell contact, actin polymerization, and polymer relaxation studies (2–5). Automated trapping for polymer relaxation studies and single cell analysis has been previously been developed in the Schroeder laboratory. However, the remaining applications utilize the flow field in either a high-throughput or manual trap fashion providing only finite time increments for observation. To the best of our knowledge, we believe that our technique is the first of its kind towards non perturbative free solution trapping of single cells. With continued development, the SCM can be used to study many systems of biological interest.

5.2 Improved devices

Throughout this thesis we have discussed the use of PDMS for fabricating our hydrodynamic trap and SCM. Albeit the advantages of the elastomeric polymer (i.e its FDA approval for use in fast food as an anti-caking agent), PDMS is absorbent to many small molecules. Weitz's group has explored the disadvantages of PDMS in order to circumvent them (6). They tested PDMS channels filled with rhodamine dye and observed absorption into the PDMS by observing fluorescence emission over time. PDMS also has have issues with swelling when exposed to certain solvents. The main goal of their research was to implement a sol-gel chemistry to coat the channels. This inert gel prevents absorption and protects the channel from solvent exposure. For certain applications where circular channels are ideal, sol-gel provides this cross section by wetting the channel and when forced out with air creates a microfluidic pipe cross-section. During early exploration in lab I have tried to implement this chemistry with the hydrodynamic trap to create a more hydrophobic surface. However, when fully evaporating the sol-gel, the composition of two silanes become glass-like. This creates a rigid structure and inhibits the functionality of the valve for controlling the stagnation point. Implementing an off-chip laminar outflow regulator may be compatibility with this surface chemistry. Another approach is to incorporate an acrylic such as poly(methyl methacrylate) (PMMA). This thermoplastic structure provides a transparent rigid channel structure. However, elastomeric valves would not be available and an off-chip flow regulator would be ideal.

The hydrodynamic trap provides trap and manipulation in the xy plane. We have teased the idea of incorporating additional axis of compression along the z-axis. However, this method would require creative microfabrication approaches to achieve a robust and reproducible design. Leading the way to make this advancement would be to incorporate an approach for PDMS 3D microfluidics by

Zhang et al. (7). They have developed a technique for transferring multiple PDMS layers for creating 3D microfluidic networks. Also, 3D printing has seen a remarkably advance and are now more readily available in fab labs and universities. The creators of the Mother Machine(8) and independent researchers developed an inexpensive print replica method by incorporating molds developed with a 3D printer and adhesive resins.

A step towards *z*-axis confinement was our implementation of stage translation using a piezo z-stage (PI). This stage interfaces readily with a USB interface into LabVIEW. We created an independent feedback control based on the cell focus. When the cell moves out of the plane of focus the image process controller searching for dark objects begins to lose or reduce the size of the output binary image. Therefore, we chose to force the controller to maximize the cell area by adjust the device in the z-axis. Now we could not be for certain which direction of adjust was appropriate. If the stage moved a distance $+d$ in the positive z $-$axis and the image became worse than the stage would move *-2d.* The controller repeated this process until a maximum cell area was achieved (i.e. the cell was at the focal plane). To improve this focus controller a cylindrical lens could be placed in the optical path. This would provide unique distortion relative to the position across the focal plane. This method has been routinely used for single molecule tracking in the z-axis (9).

Alternatively, an interesting approach would be able to confine the z dimension by placing a large valve above the stagnation point. By compressing this valve you would be effectively changing the position of the trap potential well along the *z*-axis. This process would be an interesting model for developing an adaptive controller that would account for changes in the flow field due to the extra valve for the z dimension. A feedforward approach may provide a more intuitive implementation in this scenario. When I tried implementing this approach the

imaging in phase contrast became saturated. This may be due to the deflection of light through air then water during the deformation of the PDMS. A possible way for circumventing this saturation would be instead to fill the z valve with a fluid that has an appropriate index of refraction. This approach is routinely done in the field of optofluidics (10).

5.3 Motile cells

Freely swimming cells are capable of confinement within the trap. However, because of the no-slip condition at the boundary interface the fluid velocity approaches zero. Therefore, cells are able to move freely against the fluid flow at the surface. To ensure consistent confinement of swimming cells a method for true confinement in the z-axis mentioned above would help prevent cell loss. This includes increasing flow rates to shape the trap potential and increase trap stiffness. Keeping the trap potential fixed on a cell in 3D, will help alleviate concerns of cells swimming in the yz plane towards the surface.

5.4 Potential applications

The hydrodynamic trapping technique has been utilized across many fields ranging from emulsions, biopolymers, sequencing and single cells (1, 5, 11–17). The SCM developed in this work is the first step towards providing a single cell quantitative approach using a non-perturbative method for confinement in free solution. By improving our experimental techniques for mimicking cellular environments we can began to develop better cellular and intracellular models.

I provide here a brief list of ideas I have pondered and discussed with fellow labmates during my time at the University of Illinois:

1. My previous research was on microtubule polymerization in the presence of porphyrins(18, 19). I have always considered revisiting this research and isolating microtubules from solution and looking at polymerization dynamics, relaxation, and instability under different flow conditions and or ligand concentrations. This is analogous to the work that was perceived by Kentsler and Goldstein in 2012 for studying actin filaments in extensional flow(4).

2. Single molecule pull down (SiMPull) assay developed in Prof. Taekjip Ha's lab at Illinois provides direct single molecule methods for characterizing the protein composition of cellular extracts (20). Currently, cells are lysed off chip and introduce into the flow cell for pull down and immobilization. Combining our hydrodynamic trapping technique with this method would allow direct single cell protein composition profiles. During my *E. coli* experiments I have observed direct cell lysis with lysis buffer provided from a Qiagen mini prep kit.

3. Before the conception of the cell sorting project we had discussed ideas for trapping cells in anaerobic conditions. Many approaches had come before including unique setups for mimicking an anaerobic chamber that could be mounted to on a microscope stage. Our approach however, was to utilize oxygen scavenger systems such as glucose oxidase and catalase for studying cells in anaerobic conditions. We were able to get great laminar streams showing anaerobic and aerobic conditions using resazurin as probe for oxygen. We were unsure however what the concentration of oxygen as this was important since at the time it was debatable as to how low in ppm oxygen needed to be in order to convert *E. coli* to anaerobic conditions.

5.5 References

1. Tanyeri, M., M. Ranka, N. Sittipolkul, and C.M. Schroeder. 2011. A microfluidic-based hydrodynamic trap: design and implementation. Lab Chip. 11: 1786–94.

2. Gossett, D.R., H.T.K. Tse, S.A. Lee, Y. Ying, A.G. Lindgren, et al. 2012. Hydrodynamic stretching of single cells for large population mechanical phenotyping. Proc. Natl. Acad. Sci. U. S. A. 109: 7630–5.

3. Roth, K.B., C.D. Eggleton, K.B. Neeves, and D.W.M. Marr. 2013. Measuring cell mechanics by optical alignment compression cytometry. Lab Chip. 13: 1571–7.

4. Kantsler, V., and R.E. Goldstein. 2012. Fluctuations, Dynamics, and the Stretch-Coil Transition of Single Actin Filaments in Extensional Flows. Phys. Rev. Lett. 108: 038103.

5. Schroeder, C.M., H.P. Babcock, E.S. Shaqfeh, and S. Chu. 2003. Observation of polymer conformation hysteresis in extensional flow . Science. 301: 1515–1519.

6. Abate, A.R., D. Lee, T. Do, C. Holtze, and D.A. Weitz. 2008. Glass coating for PDMS microfluidic channels by sol-gel methods. Lab Chip. 8: 516–8.

7. Zhang, M., J. Wu, L. Wang, K. Xiao, and W. Wen. 2010. A simple method for fabricating multi-layer PDMS structures for 3D microfluidic chips. Lab Chip. 10: 1199–203.

8. Wang, P., L. Robert, J. Pelletier, W.L. Dang, F. Taddei, et al. 2010. Robust growth of Escherichia coli. Curr. Biol. 20: 1099–103.

9. Kao, H.P., and A.S. Verkman. 1994. Tracking of single fluorescent particles in three dimensions: use of cylindrical optics to encode particle position. Biophys. J. 67: 1291–300.

10. Nguyen, N.-T. 2010. Micro-optofluidic Lenses: A review. Biomicrofluidics. 4.

11. Taylor, G.I. 1934. The Formation of Emulsions in Definable Fields of Flow. Proc. R. Soc. London.Series A, Contain. Pap. a Math. Phys. Character. 146: 501 – 523.

12. Bentley, B.J., and L.G. Leal. 1986. A computer-controlled four-roll mill for investigations of particle and drop dynamics in two-dimensional linear shear flows. J. Fluid Mech. 167: 219.

13. Dylla-Spears, R., J.E. Townsend, L. Jen-Jacobson, L.L. Sohn, and S.J. Muller. 2010. Single-molecule sequence detection via microfluidic planar extensional flow at a stagnation point. Lab Chip. 10: 1543–9.

14. Brockman, C., S.J. Kim, and C.M. Schroeder. 2011. Direct observation of single flexible polymers using single stranded DNA. Soft Matter. 7: 8005.

15. Tanyeri, M., E.M. Johnson-Chavarria, and C.M. Schroeder. 2010. Hydrodynamic trap for single particles and cells. Appl. Phys. Lett. 96: 224101.

16. Tanyeri, M., and C.M. Schroeder. 2013. Manipulation and confinement of single particles using fluid flow. Nano Lett. 13: 2357–64.

17. Johnson-Chavarria, E.M., M. Tanyeri, and C.M. Schroeder. 2011. A microfluidic-based hydrodynamic trap for single particles. J. Vis. Exp. : 1–5.

18. Tian, F., E.M. Johnson, M. Zamarripa, S. Sansone, and L. Brancaleon. 2007. Binding of porphyrins to tubulin heterodimers. Biomacromolecules. 8: 3767–3778.

19. Valdez, R., E. M Johnson, J. A Belcher, J. F Fuini, L. Brancaleon, et al. 2009. Porphyrins affect the self-assembly of tubulin in solution. Biophys. Chem. 145: 98–104.

20. Jain, A., R. Liu, B. Ramani, E. Arauz, Y. Ishitsuka, et al. 2011. Probing cellular protein complexes using single-molecule pull-down. Nature. 473: 484–8.

Appendix A:

SCM Fabrication Protocol

The protocol for microfabrication of the SCM presented in this thesis may be found in a supplemental file named **JohnsonChavarriaSCMFabrication.docx**

Appendix B:

SCM Mask Design

The mask transparency design for microfabrication of the SCM presented in this thesis may be found in a supplemental file named **JohnsonChavarriaSCMDesign.ai**

***Note: If you do not have Adobe Illustrator this file will be compatible with Adobe Reader and will open a pdf to view only.**